POLYTECHNIQUE MONTRÉAL

affiliée à l'Université de Montréal

Metal-based antireflective coatings with improved durability for ophthalmic applications

PHILLIP RUMSBY

Département de génie physique

Mémoire présenté en vue de l'obtention du diplôme de *Maîtrise ès sciences appliquées*

Génie physique

Août 2020

POLYTECHNIQUE MONTRÉAL

affiliée à l'Université de Montréal

Ce mémoire intitulé :

Metal-based antireflective coatings with improved durability for ophthalmic applications

présenté par **Phillip RUMSBY**

en vue de l'obtention du diplôme de *Maîtrise ès sciences appliquées*

a été dûment accepté par le jury d'examen constitué de :

Sébastien FRANCOEUR, président
Ludvik MARTINU, membre et directeur de recherche
Jolanta-Ewa SAPIEHA, membre et codirectrice de recherche
François SCHIETTEKATTE, membre externe

ACKNOWLEDGEMENTS

I'd like to start by thanking my research director and co-director, Ludvik Martinu and Jolanta-Ewa Sapieha, for the opportunity of joining the FCSEL, enabling the past few years working on this project, and hopefully the next few years working on projects to come.

I'd also like to thank all of the technicians who've helped me at FCSEL, Francis Turcot, Francis Boutet and Samuel Cardinal, without whom this would be scarcely more than a literature review.

This work would be of far lesser quality if it weren't for the insightful advice of all the research associates and senior FCSEL students, particularly Oleg Zabeida, who has always helped me take my work a step further.

Special thanks go out to Bill Baloukas, who has given me guidance on practically every aspect of this work, from fabricating samples to analysing them, and from reading my first few papers on this topic to writing this thesis. He has been unwavering in his helpfulness throughout this project and has even recommended a couple great books.

I want to thank *all* my peers as well, who've made the last couple of years dynamic, stimulating and fun. I was lucky to have Louis Dubé-Riopel as my colleague from the very beginning of this project all the way through to writing the last few lines of this work. I'm eager to continue working alongside all my other peers who aren't done just yet.

Last but not least, I want to thank my friends and family who make my life *outside* of this project as good as it is. Like my peers at FCSEL, I cannot name them all, but I specifically want to thank my parents for all their support, from kindergarten to grad school, my brother John and my friend Eli, who are models as academics and as people, and who make my life that much more enjoyable. Finally, I want to thank Camille, who supports, understands and helps me, and everyone else who is lucky enough to have her in their lives.

RÉSUMÉ

Dans une ère de supraconducteurs et d'isolants topologiques, les matériaux typiques peuvent sembler comme il n'ont plus rien à nous offrir. Mais au contraire, la plasmonique a prouvé qu'avec de la physique classique et un concept ingénieux, les métaux peuvent produire des phénomènes optiques intéressants et inattendus, et a inspiré une multitude de nouveaux moyens d'utiliser les métaux en optique.

Dans ce travail, nous avons tenté d'utiliser des couches métalliques pour améliorer la performance et la durabilité des lunettes. Plus précisément, le but était de produire un revêtement optique contenant une couche mince métallique permettant un effet antireflet important, et offrant une durabilité suffisante afin de résister à l'usage quotidien d'une paire de lunettes.

Les revêtements antireflets (AR), ont été produits selon une architecture diélectrique-métal-diélectrique. L'argent (Ag) fût sélectionné pour la couche métallique en raison de ses propriétés optiques hautement désirables, même parmi les métaux nobles. Cela étant dit, l'utilisation de l'Ag apporte son lot de défis. Tout d'abord, les couches minces d'Ag tendent à former des îlots lorsque déposées sur un diélectrique; ces îlots mènent alors à une absorption indésirable par résonance plasmon localisée. De plus, l'Ag est susceptible chimiquement, pouvant être dégradé par le chlore dans les huiles naturelles de la peau ou l'oxygène de l'air ambiant.

Ainsi ce travail traitait de deux aspects: la performance optique devait être contrôlée via la dynamique de croissance, sans introduire de susceptibilités à l'environnement et des mesures de protection devaient être implémentées tout en minimisant leur impact sur la transparence et la performance de l'AR. L'étude a été menée sur des échantillons produits par pulvérisation magnétron et par évaporation par faisceau d'électrons. La dynamique de croissance et les propriétés optiques des couches d'argent ont été étudiées par ellipsométrie spectroscopique *in situ*, ainsi que par des mesures de la résistance de feuille, par spectrophotométrie et par ellipsométrie *ex situ*. Les effets des différentes architectures et conditions de dépôt sur la nanostructure et la durabilité des revêtements ont été étudiés par diffraction de rayons-X et dans divers tests de durabilité standardisés conçus pour les lentilles ophthalmiques, tels que la résistance à l'abrasion, à la délamination, à l'humidité et à la corrosion dans une solution aqueuse de NaCl. Le recouvrement de l'Ag par un diélectrique et le dopage à l'aluminium se sont révélés être des mesures de protection

insuffisantes. L'utilisation de couches à base de nickel (Ni) et de nitrure de chrome (CrN_x) de quelques angströms d'épaisseur ont permis une durabilité chimique et mécanique accrue. En séparant le dépôt du Ni et du CrN_x et en utilisant une couche de croissance d'oxide de zinc (ZnO), des empilements chimiquement et mécaniquement durables ont été produits avec moins de 11% d'absorption et 1% de réflexion dans spectre visible. Divers moyens de contrôler la croissance de l'Ag ont été étudiés ainsi que leurs effets sur sa microstructure et la durabilité résultante de celle-ci. Des améliorations potentielles visant à augmenter la performance optique en conservant la durabilité des revêtements sont suggérées.

ABSTRACT

In an era of superconductors and topological insulators, common materials may sometimes seem like they have nothing left to offer. But on the contrary, the field of plasmonics has proved that, with classical physics and a clever concept, metals can provide us with interesting and unexpected optical phenomena and has inspired a multitude of novel uses for metals in optics.

In this work, we have attempted to use metallic layers to improve both the performance and durability of eyeglasses. More precisely, the goal was to create an optical coating containing a thin metallic layer to enable a strong antireflective effect, while proving durable enough to survive the daily ordeals of a pair of glasses.

Antireflective (AR) coatings were made following a dielectric-metal-dielectric architecture. Silver (Ag) was chosen to constitute the metal layer, due to its highly coveted optical properties even amongst noble metals. That being said, the use of Ag brings about challenges of its own. First, thin Ag layers tend to form islands when deposited on dielectrics; these islands then lead to undesirable absorption due to localized plasmon resonance. Moreover, Ag is susceptible to degradation by a host of chemicals, including the chlorine found in oils naturally coating our skin and the oxygen we breathe.

Thus, the work was twofold: optical performance was to be improved through control of the film growth without introducing durability issues and protective measures were to be implemented while minimising their impact on coating transparency and AR performance. The study was performed on samples deposited by magnetron sputtering and electron beam evaporation. Growth dynamics and optical properties of silver films were studied by *in situ* spectroscopic ellipsometry, as well as *ex situ* ellipsometry, spectrophotometry and sheet resistance measurements. The effects of these different deposition conditions and architectures on the nanostructure and durability of the coatings were investigated by X-ray diffraction measurements and standardized durability tests designed for ophthalmic lenses, such as resistance to abrasion and delamination, humidity and corrosion in an aqueous NaCl solution. Coating Ag with a dielectric layer and aluminum doping both proved to be insufficient protective measures. The use of nickel (Ni) and chromium nitride (CrN_x) based coatings of a few angstroms allow increased chemical and mechanical durability. By separating the Ni and CrN_x depositions and using a zinc oxide (ZnO) seed layer, chemically and

mechanically durable stacks with less than 11% absorption and 1% reflection in the visible spectrum were produced. Different means of controlling Ag growth were studied, as well as their effect on the Ag microstructure and the resulting changes in durability. Potential improvements towards depositing more optically performant yet equally durable coatings are suggested.

TABLE OF CONTENTS

ACKNOWLEDGEMENTS III

RÉSUMÉ IV

ABSTRACT VI

TABLE OF CONTENTS VIII

LIST OF TABLES XI

LIST OF FIGURES XII

LIST OF SYMBOLS AND ABBREVIATIONS XVI

LIST OF APPENDICES XXI

CHAPTER 1 INTRODUCTION 1

1.1 The material limitations of antireflection coatings 1

1.2 Context of the research 5

1.3 Objectives 7

1.4 Outline 7

CHAPTER 2 THEORY & LITERATURE REVIEW 9

2.1 Optical considerations 9

2.1.1 Photometry and human perception of light 9

2.1.2 Propagation and interference 11

2.1.3 The optical properties of materials 14

2.2 The deposition of silver films 18

2.2.1 Island growth 18

2.2.2 Controlling growth in physical vapor deposition processes 24

2.2.3 Growth modification techniques 30

2.3 The durability of silver films 39

2.3.1 Degradation mechanisms 40
2.3.2 Enhancing silver durability 43
CHAPTER 3 METHODOLOGY 46
3.1 Sample fabrication 46
3.1.1 E-beam evaporation 47
3.1.2 Magnetron sputtering 50
3.2 Optical characterization 52
3.2.1 Spectrophotometry 52
3.2.2 Ellipsometry 53
3.2.3 Modeling 56
3.3 Durability testing 57
3.3.1 Temperature test 58
3.3.2 UV radiation test 58
3.3.3 Mechanical durability test 58
3.3.4 Humidity test 59
3.3.5 Saline corrosion test 59
3.4 Additional characterization methods 61
3.4.1 Contactless sheet resistance 61
3.4.2 X-ray diffraction 62
3.4.3 Stylus profilometry 62
CHAPTER 4 RESULTS & DISCUSSION 63
4.1 Improving silver film coalescence 63
4.1.1 Preliminary results 63
4.1.2 Increased deposition rate 65

4.1.3 Oxygen-doped silver films 67
4.1.4 Dielectric seed layers 69
4.1.5 Nitrogen-doped silver films 73
4.1.6 Aluminum-doped silver films 78
4.1.7 Metallic seed layers 80
4.2 Improving silver film durability 82
4.2.1 Preliminary observations 82
4.2.2 Dielectric protective layers 86
4.2.3 Doped silver films 87
4.2.4 Metallic protective layers and seed layers 89
4.2.5 Improvement of metallic layers 93
4.2.6 Mechanical durability 98
CHAPTER 5 GENERAL DISCUSSION 101
CHAPTER 6 CONCLUSION & RECOMMENDATIONS 112
REFERENCES 114
APPENDIX 124

LIST OF TABLES

Table 3.1: Default deposition parameters for deposition processes by e-beam. 49

Table 3.2: Default deposition parameters and average deposition rate for deposition processes by magnetron sputtering. 51

Table 4.1: Mean A_V of coatings using $Ag_{(N)}$ layers produced with different deposition parameters in e-beam evaporation. 74

Table 4.2: Opto-electronic properties of notable AR coating configurations produced by e-beam. 76

Table 4.3: Summary of different durability tests used. 82

Table 4.4: A_V and t_{C2} of coatings containing Ag layers protected by CrN_x layers produced in an Ar-N_2 working gas with varying amounts of N_2. 90

Table 4.5: T_V (0° incidence) and t_{C2} of samples using 15 nm of Ag protected by various combinations of metallic layers. 91

Table 4.6: Mechanical durability and opto-electronic properties of various samples based on configuration H. 99

Table 5.1: Opto-electronic properties and durability of notable AR coating configurations. 101

LIST OF FIGURES

Figure 1.1: Example of destructive interference in a single-layer AR coating. 2

Figure 1.2: Crazing produced by thermal strain in a multilayer AR coating consisted of silica and zirconia. 3

Figure 2.1: Propagation of a beam of *p*-polarized light through a layer *j*, showing electric and magnetic fields travelling in distinct directions.. 12

Figure 2.2: Schema of dipole formation in metal nanoparticles by an external electric field.....18

Figure 2.3: Cluster of deposited material resting on a substrate with contact angle φ. 20

Figure 2.4: Qualitative plot of the free energy of a spherical cluster as a function of its radius derived from the capillary model and dependence on the state of supersaturation.....22

Figure 2.5: Planar FE-SEM images showing the morphological evolution of a) pure Ag and b) oxygen-doped Ag. 24

Figure 2.6: Structure zone diagram adapted to energetic deposition.. 28

Figure 2.7: *In situ* sheet resistance of a Ag film as a function of its nominal thickness, deposited on AZO coated substrates with Ni and Cr metallic seed layers of various thicknesses.....32

Figure 2.8: SEM imaging of 15 nm Ag and $Ag_{(Al)}$ films as-deposited and annealed at 300 °C.. .34

Figure 2.9: Numerical simulations showing the change in formation energy for N atom occupation at different sites as a function of distance from the Ag surface and change in surface energy as a function of N-occupied site density.. 36

Figure 2.10: *In situ* transmission photometry as a function of time and ellipsometry performed at 633 nm during deposition and etching of gold films. 38

Figure 2.11: Idealized representation of gold films just after coalescence and just before becoming discontinuous.....39

Figure 2.12: Optical micrographs of corrosion features after 10 days of mixed flowing gas exposure on a Ag mirror using a CrN_x adhesion layer, and a $NiCrN_x$ adhesion layer.....41

Figure 2.13: XPS depth profiles of as-deposited Ag mirrors using a CrN_x adhesion layer and a $NiCrN_x$ adhesion layer.. 45

Figure 3.1: Schematic representation of the e-beam evaporation system and ion source used. ...48

Figure 3.2: Schematic representation of the magnetron sputtering system used. 50

Figure 3.3: Example of R_V and T_V mapping of an AR coating produced with *Python*.....57

Figure 3.4: Schematic representation of saline corrosion test configured for use with *in situ* transmission spectrophotometry.....60

Figure 3.5: *In situ* transmission spectrophotometry measurement demonstrating the degradation of an unprotected AR stack during decelerated saline corrosion testing.....61

Figure 4.1: Modeled transmittance and reflectance spectra of AR coatings optimized by *Python* code and plotted with *OpenFilters* for fixed Ag thicknesses of 6 and 15 nm.....64

Figure 4.2: Nominal layer configurations A, B, C, used in different AR designs.. 64

Figure 4.3: Sheet resistance of samples deposited by e-beam in configuration A as a function of the deposition rate. 65

Figure 4.4: Sheet resistance and A_V of samples deposited by e-beam in configuration A as a function of the Ag layer thickness.....66

Figure 4.5: Transmittance and reflectance spectra of an AR coating in configuration B deposited on an Orma substrate.....67

Figure 4.6: Sheet resistance and A_V of 7-nm-thick passively-doped $Ag_{(O)}$ layers deposited by e-beam evaporation in configuration A as a function of O_2 flow. 68

Figure 4.7: Sheet resistance and A_V of 7-nm-thick IBA-doped $Ag_{(O)}$ layers deposited by e-beam evaporation in configuration A as a function of the O_2 composition of the IBA discharge gas. 69

Figure 4.8: Sheet resistance and A_V of stacks in configuration C, as a function of the Ag layer thickness, for underlying ZnO seed layers produced under different IAD accelerating voltages.....70

Figure 4.9: A_V of stacks in configuration C with 7-nm-thick Ag layers, as a function of the ZnO layer thickness. 71

Figure 4.10: Transmittance and reflectance spectra of AR coatings in configuration B and C. Both Ag layers were 9-nm-thick and deposited at a nominal rate of 3.1 Å/s. 72

Figure 4.11: Time-reversed fitting of the thickness of continuous Ag layers to *in situ* ellipsometry data demonstrating coalescence behavior for different substrate conditions. 73

Figure 4.12: Transmittance and reflectance spectra of an AR coating in configuration D. 75

Figure 4.13: Time-reversed fitting of the thickness of continuous $Ag_{(N)}$ layers to *in situ* ellipsometry data demonstrating coalescence behavior for different Ar:N_2 compositions. ... 77

Figure 4.14: Refractive index of $Ag_{(N)}$ layers sputtered in different Ar:N_2 compositions, obtained from *in situ* ellipsometry measurements. 77

Figure 4.15: Optical properties of $Ag_{(Al)}$ coatings with different Al content obtained by *ex situ* ellipsometry. 79

Figure 4.16: Time-reversed fitting of the thickness of continuous $Ag_{(Al)}$ layers to *in situ* ellipsometry data demonstrating coalescence behavior for different levels of Al content. ... 79

Figure 4.17: Time-reversed fitting of the thickness of continuous $Ag_{(N)}$ layers to *in situ* ellipsometry data demonstrating coalescence behavior for different metal-dielectric seed layer combinations. 80

Figure 4.18: A_V of different samples deposited on ZnO coated and B270 dielectric surfaces. 81

Figure 4.19: Photographs of an AR coating using Ag samples with Al protective layers following humidity testing at 60 °C and 80 °C. 83

Figure 4.20: : *In situ* transmission data in saline testing performed in a 200 g/L NaCl solution, for varying temperatures. 84

Figure 4.21: Critical degradation times for different concentrations of NaCl at room temperature and at 50 °C. 85

Figure 4.22: : *In situ* transmission data in decelerated saline corrosion testing for evaporated Ag layers, coated with SiO_2 deposited under different IAD conditions. 87

Figure 4.23: *In situ* transmission data in saline testing performed in decelerated testing conditions for sputtered Ag layers deposited with different dopants. 88

Figure 4.24: Transmittance and reflectance spectra of an AR coating in configuration E, before and after 20 minutes of saline corrosion testing in benchmark conditions. 92

Figure 4.25: Critical degradation times of samples deposited on ZnO and B270.....94

Figure 4.26: Nominal layer configurations F, G, used in Figure 4.25.. 94

Figure 4.27: Photographs of samples following corrosion testing showing different representative levels of degradation. 95

Figure 4.28: *In situ* transmission data in saline testing performed in benchmark conditions for coatings using co-sputtered and sequenced NiV_x-CrN_x seed layers. 97

Figure 4.29: Nominal layer configuration H used as the standard stack in Table 4.6. 98

Figure 5.1: Review of nominal layer configurations shown in Table 5.1 102

Figure 5.2: Fitting of the thickness of continuous Ag layers to *in situ* ellipsometry data demonstrating (de-)coalescence behavior during deposition and etching.....104

Figure 5.3: Fitting of the thickness of continuous $Ag_{(N)}$ layers to *in situ* ellipsometry data demonstrating (de-)coalescence behavior for samples deposited at 100 °C and etched at room temperature.....106

Figure 5.4: Nominal layer configuration of an AR design with high durability and optical performance potential and modeled optical properties 108

Figure 5.5: *S*1 curves for different wavelengths, measured during deposition and etching, and peak positions by resonant wavelength. 110

Figure A.1: *S*1 curves for different wavelengths, measured during deposition and etching, and peak positions by resonant wavelength.....124

LIST OF SYMBOLS AND ABBREVIATIONS

Abbreviations

AFM	Atomic force microscopy
ALD	Atomic layer deposition
AR	Antireflective
B270	Borosilicate glass
CIE	Commission internationale de l'éclairage
CRI	Custrom refractive index
DC	Direct current
DFT	Density functional theory
E-beam	Electron beam
FE-SEM	(Field-effect) scanning electron microscopy
FM	Frank-van der Merve (growth mode)
IAD	Ion assisted deposition
IPC	Ion pre-cleaning
IR	Infra-red
LSPR	Localized surface plasmon resonance
MSE	Mean square error
PID	Proportional integral derivative controller
PLC	Programmable logic controller
PVD	Physical vapor deposition
RF	Radio frequency
QCM	Quartz crystal microbalance
SZM	Structure zone model

TEM	Transmission electron microscopy
UV	Ultra-violet
VW	Volmer-Weber (growth mode)
XPS	X-ray photoelectron spectroscopy
XRD	X-ray diffraction

Materials and elements

Ag	Silver
$Ag_{(Al)}$	Aluminum doped silver
$Ag_{(O)}$	Oxygen doped silver
$Ag_{(N)}$	Nitrogen doped silver
Al	Aluminum
Ar	Argon
AZO	Aluminum doped zinc oxide
Cl	Chlorine
Cr	Chromium
Ni	Nickel
N	Nitrogen
O	Oxygen
Si_3N_4	Silicon nitride
SiO_2	Silicon dioxide
TiO_2	Titanium dioxide
V	Vanadium
ZnO	Zinc oxide
ZrO_2	Zirconium dioxide (Zirconia)

Symbols

A	Absorptance
A_V	Visual absorptance
D	Diffusion coefficient
D_0	Diffusion coefficient prefactor
E	Electric field
E_D	Energy barrier to diffusion
ΔG^*	Critical (variation of) free energy
H	Magnetic field
$I_{E/D}$	Emission/Discharge current
J	Impinging flux of film material
k_b	Boltzmann's constant
k	Complex component of the refractive index, extinction coefficient
N	Complex refractive index ($N = n - ik$)
n	Real component of the refractive index, real refractive index
P	Partial pressure (of film material in vapor phase)
P_0	Equilibrium pressure (of film material)
r^*	Critical cluster size
r	Reflected amplitude
R	Reflectance
R_V	Visual reflectance
R_V^{FS}	Front side visual reflectance (backside reflection supressed)
S	Supersaturation

S_1	Stokes parameter
t_{C1}	First critical degradation time, beginning of meaningful degradation
t_{C2}	Second critical degradation time, end of meaningful degradation
t	Transmitted amplitude
T	Transmittance
T_V	Visual transmittance
T_c	Constant temperature of compression
T_S	Substrate temperature
V_D	Discharge accelerating voltage
$\bar{y}$	Luminous efficiency
y_0	Optical admittance of the vacuum
Y	Relative luminance
γ	Collision frequency
Γ_{S-V}	Substrate-vacuum surface energy
Γ_{F-V}	Film-vacuum surface energy
Γ_{S-F}	Substrate-film surface energy
δ	Change of phase
Δ	Dephasing between polarizations
ε_0	Permittivity of the vacuum
ε	Dielectric function (interchangeable with relative permittivity)
ε_1	Real part of the dielectric function
ε_2	Complex part of the dielectric function
η	Tilted optical admittance

θ	Angle of propagation / incidence
λ	Wavelength
ρ	Resistivity
τ	Relaxation time
φ	Contact angle
$\Phi_{S,I}$	Power distribution (of an illuminant)
Ψ	Ratio of reflected polarization amplitudes
ω	Angular frequency
ω_0	Resonant frequency
ω_p	Plasma frequency
Ω/□	Ohms per square

LIST OF APPENDICES

APPENDIX A IN SITU ELLIPSOMETRY OF EARLY GROWTH 124

CHAPTER 1 INTRODUCTION

1.1 The material limitations of antireflection coatings

Although the public at large may not concern itself with the matter, common technologies are growing increasingly dependent on the use of light-manipulating optical coatings. As of 2018, the global market for optical coatings was valued at 14 billion USD and was expected to grow to above 25 billion USD by the end of 2025, driven by the use of said coatings in domains such as smart devices, energy saving construction (e.g. low-emissivity glass) and solar power generation [1]. As it stands, the aforementioned applications are bound to grow only more important in the years and decades beyond this projection, and the optical coating technologies present within them will likewise come to the fore, both from a practical and an economic standpoint.

Antireflective (AR) coatings account for the largest portion of the optical coatings market and their market is likewise expected to expand. in coming years [1], [2]. The primary market for AR coatings remains eyewear, but they are increasingly used in solar cells and electronics (which should come as no surprise, given that these are where optical filters in general are most used), in addition to the automotive industry, where reduced reflection in windshields, for example, can translate to gain from increased transmission as well as increased safety and ease due to decreased glare and unwanted reflections [2]–[5].

Of course, a multitude of applications begets a multitude of designs, each with their own advantages and shortcomings. To consider all the possible embodiments of AR coatings as a monolith would be misleading. That being said, the optical phenomena behind their antireflectivity are essentially the same.

The basic principle of AR coatings is to eliminate the reflected light through destructive interference, e.g. combining two beams of light with opposite phase and amplitude, resulting in the extinction of the combined beams [6], as shown in Figure 1.1. The goal, when designing an AR coating, is therefore to control the phase and amplitude of each wave as to make their sum have an amplitude smaller than that of the bare substrate – preferably to reduce it to zero, in most applications. At face value, that might seem to be a relatively straightforward task: a simple, one-layer design such as presented in Figure 1.1 works in theory – at a particular reference wavelength, with some material restrictions.

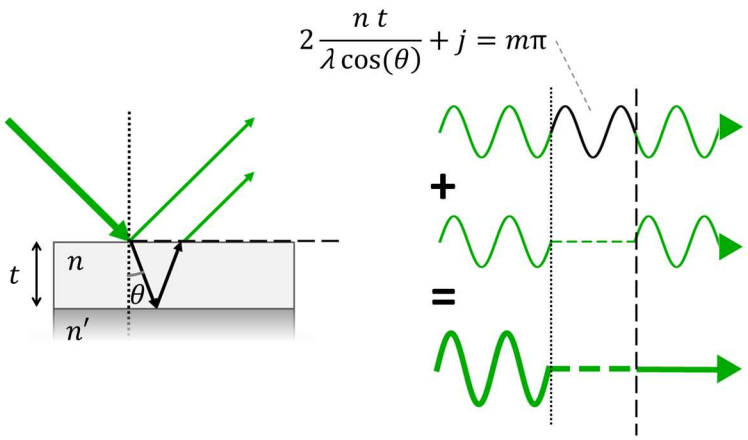

Figure 1.1: Example of destructive interference in a single-layer AR coating, where m is any odd integer and j accounts for any phase changes at the lower interface.

It should come as no great surprise that in application, things become a bit more complicated. Controlling the phase is relatively straightforward: at an interface between two dielectrics, the transmitted beam does not change phase and the reflected beam changes phase only if it reflects off a material with a higher refractive index than the incident medium, with a phase shift of π. The change in phase while traveling through a dielectric is merely a product of the thickness and the refractive index (i.e. the optical thickness), which can therefore be adjusted to tune the phase of the secondary reflection. However, the beam intensities, for a given incidence, are defined by the difference between the refractive indices about the interface and cannot be tuned otherwise, with the reflected intensity, or reflectance, *R*, given in equation [6], [7].

$$R = \left(\frac{n_1 - n_2}{n_1 + n_2}\right)^2 \qquad 1)$$

with n_1 and n_2 being the refractive indices of the two media about the interface. In the case of ophthalmic lenses, a majority of lenses are made with polymer substrates – of which a subsequent majority are made of CR39®, a versatile low-index polymer ($n \approx 1.5$). Likewise, standard glass materials have an index generally between 1.5 and 1.6 [5]. Of course, the surrounding media is air, with $n \approx 1$. Therefore, to have equal reflections which can cancel each other out, a single-layerAR coating should be made of a material with $n \approx 1.23$, but no such bulk material currently exists. Thus, to achieve high performance, broadband AR coatings, nano-structured single-layer coatings or multilayer AR coatings are used [3], [4], [6], [8].

In the former, a patterned or porous top layer is created such that the layer is largely composed of air, yet relatively uniform at the wavelength scale. This uniformity means the layer behaves as though its refractive index were a weighted average of air and the solid [3], [4], [6], [8]. Similarly, an array of dielectric cones can create an effective medium which is laterally uniform with a refractive index gradient which can progressively match the substrate and media [3]. These types of structures are generally lacking in mechanical durability, however, particularly patterned structures with low density [3], [4], [6]. Furthermore, these are susceptible to adsorption of water or other contaminants: as the reduced index relies on using small inclusions of air to lower to overall refractive index, if these fill with water or otherwise, the AR performance will drop [9]. Although this can be mitigated by using low-index hydrophobic materials such as MgF_2 [10], such coatings are unlikely to be practical for ophthalmic lenses which are frequently manipulated.

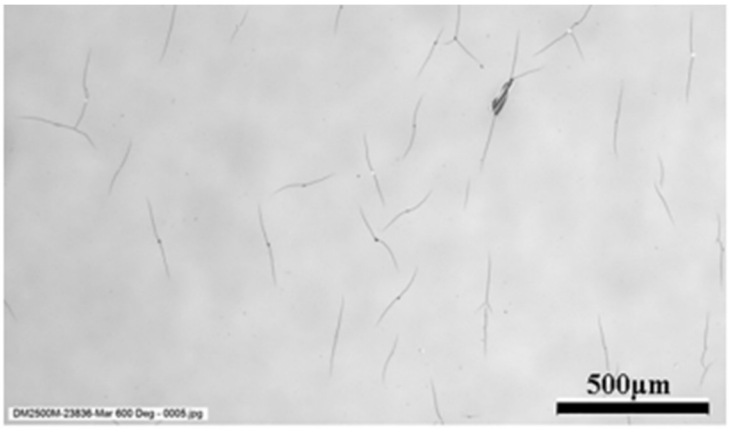

Figure 1.2: Crazing produced by thermal strain in a multilayer AR coating consisted of silica and zirconia, imaged by optical microscope. Adapted from [11].

Thus, in the ophthalmic industry, AR coatings are generally produced in a multilayer fashion. As a detailed explanation of interference phenomena in, and the resulting optical properties of, multilayer stacks is offered in section 2.1.2, a simple explanation will suffice at this time. As mentioned above, phase changes as a function of thickness and of wavelength. As such, a simple two-layer coating which efficiently lowers the reflectivity about a given wavelength can be supplemented with a layer which won't affect the behaviour at said target wavelength while broadening the AR effect. Broadband AR coatings can, therefore, be produced relatively easily with three or four layers, albeit adding more layers can help achieve a particularly strong AR effect

over a wider spectrum [5], [6]. That is not to say that adding layers will not inherently improve the AR. As a matter of fact, the opposite might be true: additional coating layers will inevitably bring about additional production costs and may have unintended consequences on other aspects of the final product [5], [6]. Polymer substrates, as used in the ophthalmic industry, are sensitive to expansion by water absorption and thermal expansion, whereas the dielectric coating layers tend to have higher hardness, brittleness and lower expansion (of any kind). The resulting mismatch in mechanical properties can cause crazing cracks and delamination within the coating (as shown in Figure 1.2), leading to shorter coating lifetimes [12], [13]. Again, optical performance and durability are throttled by material limitations.

An ideal multilayer AR coating would thus have few layers, but still keep broadband antireflectivity; one means of achieving this may be through the addition of a *metallic* layer. Although it may seem strange to take materials used in mirrors to make a coating which is *anti*reflective, metals have a number of useful properties. The mechanical advantage is quite straightforward: although metals aren't as expansive as polymers [14], they are not brittle like dielectrics and should help accommodate strain.

Optically, metallic layers distinguish themselves by their conductivity. In dielectric materials, electrons are bound to their respective cores, and the electric field of a beam of light will make them oscillate but not create an internal current [15]. Metals, however, have an ample supply of free electrons whose motion will follow the field, causing high reflection and dissipating the transmitted beam's energy through joule heating – thus causing absorption [16]. The induced current variation interacts with the magnetic field, resulting in optical properties that cannot be achieved in dielectrics: this can be represented by considering metals as having a complex refractive index, which produces waves with a complex wavenumber [6], [7], [16].

This may not seem particularly exciting until one realizes how many of the limitations imposed in the previous discussion of AR coatings are a consequence of limiting oneself to dielectrics. The conductivity of a metal makes for reflection amplitudes which aren't tightly bound to the real part of the refractive index [7]. Just like that, amplitudes about the interface are no longer strictly defined by the ratio of dielectric refractive indices. Phase is also freed of the rigid values observed in all-dielectric coatings: both reflected and transmitted beams change phase at a metal-dielectric

interface and the changes are no longer confined to values of 0 or π [7], [8]. Amplitude and phase can also be tuned by controlling the optical path length within the metal film [7], [17].

The optical versatility offered by these materials can make them a useful tool, but their implementation is no simple thing. Usability is threatened by technical challenges in the very deposition of the films, optical losses by absorption and various modes of chemical and mechanical degradation – the overcoming of which constitutes the goal of this research.

1.2 Context of the research

Although it may be an unintuitive idea at first glance, the inclusion of metal layers in AR coatings, and in optical interference filters in general, provides a versatile new tool by which to control light in the field of ophthalmic coatings. Furthermore, metal films have mechanical and electrical properties that could allow these coatings to be multi-functional: metal coatings could prove an alternative to brittle transparent conductive oxides such as ITO, for flexible (or simply more mechanically durable) transparent electrodes, for example [18]. Many products where AR coatings are currently in use already incorporate transparent conductors, such as solar cells, touchscreens and even eyeglasses, where they dissipate charges that would otherwise lead to dust accumulation [2], [5]. Combining the AR and conductive coatings in one simple design would likely be advantageous.

Essilor, one of the world's leading eyewear companies, began developing and identifying the challenges associated with creating a broadband antireflective coating in the visible range suitable for everyday use in eyewear, using a dielectric-metal-dielectric structure, and reached out to MIC-CSE, the Multisectorial Industrial Research Chair in Coatings and Surface Engineering, to collaborate in this endeavour.

First, suitable metals were identified; for optical applications, metals with a high k/n ratio (k, the extinction coefficient, is the complex component of the refractive index, whereas n is its real component) have been shown to have the most potential [19]. Essentially, all the interesting optical behaviors of metals emerge from their conductivity, and therefore it should come as no surprise that the metals with the best optical properties are the most conductive: that is the noble metals,

gold, copper and silver [20], [21]. Silver (Ag) was made the primary object of this work on the grounds that it has the highest conductivity and, naturally, the highest k/n ratio.

The nobility of silver incurs problems of it own, however. Due to their relatively high surface energy and weak adhesion to dielectrics, silver coatings tend to form following a Volmer-Weber (VW) growth mode [22]. This means that deposited silver will be more likely to bond with itself than with the substrate, and form island-like clusters on the surface which will remain separate until they are large enough to coalesce into a continuous film. Its quite simple to see that if the film is too thick it will be highly absorbant. However less intuitive, the same is true for films which are too thin: indeed, if a silver film is discontinuous, the free electrons within the clusters oscillate under the influence of the electric field with preferential modes defined by the cluster size, leading to a phenomenon known as localized plasmon resonance (LSPR), which causes enhanced absorption and scattering in the visible spectrum [15]. Therefore, to maximize transparency, film growth must be controlled to achieve film coalescence at low thickness, by using appropriate process parameters or by depositing the silver layer on dielectrics with high surface energy or an affinity for silver, such as zinc oxide [23].

Finally, AR coatings for the ophthalmic industry must be durable. As mentioned previously, silver and most other metals bond poorly with dielectric surfaces, leading to adhesion issues as well as promoting the VW growth mode [24]. Of course, the mechanical advantages offered by a metallic layer will be null if it simply delaminates under strain, and thus particular care must be given to ensuring the adhesion of the film. Equally, if not more important is the chemical durability of the silver film. Silver is quickly corroded in the presence of sulfur or chlorine and may oxidise as well [25]. These issues are commonly resolved by using thin metallic protective coatings which may improve adhesion and inhibit corrosion.

To resume, AR coatings making use of a silver layer could achieve broadband antireflection while providing a mechanically durable conductive layer. However, to make such a coating viable in application, the growth of the silver film must be controlled to achieve a continuous film at low thicknesses and a high standard of environmental durability must be achieved.

1.3 Objectives

Therefore, the objective of this project was to study AR coatings containing Ag films deposited on glass and on polymer substrates in order to explore their optical performance and assess their environmental and mechanical durability. In order to focus on the distinct challenges offered by this project, however, two secondary objectives were defined as so:

1. Deposit continuous thin silver films under different conditions, assess the resulting optical properties and model the performance of optimized AR coatings.
2. Evaluate and improve the environmental and mechanical durability of complete AR coatings.

To quantify these goals, it was determined that coatings should have a visual reflectance (R_V) below 1 %, preferably below 0.5 %, visual transmittance (T_V) above 85%, preferably above 90 %, and should pass specific durability tests (described in chapter 3) without losing their optical performance. Of course, the underlying challenge was to achieve both goals simultaneously, i.e. to protect the AR coatings without forsaking their optical performance, and to optimize the growth and optical quality of silver without introducing vulnerabilities. To that effect, coating designs were to be kept below a total thickness of 150 nm, preferably 100 nm, to keep the thermo-mechanic advantage of thin coatings.

1.4 Outline

The work presented is to be broken down into 5 chapters, the first of which is this introduction. Chapter 2 will present the theory relevant to the work as well as review some the published findings which have guided this project. First, the theory of propagation of light through a thin film interference filter is explained. The human eye's sensitivity to light and the related considerations in designing optical filters for ophthalmic applications are quickly presented, as well as details on the optics of continuous and discontinuous metals. Following this, the theory of film growth, with specific attention to silver is presented. This naturally leads into a review of the techniques used to control silver growth and morphology, as well as another small section pertaining to the durability of silver films.

Chapter 3 describes the methodology used throughout the project, detailing the deposition methods used and relating these to the film growth theory exposed in the previous chapter. Following this, the characterization methods used to evaluate sample quality are presented. Optical characterization through spectroscopic ellipsometry and photometry are presented as well as modeling approaches and how each characterization tool plays into improving or confirming the modeling results. The durability tests which were used, most of which are standard in the eyewear industry, are then detailed. Finally, complementary characterization methods used alongside these are presented.

Chapter 4 presents and discusses the main body of results in light of current literature, loosely divided as optical performance and characterization results on one hand and durability testing and improvement on the other. With a global view of the effect of the many process and architecture variations on both optical properties and durability, the overall performance of different AR stacks incorporating the most promising elements of the each of the previous sections is evaluated and discussed.

Finally, chapter 5 concludes with a broad overview of the project, highlighting important results and outlining perspectives for future work.

CHAPTER 2 THEORY & LITERATURE REVIEW

2.1 Optical considerations

This thesis concerns itself largely with the material aspects of metal films, the control of their growth, the resultant structures and properties, but the primary motivation behind this material investigation is an optical one, and behind this is a human one. This section will be structured to lead from the human to the material, by first presenting how humans perceive light, allowing to understand how an antireflection coating meant for human eyes should be designed. The mathematical description of light propagation through a stack of thin films supplies the tools to design such AR coatings with a given set of materials and, finally, the important optical properties of the materials of this study, namely the key material, silver, are discussed.

2.1.1 Photometry and human perception of light

This section shall focus on the basics of how observers perceive brightness, and how the optical properties of objects can tailor stimulus, and therefore, perception. Although color plays an important role in the field of ophthalmics (the AR coatings used in the field being no exception), a full description of the adaptivity of the eye to light and its perception of color is beyond the scope of this section. A reader interested in learning more about these topics may refer to *Colorimetry: Fundamentals & Applications*, by Ohta and Robertson [26], which is the primary reference of this section.

Brightness, however, is somewhat hard to quantify: the eye adapts to the lighting conditions it is currently subjected to, which can dramatically change what is perceived as bright. In this work, only observers in photopic vision conditions are considered: being the most representative of the average person's daily experience, it has been established as the default for photometric measurements by the Commission Internationale de l'Éclairage (CIE) [27].

In this work, absolute radiometric and photometric quantities will not be considered, as the reflectance of a coating is expressed in terms relative to the total incident intensity. Thus, the eye's sensitivity can be described using spectral luminous efficiency, $\bar{y}(\lambda)$, which designates the relative brightness perceived for a fixed amount of radiant energy, as a function of the wavelength, λ. The CIE standard photometric observer represents the average spectral luminous efficiency measured

from roughly 250 subjects, therefore providing a representative, if not perfect, means to generalize the sensitivity of the human eye to different wavelengths. Similarly, the CIE has established standardized illuminants which describe the relative spectral power distributions, $\Phi_{S,I}(\lambda)$, of given sources of illumination [28]. In this work, if not specified otherwise, the standard illuminant D65, intended to represent average daylight and typically used in ophthalmics, is used [5], [29]. With this, one can use equation 2 to calculate the relative luminance Y, a unitless measure of the potential[1] brightness perceived upon observation of a light source [26].

$$Y = \int \Phi_{S,I}(\lambda)\, \bar{y}(\lambda)\, \mathrm{d}\lambda \qquad 2)$$

That being said, the vast majority of materials in day-to-day life do not produce visible light unprompted: they can, however, reflect, transmit or absorb the light which illuminates them. As such, the brightness transmitted, absorbed, or reflected by an object can be obtained from equation 2 by adding the object's spectral reflectance, transmittance or absorbtance, $R(\lambda)$, $T(\lambda)$ or $A(\lambda)$, respectively, to the interior of the integral [5], [30]. By comparing this value to that of the illuminant, a measure of the "brightness reflectance", R_V, is obtained, as shown in equation 3.

$$R_V = \frac{\int \Phi_{S,I}(\lambda)\, \bar{y}(\lambda)\, R(\lambda)\, \mathrm{d}\lambda}{\int \Phi_{S,I}(\lambda)\, \bar{y}(\lambda)\, \mathrm{d}\lambda} \qquad 3)$$

R_V is the luminous reflectance in the visual range, or *visual reflectance*. One understands this to be the perceived brightness of the reflection from the studied object – and thus is perfectly suited as a figure of merit for a coating meant to reduce visible reflection. Likewise, $R(\lambda)$ can be replaced by $T(\lambda)$ or $A(\lambda)$ in equation 3 to obtain T_V or A_V, which are similarly useful to describe how much perceivable light is transmitted through the coating or lost to absorption [5]. Moreover, it shows that an AR coating should show low reflection over a broad range, but it is most important that it

[1] Y can be converted to an absolute value of luminous flux by multiplying it by the maximum values of the spectral radiant flux and spectral luminous efficacy, which respectively describe the flux of energy of the light and a sensitivity in lumens/W [26]. Thus, it is 'potential' brightness, contingent on the light's power and the observer's sensitivity.

minimizes reflection around the peak of the eye's sensitivity (at 555 nm), and depending on the lighting, have lower reflectance in regions of the spectrum where the illuminant is high.

2.1.2 Propagation and interference

With the means to evaluate how the eye will perceive an object with a given reflectance, $R(\lambda)$, explicited in the previous section, one now needs to have the tools to tailor $R(\lambda)$ by means of a stack of thin-film coatings.

To understand what occurs when light traverses a series of interfaces, one must first consider what occurs at an interface between any two given materials. Assuming a harmonic transversal plane wave, both the magnetic and electric fields will have a component parallel to the interface: naturally, they must remain continuous at the boundary, despite the different material properties on either side [6], [7]. Solving the equation system formed by equating the incident, transmitted and reflected amplitudes at the interface is not only too long to be worth included in this work, particularly in the general case, it simply results in the well-known Fresnel equations [6], [7].

Taking $\eta = N\, y_0/\cos(\theta)$ for p-polarized light, or $\eta = N\, y_0 \cos(\theta)$ for s-polarized light:

$$r = \frac{\eta_i - \eta_e}{\eta_i + \eta_e} \qquad 4\text{ a)}$$

$$t = \frac{2\eta_i}{\eta_i + \eta_e} \qquad 4\text{ b)}$$

Here η_i and η_e are the tilted optical admittances in the incident and exit media, respectively. The angles, which may be complex, are given for the exit media by Snell's law. Finally, although this should not be an issue in this work, the formulation above is only valid for non-magnetic media. Otherwise, N and y_0 (the optical admittance of the vacuum) should be substituted with y, the optical admittance of the medium [6], [31].

With these equations, one can find the reflected and transmitted amplitudes resulting of each beam at a given interface, as well as any dephasing induced at the interface, included in the amplitude as a change of sign for dielectrics, or as a complex value for metallic layers.

Now that the behavior on a beam at an interface has been explicited, one now needs to account for the effect on the phase and amplitude of a given beam as it propagates to the next interface. One

finds the angle of propagation in a layer j with the law of reflection for reflected beams and Snell's law for transmitted beams; with the layer's thickness, d_j, and its refractive index, $N_j(\lambda)$, the optical length can be obtained. Finally, this is converted into a change of phase, δ_j, as shown in equation 5, with complex-valued refractive indices exponentially decreasing the beam amplitude as it is transmitted through the layer [6].

$$\delta_j = 2\pi \frac{N_j d_j \cos(\theta_j)}{\lambda} \qquad 5)$$

A wave reaching a new interface can be subjected to new boundary conditions, and the process can be repeated, starting with Fresnel's equations being reapplied. However, rather than repeating this process ad infinitum, the overall response of a layer *j* can be obtained by considering the tangential field components traveling towards the incident medium (E^-, H^-) and exit medium (E^+, H^+) of each field separately (as illustrated in Figure 2.1). Taking the sum of the fields going in each direction, at each side of each interface, the field totals in the incident medium (E_i, H_i) can be written as a function of field totals in the exit medium (E_e, H_e) [6]. This is a somewhat complex procedure, which fortunately yields a much easier to use, elegant set of equations; these are resumed by the matrix expression given in equation 6.

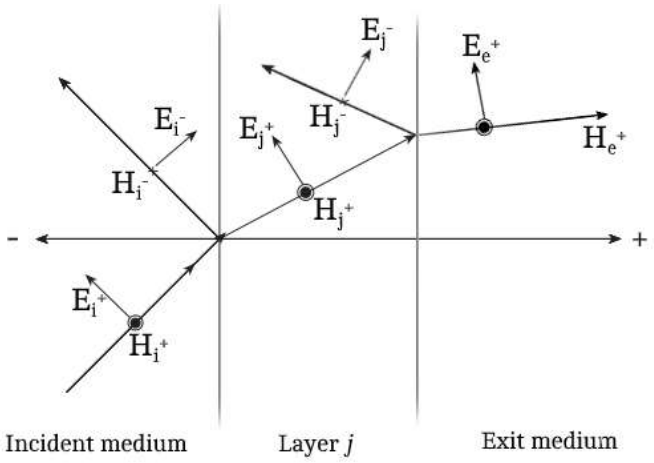

Figure 2.1: Propagation of a beam of *p*-polarized light through a layer *j*, showing electric and magnetic fields travelling in distinct directions. Adapted from [6].

The advantage of this approach is that the total fields on either side of the layer j are related by multiplication of the layer's associated transfer matrix, M_j – and adding a layer simply adds a

matrix multiplication, equally shown in equation 6. As such, the total product of these matrices results in the stack transfer matrix, M_S, from which the optical properties of an assembly of m layers can be derived [6], [32].

$$\frac{1}{E_e}\begin{bmatrix}E_i\\H_i\end{bmatrix} = \underbrace{\prod_{j=m}^{1}\overbrace{\begin{bmatrix}cos(\delta) & i\,sin(\delta)/\eta\\ i\,\eta\,sin(\delta) & cos(\delta)\end{bmatrix}}^{M_j}}_{M_S}\begin{bmatrix}1\\\eta_e\end{bmatrix} \quad 6)$$

The reflected amplitude can be obtained by taking the effective admittance of the stack and inserting it into the Fresnel equations adapted to admittance, following which transmittance can de determined directly from irradiance considerations [6]. For the sake of simplicity, these steps are forgone; the reflected and transmitted amplitudes for the stack are given by equations 7 and 8 [32].

Taking $M_S = \begin{bmatrix}m_{11} & m_{12}\\ m_{21} & m_{22}\end{bmatrix}$:

$$r = \frac{\eta_i m_{11} - \eta_e m_{22} + \eta_i\eta_e m_{12} - m_{21}}{\eta_i m_{11} + \eta_e m_{22} + \eta_i\eta_e m_{12} + m_{21}} \quad 7)$$

$$t = \frac{2\eta_i}{\eta_i m_{11} + \eta_e m_{22} + \eta_i\eta_e m_{12} + m_{21}} \quad 8)$$

The associated intensities are obtained straightforwardly, by taking the square of their norms. The absorptance is then obtained indirectly, by isolating A in the total intensity, $R + T + A = 1$ [6], [32]. As there are separate expression for each polarization, one should treat *s*- and *p*-polarized light separately, then average R, T, and A to consider unpolarized light.

With these tools, one can determine the reflectance, transmittance or absorbance of any stack of films with elementary input data: assuming that the incident angle is known, and that the approximation presented in equation 4 remains valid, the thickness of the layers and the refractive indices of each medium are all that is needed to ascertain the optical properties of the stack as a whole.

Albeit very versatile, this method does have its limitations: working under the implicit assumption that all interfaces are plane and parallel means that roughness and other imperfections are not considered [33]. Moreover, this only applies for coherent media, which implies layer thicknesses of the wavelength scale must be used: common substrates cannot be treated as a layer, and must be

considered as the exit medium, with additional considerations required to appropriately treat the backside [6], [32]. The backside contribution may be added as a geometrical series or adjusted with random phase inclusions, depending on the level of coherence – common glass substrates can often have their backside reflection approximated as a fixed amount, however [32], [34].

There are different approaches taken in this regard just as there are different approaches taken with transfer matrixes [6], [16], [32]–[36]. As with any model, it is important that the model used is appropriate for the situation it is meant to describe – the choices made and the justifications for them, in this work, will be detailed in Chapter 3.

2.1.3 The optical properties of materials

One can now focus on the last few theoretical considerations needed to link the performance of eyeglasses to materials and processes: with the means to determine R, T and A, given a known incidence of light and the optical properties of the materials used, one now needs to understand how these optical properties emerge from the material structure.

The dielectric function, (interchangeable with the relative permittivity,) ε, is directly related to the complex refractive index through the relation $\varepsilon = N^2$. However, as useful as this relation is, in straightforwardly relating the electronic structure and the refractive index, it is not particularly telling. Therefore, it is of interest, both for practical applications and additional insight, to separate the dielectric function into real and complex components such as $\varepsilon = \varepsilon_1 + i\varepsilon_2$ [15]. With this, n and k are defined by equation 9.

$$n = \left(\frac{\varepsilon_1}{2} + \frac{\sqrt{\varepsilon_1^2 + \varepsilon_2^2}}{2} \right)^{1/2} \tag{9 a}$$

$$k = \frac{\varepsilon_2}{2n} \tag{9 b}$$

One will recall that it is the addition of complex refractive indices that distinguishes metals from dielectrics and makes them of interest for optical applications, and that more specifically, the k/n ratio has been shown to be a useful figure of merit for these metals [6], [19]. Now, all that is needed is to describe ε in material terms.

The Drude model, albeit somewhat over-simplified, is a good starting point from which to begin describing metals. It assumes a sea of free valence (or conduction) electrons moving freely through an immobile metal lattice composed of the positive ion cores and tightly bound core electrons [15]. In this it is implied that (despite being confined to the metal lattice,) the positive ions and other electrons of the metal do not exert an electric field on a given electron, and thus its motion will be driven by the external electric field. In such case, motion driven by an external field will be damped by the internal system. The precise mechanism of this damping is not important, as long as it helps describe the system; to paraphrase Ashcroft and Mermin, the important part is that there is *a* mechanism causing damping. The original model assumes collisions with the positive ion cores at a frequency $\gamma = 1/\tau$, where τ is referred to as the relaxation time [15], [37]. This introduces speed dependant damping, resulting in motion as described by equation 10.

$$m\ddot{\boldsymbol{x}} + m\gamma\dot{\boldsymbol{x}} = -e\boldsymbol{E} \tag{10}$$

where x, m and e are the electron displacement, mass and charge, respectively, and E is the external electric field. Assuming that the electric field is harmonic, one can find a general expression for x relativly easily by assuming it's of the form $x(t) = x_0 e^{-iwt}$. The polarization is a simple function of the of the displacement, which is expressed in terms of E, allowing to describe the total displacement field in terms of E as well [15]. As such, the dielectric function, can be described by equation 11.

$$\varepsilon(\omega) = 1 - \frac{\omega_p^2}{\omega^2 + i\gamma\omega} \text{ where: } \omega_p^2 = \frac{ne^2}{\varepsilon_0 m} \tag{11}$$

where ω is the frequency of the incident wave, n is the free electron density and ω_p is the plasma frequency, which is a measure of the natural oscillation frequency of the free electron sea. As the frequency of incident light approaches ω_p, it becomes increasingly difficult for electron motion to follow the external field. Beyond it, the electron sea can no longer keep up with the external field, and the metal behaves like a dielectric: of course, with damping taken into consideration, this change is not as sudden as it is in theory [15], [37].

As mentioned in the introduction, electrons in dielectrics are bound in certain states. This does not mean that they're immobile, of course: simply that they're subjected to a restoring force. One can

consider the equation of motion of an electron in a given bound state by simply adding a term of the form $m\omega_0^2\boldsymbol{x}$ to the left half of equation 10, which is that of a restoring force. One can similarly adapt equation 11 simply by subtracting ω_0^2 from the denominator, which accounts for the resonance frequency introduced by the presence of said restoring force, and assuming n now refers to the density of electrons in that particular state [7]. To avoid confusion ω_p will be replaced with ω_j to refer to the "plasma frequency" of electrons in a given state j. One can now compare the real and complex parts of the general dielectric functions of metals (ε_m) and dielectrics (ε_d) as shown in equation 12.

$$\varepsilon_m = \overbrace{1 - \frac{\omega_p^2\tau^2}{1+\omega^2\tau^2}}^{\varepsilon_1} + i\overbrace{\frac{\omega_p^2\tau}{\omega(1+\omega^2\tau^2)}}^{\varepsilon_2} \tag{12a}$$

$$\varepsilon_d = \overbrace{1 - \frac{(\omega^2-\omega_0^2)\omega_j^2\tau^2}{\omega^2+(\omega^2-\omega_0^2)^2\tau^2}}^{\varepsilon_1} + i\overbrace{\frac{\omega\omega_j^2\tau}{\omega^2+(\omega^2-\omega_0^2)^2\tau^2}}^{\varepsilon_2} \tag{12b}$$

Observing the real part of the dielectric function, one notices that (below the plasma frequency) metals have a negative ε_1. More interesting still is that if the damping within the metal is considered negligible, such that $\tau \to \infty$, ε_2 will also become negligible, but ε_1 will retain its negative, metallic character. This shows that while the complex refractive index k is intrinsic to metallic behavior, the complex dielectric function, ε_2, is not Returning to equation 9 one will also notice that a strongly negative ε_1, which will occur for higher plasma frequencies, and therefore higher densities of conduction electrons, will push n to smaller values, particularly if the norm of ε_2 is relatively small. Therefore, the k/n figure of merit can be rephrased as a requirement for a highly conductive metal with low damping, and as in plasmonics, silver is the material of choice [38].

Studying ε_d at low frequencies, behavior is intuitive: ε_1 is positive, ε_2 is small. Nearing the resonant frequency ω_0, however, behavior changes significantly: ε_1 approaches unit value, regardless of material properties, and ε_2 peaks. This behavior, which causes anomalous dispersion at these frequencies is simply due to enhanced loss due to high oscillation amplitudes when driving electrons at their preferred frequency. That being said, one will recall that it was specified that this was the formula for the electrons in a given state – with no great loss of generality, one can affirm

that no such state will dominate the material's overall dielectric function, which is a sum of the oscillating contributions of each state, weighed by their density, included in ω_j [7]. Naturally, exceptional cases, such as at very high frequencies, where plasma-like or non-linear behaviors can occur, need not be considered in the context of this work.

Dielectric materials and their optical properties are certainly of interest; however, their properties are well known in the context of AR coatings and the primary focus of this work lies in the implementation and control of the silver film's properties. Fortunately, the tools used to describe dielectrics are quite useful in describing real metals as well. Of course, only a fraction of electrons in a given metal can be considered free: bound states behave following the same general form as in dielectrics (i.e. $\omega_j^2/(\omega^2 - \omega_0^2 + i\gamma\omega)$, commonly called a Lorentz oscillator) [15]. For the sake of simplicity, most of these can be incorporated into effective background functions (see section 3.2.2). Others, such as the interband transitions of silver, which cause a sharp rise of ε_2 for energies above $\approx$ 4 eV, must be accounted for in a distinct manner but have little impact in the visible spectrum [15].

The contributions to the dielectric function which emerge from the inherent structure of silver are relatively easy to consider, mainly because they do no readily change from experiment to experiment. Even if the means of modelling them does, one understands that the underlying atomic structure has not fundamentally changed. This is not the case for contributions arising from the nanostructure. Metallic inclusions in a dielectric medium essentially act as reservoirs of free electrons, which are readily displaced by an external electric field. However, at small scales, of the order of the wavelength, the body of free electrons can be collectively displaced, forming a plasmon. The plasmon carries a negative charge density, whereas the background of positive ion cores depleted of conduction electrons creates a positive charge density, forming a dipole as illustrated in figure [15], [39].

A discontinuous metal layer will thus display enhanced extinction around the resonant frequencies, which, for silver nanoparticles, lie in visible range despite variation due to the parameters mentioned above. As such, even though certain nanostructured metals films have proven to make high quality AR coatings [8], [40], this work requires continuous metal layers to maintain a highly transparent coating in the visible range.

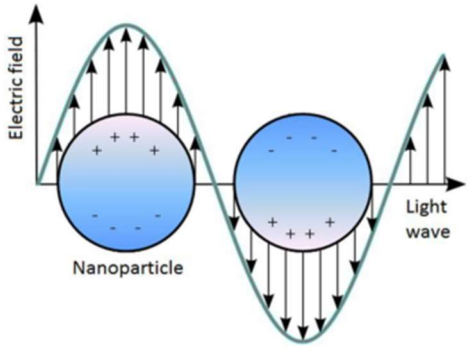

Figure 2.2: Schema of dipole formation in metal nanoparticles by an external electric field. Reproduced from [39].

LSPR does not only occur in discontinuous films, nor is it the only way the nanostructure affects the optical properties. Free surfaces at film edges and at grain boundaries can also enable resonance and degrade optical properties [41], [42]. Not considering plasmon resonance, defect density, surface roughness and grain boundaries have been shown to have increasingly important effects on film properties [43], as they supply additional scattering sites for electrons – similarly higher temperature operation may increase phonon scattering. Both of these will increase the scattering frequency γ, which increases both ε_1 and ε_2 as one can see from equations 11 and 12, leading to degradation of the optical properties [44], [45].

2.2 The deposition of silver films

The previous section supplied all the necessary theory to understand and conceptualize a metallic AR, as well as appreciate the extent to which control of the nanostructure is important to its performance. This section focuses on the means available to control said structure through the deposition process. It begins by presenting the challenge presented by the island growth mode of silver films, then discusses which of the main parameters of physical vapor deposition (PVD) processes can be used to address them. With theoretical understanding of the problem and of potential solutions well exposed, techniques used to control the growth mode are then presented.

2.2.1 Island growth

To gain a conceptual understanding of island growth, one may first approach the problem under the approximation that the system is in a state of local thermodynamic equilibrium – with a more

complete picture coming into view when parameters intrinsic to the deposition process are introduced [46].

Consider therefore that the system is driven to minimize its free energy: given a fixed contribution coming from the volume, this translates as a requirement to minimize the surface free energy, Γ. Taking Γ as the energy per unit area required to form a new interface, one can intuitively associate it to the binding energy; the creation of a new interface within a volume implies breaking the bonds with which it intersects, and thus the strength and density of bonds at the interface are closely linked to Γ [22], [46].

For a deposition on a given substrate, where impinging atoms have enough energy to diffuse to low-energy sites, they will occupy these before defaulting to other, less advantageous positions. In this situation, if the adatoms bind more strongly with the substrate than with themselves, they will cover the entire substrate before forming a second layer: this is known as Frank-van der Merve (FM) or layer-by-layer growth [22], [46]. In the alternate scenario where adatoms bind more strongly with each other than with the substrate, they will condensate into island-like structures, with additional impinging adatoms tending to join existing islands as a means to minimise the surface-volume ratio. This is the island growth mode which has been referred to throughout this work, which is also known as the Volmer-Weber (VW) growth mode [22], [46].

To express this in terms of surface energy, both simply and quantitatively, one can use the capillary model of nucleation, in which the surface energy of the adatoms is likened to the surface tension of a liquid droplet. Expressing energy per surface are as force per length, and assuming this force is parallel with the surface its associated to, one can equate the components of said forces which are parallel to the substrate at the perimeter of the substrate-film interface, resulting in equation 13, also known as Young's equation, and illustrated in Figure 2.3 [22], [46].

$$\Gamma_{S-V} = \Gamma_{F-V} \cos\varphi + \Gamma_{S-F} \qquad 13)$$

where Γ_{S-V}, Γ_{F-V} and Γ_{S-F} are the surface energies of the substrate-vacuum, film-vacuum and substrate-film interfaces respectively, and φ is the contact angle of the film at the substrate interface, as shown in Figure 2.3.

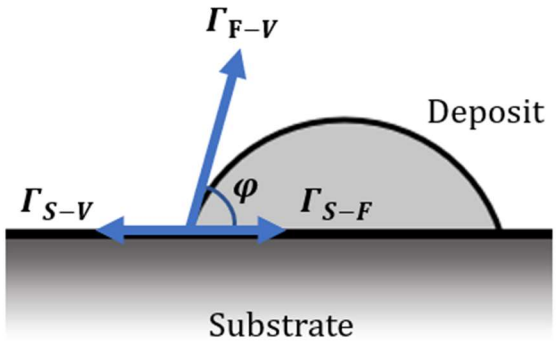

Figure 2.3: Cluster of deposited material resting on a substrate with contact angle φ with surface energies Γ_{S-V}, Γ_{F-V} and Γ_{S-F} represented as forces at the substrate-film surface boundary.

From Figure 2.3 one can see that if there is total coverage (FM growth mode) if $\varphi = 0$, and islands will be accentuated as φ increases. Then, $\cos\varphi$ would be unity for FM growth and below this threshold for VW growth: growth mode can then be approximated from the surface energies as shown in equation 14.

$$\begin{aligned} \Gamma_{S-V} &< \Gamma_{F-V} + \Gamma_{S-F} \quad : \quad \text{VW growth} \\ \Gamma_{S-V} &\geq \Gamma_{F-V} + \Gamma_{S-F} \quad : \quad \text{FM growth} \end{aligned} \tag{14}$$

Of course, this is not as clear-cut a binary as this model would have one believe: low contact angles may result in a very flat coating not unlike those produced by FM growth and the development used here has relied on the underlying assumption that adatoms can diffuse to preferential sites, which may not be the case, causing condensation even in FM conditions. Moreover, shifting conditions can change the growth mode, such as in Stranski-Krastanov (SK) growth, where accumulated strain or the loss of the substrate's effect causes a coating to shift from layer-by-layer to island growth [22], [46], [47]. Nevertheless, one can see how, having fairly high surface energy compared to most glasses [47], [48], as well as poor adhesion on them [24], silver will tend to create island-like coatings. As for the real shape of islands beyond this approximation, the Wulff relation, which says that the distance between two parallel facets of a crystal increases linearly with the surface energy of the facets, implies that the equilibrium shape of a given crystal will minimis the total surface energy, thus leading to configurations which maximise the surface area of crystal orientations with lower surface energy, and vice-versa [49]. Thus, the lowest-energy surface should

be parallel to the substrate surface, barring a specific affinity with the substrate, with the general "flatness" of the cluster defined largely by the growth mode and its more specific shape by the minimisation of its own surface energy.

This is valid only in equilibrium conditions, however, resulting in a balance between desorption and adsorption processes. Of course, it is not the balance between these, but the lack thereof, that defines film growth. A convenient way to represent this is with the supersaturation, $S = P/P_0$, where P is the partial pressure of the film material in the vapor phase and P_0 is the equilibrium vapor pressure of the deposited film [22], [46]. The basic growth modes were derived in equilibrium conditions, such that $P = P_0$ and $S = 1$. Borrowing the formalism of the compression of an ideal gas, Lüth adds a term accounting for the effect of non-equilibrium conditions on the free energy of deposited and vapor-phase film material, given by equation 15 [46].

$$\begin{aligned} \Gamma_{S-V} &< \Gamma_{F-V} + \Gamma_{S-F} - Ck_bT_c \ln(S) \quad : \quad \text{VW growth} \\ \Gamma_{S-V} &\geq \Gamma_{F-V} + \Gamma_{S-F} - Ck_bT_c \ln(S) \quad : \quad \text{FM growth} \end{aligned} \tag{15}$$

where C is a constant related to the density of adatoms [46]. T_c is a constant temperature associated to the transition from the gas phase to the solid phase.

Looking back to equation 15, one might ponder that the distinction between growth modes is based on whether the free energy is lowered by covering the substrate or not, and thus, why island growth occurs at all, if it requires a net increase of free energy. This is simply the free energy associated with the formation of *surfaces* however, with the last term accounting for the "compression" of a single adatom from the vapor phase joining the surface. The formation of an ordered *volume*, however, lowers the system's free energy, lowering the energy required for formation. As illustrated in Figure 2.4, the increase of energy due to the formation of surfaces is more important at small sizes where the surface-to-volume ratio is high; this trend changes as clusters become larger, leading to a free energy barrier for the formation of clusters. A critical size can be found; above it clusters will be stable and below it they will desorb from the surface [22], [46], [50].

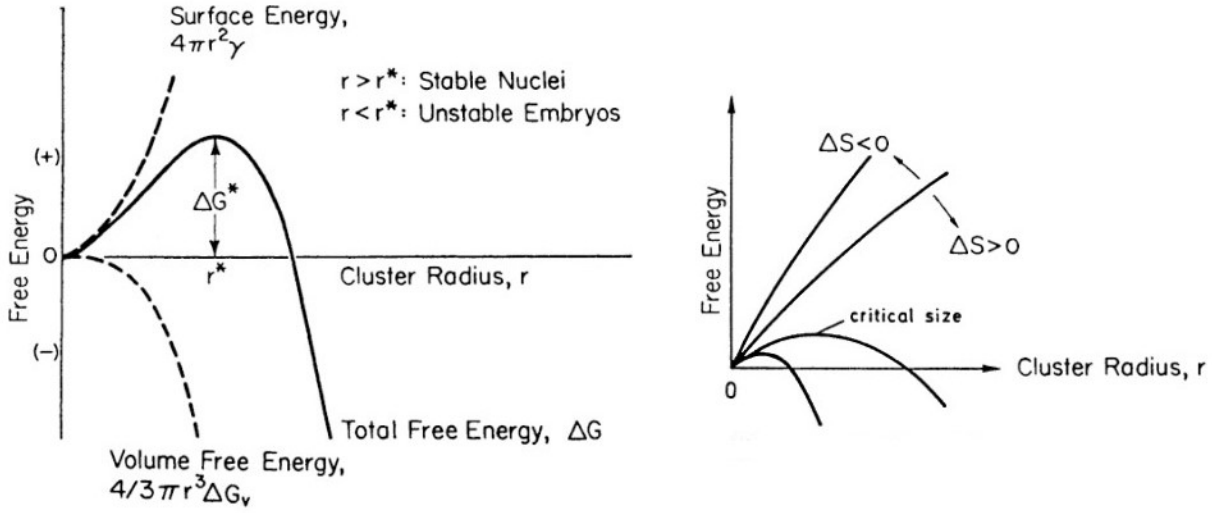

Figure 2.4: (Left) Qualitative plot of the free energy of a spherical cluster as a function of its radius derived from the capillary model. (Right) Qualitative plot of the same parameters, showing the dependence on the state of supersaturation. Adapted from [22] and [46], respectively.

Although more recent approaches distinguish the formation of 2D and 3D clusters and quantify this critical stable size by the number of atoms constituting the cluster, these are passably more complex, and although they provide more precise results, the same general trends can be obtained with a much simpler model [46], [50]. Considering perfectly spherical clusters with a uniform surface energy, the contact area between the film and substrate becomes vanishingly small: there is then no addition of an interfacial surface energy, Γ_{S-F}, no loss of substrate surface energy, Γ_{S-V}, and the contribution of the film's surface is reduced to an area given by the sphere's radius with surface energy per unit area Γ_{F-V}. As previously, considering variations of temperature at the interface to be relatively small, the free energy per volume can be expressed as a function of the change of pressure, which may be represented in terms of supersaturation. The derivative of the total free energy is then set to zero to find the maximum free energy, ΔG^*, shown in Figure 2.4 and, finally, r^*, the associated critical radius, is isolated, resulting in equation 16 [50].

$$r^* = 2\Omega\Gamma_{F-V}/k_B T_c \ln(S) \qquad 16)$$

where Ω is the volume of an adatom, and all other variables are as defined previously. Reiterating once again that this equation is merely a qualitative guide to cluster behavior, one can now look at

the effect of the main parameters. As shown in the right half of Figure 2.4, increasing supersaturation decreases the minimal cluster size and vice-versa: higher pressure in the vapor phase promotes cluster formation on the surface and limits desorption back into the saturated gas phase, whereas lower vapor pressure of the deposited film material indicates higher cohesion of the clusters, similarly limiting their desorption. As mentioned, the opposite is true for decreasing supersaturation.

Increasing the surface energy of the cluster will also require a larger radius: as the energy required to form the surface increases for a given energy per volume formed, one merely needs to lower the surface-to-volume ratio to compensate. With this in mind, it is worth noting that in this approximation of spherical clusters with no meaningful interface with the substrate, the surface energy of the film is all *added* to the system. The surface being a sphere is merely a convenience allowing to express the competing contributions with the same parameter, r^*. Considering a different geometry, the above equation would no longer hold, as different interfaces would have different energies, weighted by areas which may not be easily or elegantly expressed. The total change of surface energy can be understood to follow the following general form: $\Delta\Gamma = A_{F-V}\Gamma_{F-V} + A_{S-F}\Gamma_{S-F} - A_{S-F}\Gamma_{S-V}$, with A being the area associated to each type of newly formed surface. As such, even though it cannot be fit into a convenient equation, one can still intuitively grasp that higher substrate surface energies and stronger bonding between substrate and film are means to lower the size of stable clusters.

To inhibit losses due to discontinuities (causing plasmonic resonance), roughness or other morphological features, while maintaining low Ag thicknesses, it is of particular interest to consider not only how the shape and density of clusters can vary, but how they influence coalescence. One can see in Figure 2.5 the evolution of Ag layers in different conditions: starting with the nucleation of the first stable clusters, additional Ag adatoms tend diffuse along the surface to join existing clusters, rather than continually form new ones, which eventually leads to existing islands joining together into larger structures [50], [51]. As these form larger structures, they eventually connect at scales of the order of the substrate, enabling a certain conductivity. This state, as opposed to coalescence, where coverage nears and reaches totality, is referred to as percolation.

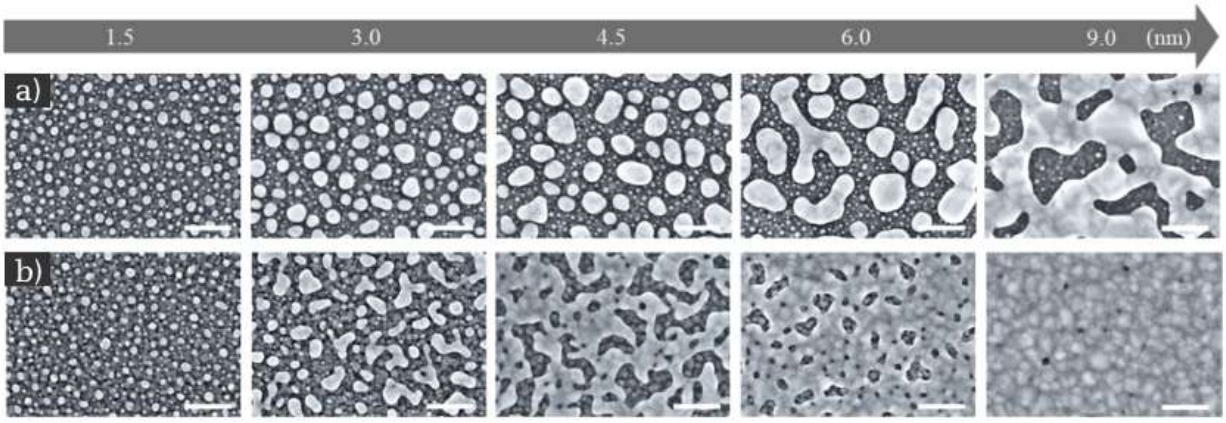

Figure 2.5: Planar FE-SEM images showing the morphological evolution of a) pure Ag and b) oxygen-doped Ag, deposited as a function of the nominal thickness. The scale bars represent 50 nm. Adapted from [51].

Smaller critical cluster sizes promote higher nucleation densities for a given coverage which is understood to act as a central precursor for later film structure, but this idea is challenged by Zhao *et al*., who have suggested that it is the coalescence dynamics which have greater importance on the overall growth of the layer [50], [51]. As shown in the lower half of Figure 2.5, oxygen-doped Ag (discussed in more detail in section 2.2.3) coalesces significantly faster than pure Ag despite a lower initial nucleation density, which is associated to a lower $Ag_{(O)}$ surface energy promoting flatter islands which join together at lower thicknesses [51]. As this behavior, just like increased nucleation density, can be promoted by decreasing the energy associated to forming a cluster, rather than take position on the importance of either factor, focus will be on their common origin and the kinetics which enable Ag films to reach, or not reach, their thermodynamically preferred states. To better address the latter, however, introducing a more practical view of deposition processes can be of use.

2.2.2 Controlling growth in physical vapor deposition processes

PVD can be defined as processes which create a coating by vaporizing a solid under vacuum, with minimal chemical interactions. This definition is a useful one, as it describes both deposition processes used in this work (detailed in section 3.1) and allows one to focus on the common atomistic mechanisms at play during deposition, subsequently allowing one to understand how to make use of these the controllable parameters to alter growth via kinetics, regardless of the chosen

deposition process. The main parameters which users can control to tailor film characteristics, as broken down by Greene, are choice of film material, incident flux and kinetic energy of impinging atoms of said material, temperature of the surface, as well as material choice, cleanliness, crystallinity and orientation of the substrate, and, finally, the flux of contaminants [6].

A few of these parameters fit squarely into the previous discussion. Of course, the film material and substrate material will directly determine the surface energies presented in equations 13 and 14. The orientation of the substrate will also change its surface energy, as mentioned when discussing the Wulff relation, given that the density of bonds will change as well [48], [52]. Moreover, the nature of said bonds may have an effect if they present an affinity with the deposited material (which will be discussed further in the following section). Others, such as crystallinity and cleanliness of the substrate, as well as flux of contaminants, require a bit more nuance.

Crystallinity of the substrate takes on more importance in epitaxy techniques where defects and lattice mismatch are critical parameters and may be more available to control [46], [53]. In this work, a polymer substrate is used, and although a thin overlayer is sufficient to change the effective surface and bonding energy, underlying structure has been shown to still affect silver morphology [54] and structure-zone models suggest that formation of highly of large grained dielectric layers at low thickness (particularly so at temperatures acceptable for polymers) is unlikely [53]. Thus, in the context of this work, it suffices to say that the substrate's crystallinity may serve as a template or promote similar morphology for layers deposited above it.

Contamination commonly lowers the free energy of affected surfaces: namely, substrate contamination by hydrocarbons is recognized to lower substrate energy and promote VW growth [55]. Moreover, as will be discussed in section 2.3, silver is fairly reactive, and the optical properties of a coating can be affected by a host of contaminants, such as residual water vapor. Contaminants impinging on the surface during deposition or present on an unclean surface may be treated rather similarly. One may glean from this quick discussion that controlled addition of certain materials can lower the surface energy of, say, silver, and promote FM growth. If voluntary and controlled, one can refer to these as surface treatments or doping: the term contamination can then be reserved for unwanted and uncontrolled additions, which will be treated straightforwardly as a source of error to minimise.

The flux of impinging film material, J, must be well distinguished from the deposition and adsorption rates – it is not a measure of how many adatoms are being added to the surface, but rather the potential amount that *could* be added, assuming they remain on the substrate [22]. Considering an ideal gas, partial pressure is directly related to the density of atoms in the vapor phase. Assuming said density to be approximately constant near the substrate, one intuitively understands that it will scale with J, and as such one can relate J with the partial pressure of film material in the vapor phase, P, introduced in the previous section. Before discussing the effects of J on film growth at length, a few more variables ought to be introduced: much like P gains meaning as part of S, J gains additional meaning as part of a larger kinetic picture.

Fortunately, the substrate temperature, T_S offers much of the rest of that picture; one can assume that impinging film material will be quickly thermalized by the substrate. As such, T_S will determine the film temperature, which the equilibrium vapor pressure, P_0, scales exponentially with. The temperature T_c which compression from the gas to the solid phase was approximated to occur at, used in equations 15 and 16, can also be taken as T_S, with the assumption that vapor near the interface is already partially thermalized. Of course, depending on the temperature discrepancy and the speed of thermalization, the approximation $T_c \approx T_S$ may be more or less valid [46], [56].

Even though P and P_0 do not linearly scale with J and T_S, increasing J will come with an increase of P, and increasing T_S will come with an increase of P_0. Thus, these parameters offer an effective means to increase or decrease the supersaturation $S = P/P_0$, and thus critical cluster size and nucleation density.

The role of these parameters goes beyond simply fitting into the previous thermodynamic theory. One will recall that when VW and FM modes were introduced it was said that adatoms would settle in the most advantageous positions, granted that they have enough energy to diffuse to low-energy sites. Here is where the kinetic energy of impinging species, E_K, left out of the thermodynamic developments, comes in and the temperature of the substrate, T_S, gains its kinetic aspect. Both supply energy to adatoms to diffuse along or desorb from the surface, albeit at different points in time; as mentioned previously, species reaching the surface are quickly thermalized, which can either supply low energy impinging species with energy or, inversely, dissipate energy from more

energetic ones [22]. The diffusivity or diffusion coefficient, D, of a thermalized adatom is given by equation [57].

$$D = D_0 e^{-(E_D/k_B T_S)} \quad 17)$$

where D_0 is a prefactor which includes the average number of adatom jumps, their length and the frequency at which jumps are attempted and can be approximated to 10^{-3} cm^2/s [57]. The activation barrier to diffusion, E_D, acts as a measure of the energy required to achieve diffusion, which can be approximated as about one tenth of the adatom binding energy [46]. T_S, in the approximation where the adatom is well thermalized to the substrate, corresponds to the adatom's effective temperature, supplying energy to overcome the activation barrier, with k_B naturally being Boltzmann's constant. Desorption from the substrate behaves similarly, although it is generally the desorption frequency which is considered, as there is no meaningful parallel to the diffusion length in this case; regardless, both have the same form defined by an activation barrier opposed to the thermal energy, albeit desorption requires a higher loss of coordination and thus of course a faces a higher potential energy barrier [46].

Naturally, the effect of particles impinging with high kinetic energy is qualitatively different than the effect of particles thermalized, even to high temperatures, upon reaching the substrate. Even a substrate heated up to 1000 K will only yield an effective energy ($k_B T_S$) of the order of 0.1 eV, which is approximately the kinetic energy of an impinging particle produced by evaporation. In stark contrast, those produced by biased magnetron sputtering or evaporation with ion beam assistance (IBA) can easily reach a few hundred eV, essentially ensuring diffusion and enabling re-sputtering [22], [58], [59]. Moreover, particles impinging with, or excited to, high kinetic energy will only retain said energy for a few vibrational periods, whereas thermalized adatoms will attempt jumps at a frequency of the order of 10^{12} Hz [22], [58]. Although high energy impinging species can be implanted or cause sub-surface effects, their effect beyond the surface is generally limited when compared to an increase in temperature, which will affect the bulk of the film, similarly to an annealing process [60].

There is no simple, single way to describe the interplay of all the aspects relevant to kinetic development of a film, particularly at low thicknesses pre-coalescence where FM and VW growth

modes lead to markedly different morphologies. The revised structure zone model (SZM) proposed by A. Anders, shown in Figure 2.6, does however highlight some interesting general ideas: it describes the dependence of the microstructure on a generalized temperature, T^*, which includes the film growth temperature normalized by the melting temperature of the film material (thus expressing temperature in terms of its ability to reorganize the material), and the contribution of heating and rearrangement of atoms due to the kinetic energy of impinging atoms. The energy axis typically found in SZM models is replaced with a normalized energy flux, E^*, which accounts for the energy of impinging species and their flux relative to that of deposited film material [59]. It should be noted that this SZM is specifically adapted to energetic deposition processes, hence the inaccessible region at low energy (another inaccessible region is present due to high energy flux causing heating) [59].

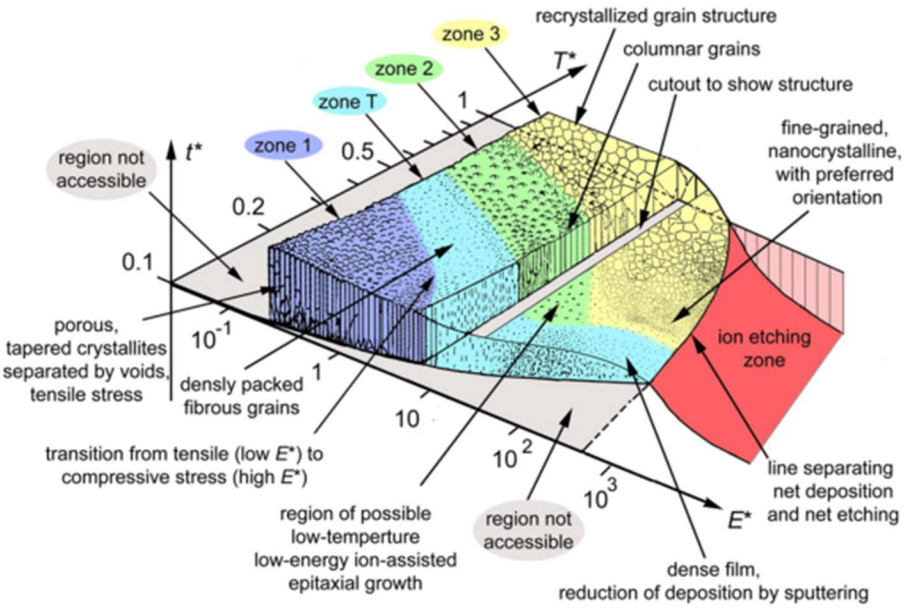

Figure 2.6: Structure zone diagram adapted to energetic deposition. The axes use generalized temperature T^* and normalized energy flux E^*, described in the text. Axis values and zone separations are purely illustrative. Reproduced from [59].

As such, with increasing generalized temperature, the formation of porous, small-grained films where there is insufficient mobility for preferred structures to form, shifts to larger grains with better packing density at higher temperatures [59]. Although high temperatures promote formation

of larger grain structures, which would otherwise be profitable, the reduced supersaturation and additional mobility promote diffusion of Ag adatoms, and even that of small clusters, to pre-existing islands, which is thermodynamically advantageous, as shown in Figure 2.4: this tendency to agglomerate into larger, less numerous islands is known as ripening or coarsening, and is exemplified in the upper half of Figure 2.5 [61]. Although deposition rate is not discussed here, which isn't unreasonable as higher temperatures can rearrange the bulk of the film, higher deposition rates (and understandably, supersaturation) promote higher nucleation density and faster coalescence, as well as lower packing density for a given temperature, illustrating a balance to be maintained between the two parameters [62], [63].

A similar balance must be considered for the kinetic energy flux. Anders' SZM shows that for fully formed well coalesced films, with increasing energy flux, one initially promotes earlier transition to larger-grained structures, then transition to equally dense, yet fine and well-aligned grains, as larger grains are more likely to be re-sputtered. Finally, net etching occurs when re-sputtering overcomes the deposition process [59], [60]. A more delicate balance is present for very thin films, particularly in VW growth mode, as the enhanced diffusion length can promote a form of ripening where adatoms will be able to join existing clusters further away, and are likely to be re-sputtered or diffuse away otherwise, creating depleted zones around larger clusters, as reported by Marinov [64]. On the other hand, judicious use of kinetic assistance can promote higher nucleation density and FM type growth; Ensinger recommends pulsed ion bombardment to this end, whereas Netterfield and Martin report varying improvements of coalescence depending on specific ion energy and flux values (relative to J) [60], [65].

As such, although there is no single straightforward single way to use kinetic parameters to achieve high quality and rapid coalescence of thin films, such as Ag, growing in VW mode. As mentioned previously, however, kinetics alter the ability of a system to reach its thermodynamically preferred state; therefore the approach used to tailor the growth of these films will center around means to alter said state and a judicious use of kinetics to properly enable the desired features.

2.2.3 Growth modification techniques

Practical means of controlling the growth of thin silver films may now be exposed. One will recall that in the context of this work, a thin, continuous silver film is required to mitigate absorption, preferably with few grain boundaries and low roughness.

Of course, the simplest solution to promote continuous layer formation at low thickness is to promote FM growth, which, without even beginning to consider deposition conditions, can be promoted by using a high surface energy substrate with as strong as possible binding affinity to the silver film, as shown in equation 14. Thin films deposited to assist the growth of silver in this way, by effectively acting as an improved substrate are commonly referred to as *seed layers*.

The seed layer of choice used by industry is zinc oxide (ZnO), which is known to improve the structure – and thus the electronic and optical properties – of the silver layer, as well as having high surface energy, making it ideal for the deposition of transparent silver layers [23], [66]. Cornil *et* al. use density functional theory (DFT) simulations to compare the adhesion energy of Ag (111) on commonly used transparent oxides [67]. Amongst these, the high adherence of zirconia (ZrO_2) and zinc oxide stand out: in particular, their polar surfaces, present for ZnO $(000\bar{1})$ and ZrO_2 (100) orientations, are terminated with oxygen and thus allows metal-oxide bonding rather than metal-metal bonding [67].This is consistent with the results of Li *et al*., who report improved percolation of Ag deposited on aluminum-doped ZnO (AZO) by applying a reactive oxygen plasma treatment to the substrate before deposition of the Ag layer [68]. The mechanism suggested in their work, a reduction of adatom mobility forcing Ag to group into smaller clusters, is consistent with previous discussions in this work, if one assumes that the oxygen plasma treatment increases the density of oxygen bonds at the AZO surface; this should also reduce the interfacial surface energy, which of course is not contradictory.

Cubic zirconia, as used in the previously mentioned simulations, can relax into a monoclinic structure, with much lower surface energies [69]. Moreover, the non-polar orientation of ZrO_2 studied shows very weak adhesion, whereas the other orientation of ZnO tested remains competitive relative to the other oxides [67]. Given that ZrO_2 is already commonly used in ophthalmic anti-reflective coatings, it remains interesting to consider its application alongside silver, however [5]. Titanium dioxide (TiO_2) and zinc-tin oxide have also been shown to be good

seed layers [70]. Despite poor adhesion to Ag (which may be remedied by doping or leaving the surface sub-stoichiometric), TiO_2 (110) shows very little mismatch with Ag (111), which is a key factor in improving Ag film crystallinity, and thus quality, according to Ries, who suggests that using strain induced by ion bombardment or doping to reduce the mismatch between ZnO and Ag is a key manner of improving ZnO as a seed layer [23], [67].

Although there is understandably a focus on transparent, dielectric seed layers for use in applications such as this work, where transparency of the coating is required, it can be of some interest to couple these with very thin metallic layers to further promote rapid coalescence of the Ag layer. As has been repeated, the tendency of Ag films to form in a VW growth mode is due to its high surface energy and low affinity with common substrates. This offers a certain niche for certain less noble metals, which bind more strongly, and thus grow in FM mode while retaining high surface energy [71]. Anders *et al*. tested sub-nanometer layers of niobium (Nb) and titanium (Ti) as metal seeds and found an extremely important dependence on the (nominal) thickness of the layer [72]. In this small, sub-nanometer range, faster coalescence and smoother films with significantly smaller grain sizes are obtained. Following the work of Campbell, they suggest that, depending on substrate temperature (and thus on adatom mobility) and the level of coverage, FM growth may be replaced by VW growth, in which case the preferential adsorption to the metal seed layer would promote VW growth for the Ag layer as well, diminishing the quality of the metal seed [71], [72]. Thus, a careful selection of deposition conditions and nominal thickness is required, as exemplified in Figure 2.7.

The reported mass-equivalent thickness ranges where given metallic seeds are effective should be taken with a grain of salt, as these will hinge on multiple parameters, such as oxidation of the metal seeds, sputtering power, or substrate parameters, and as such will not be readily replicable. However, the general behavior of Ag films deposited on different metal-dielectric seed layers is of great interest: particularly so, nickel (Ni) and chromium (Cr), alloys of which are commonly used in thin layers both below and above the silver layer to enhance its durability, detailed at length in the following section. Fukuda *et al*. report that Ni layers deposited on AZO substrates will improve coalescence for nominal thicknesses of a couple tenths of a nanometer, but remain similarly sensitive, with layers of higher equivalent thickness seemingly inhibiting percolation, shown on the right of Figure 2.7. Cr, on the other hand, was reported to delay percolation for all thickness

tested, shown on the right of Figure 2.7 [73]. There is no data for the effect of these metal seeds on grain size and roughness in that work, although Sonmez *et al.*, focused on metal seeds with nominal thicknesses of a nanometer and above, report that Ag films deposited on said "thick" Ni and Cr films display lower sheet resistance and roughness than those directly deposited on AZO. That being said, Ni seed layers are still shown to promote smoother films than Cr, if not as smooth as Nb, illustrating that the general trends observed over multiple reports serve as a good indicator of a metal film's usefulness as a seed layer [74].

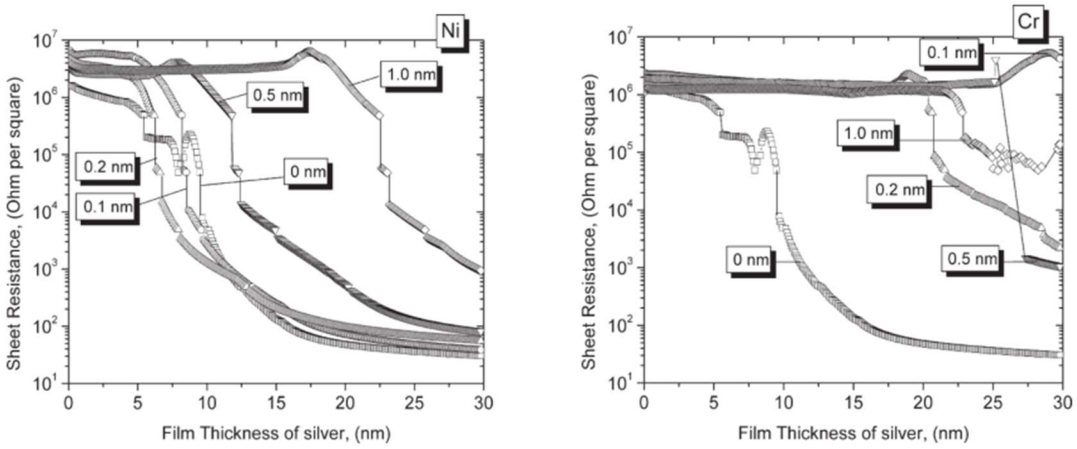

Figure 2.7: *In situ* sheet resistance of a Ag film as a function of its nominal thickness, deposited on AZO coated substrates with Ni (left) and Cr (right) metallic seed layers of various thicknesses. Adapted from [73].

Another candidate of interest as a metal seed layer is germanium (Ge), which has been shown to promote the formation of extremely smooth Ag layers, with small grain sizes [75], [76]. Unfortunately, Ge diffusion to grain boundaries and other free surfaces has been tied to an important increase in silver resistivity; alternatively, Ni seeds can provide a similar, if not equivalent reduction of roughness, while promoting larger Ag grains and lower resistivity, making them more interesting for surface plasmon or low-E glass applications [42], [77]. This decrease in opto-electronic quality may be worth the smooth layer formation and the potential durability improvement for situations where IR optical properties are not a central objective; for example, Fujifilm has patented an AR coating for camera lenses making use of Ag grown on germanium which displays very little reflection in the visible spectrum [78].

Alternatively, one can alter the Ag layer rather than the substrate. A lack of mobility can trap adatoms in non-equilibrium states: for seed layer metals, which would preferably be deposited in FM growth mode, a lack of mobility could promote cluster formation – but for the silver layer, which will tend to grow in VW mode, and may be further affected by ripening effects, low mobility can trap silver in small, uniform clusters to promote growth. One will recall that this was the mechanism proposed by Li *et al*. for AZO seed layers enhanced by oxygen plasma treatment; following the same concept one can oxidise silver nano clusters in their early germination stages to lock in their morphology [79], [80].

From there, one can either use this silver oxide as a metallic seed layer or use this as a template for the growth of the whole layer, using oxygen as a dopant. In one method, proposed by Liu *et al.*, silver is deposited in distinct steps, with the downtime between each deposition being used to oxidise the surfaces of the small silver clusters formed, and in doing so aims to produce a film which is entirely composed of small grains with oxidised boundaries inhibiting diffusion [80]. Although seemingly less transparent than the silver layers grown on an oxidized silver seed layer by Zhao *et al.*, the former were deposited directly on glass, whereas the latter were deposited on and capped with ZnO; this is particularly important as the change in interference effects can greatly affect the transmission – without the optical constants of each layer or at least their reflectance curves, one cannot distinguish the effect of the Ag layer's quality from that of an improved architecture [79], [80]. Moreover, the increase in binding and reduction in surface energy are expected promote flatter initial clusters, roughly described by equation 13, and also ought to promote smaller clusters and higher cluster densities as discussed following equation 16. To what extent mobility affects the growth as opposed to the reduced surface energy remains debatable [51].

Although not exactly equivalent to the sequenced deposition-oxidation method, sputtering of Ag in a mixed Ar-O_2 gas environment has been performed on ZnO; the $Ag_{(O)}$ films so produced displayed low roughness, earlier coalescence, and high transparency comparable to the Ag films grown on an $Ag_{(O)}$ metal seed layer [79], [81]. These films show an increase in n and a decrease in k with increasing oxygen content: although this decreases the k/n figure of merit for silver layers, at low concentrations ($\approx$ 3.4 at.%) this decrease is relatively small while the improvement to coalescence remains important [81]. Whether the oxygen content of these films being added continuously rather than sequentially has an important effect on the $Ag_{(O)}$ layer's properties is

unclear; one could consider semi-randomly distributed $Ag_{(O)}$ defects in an otherwise normal film, as opposed to $Ag_{(O)}$ formation specifically at grain boundaries, a difference which might influence the durability or optical properties of the film.

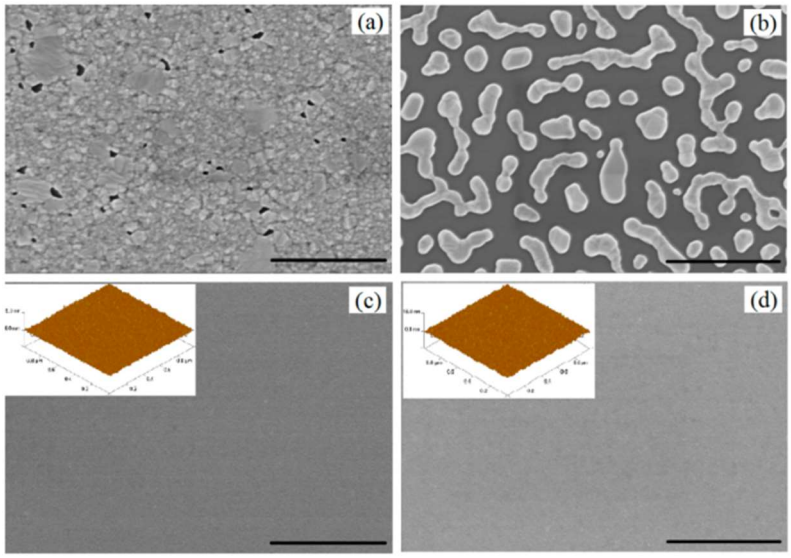

Figure 2.8: SEM imaging (scale bars are 1 μm) of 15 nm Ag (top) and $Ag_{(Al)}$ (bottom) films as-deposited (left) and annealed at 300 °C (right). Insets for the $Ag_{(Al)}$ films show AFM measurements with root-mean-square roughness of 0.43 and 0.45 nm for the as-deposited and annealed film, respectively. Reproduced from [82].

There are a multitude of other dopants which have been reported to either improve the coalescence or durability of Ag films, such as chromium, gold, silicon and zinc, amongst others [83]–[85]. It would be well beyond the scope of this work to investigate each of these. As such, focus will be given to a single metal dopant, that is aluminum (Al). Relatively small quantities of Al co-deposited with Ag significantly change the film morphology throughout the growth process, promoting earlier coalescence and significantly smoother final films, with roughness values easily an order of magnitude lower than those of pure Ag films of equal thickness [82], [86], [87]. The mechanism offered by Gu *et al*. explaining this altered growth process lines up particularly well with previous discussions on metallic seed layers and oxygen doping; as Al is far less noble than Ag, it will bind more strongly with the substrate, particularly so if it presents an opportunity to bond with oxygen - as such, the energy barrier for diffusion is increased, and surface mobility is reduced, as was the case for oxidized Ag [82]. Moreover, this higher affinity, coupled to surface energy approximately

equal to that of Ag [52], will lead to flatter initial clusters of Al which will then promote Ag growth as a metallic seed layer would.

Once again, resolving to what extent the bonds are affecting mobility at the interface or are changing the free energy of island formation remains too complex to ascertain, as bonding energy also changes mobility, and both contributions are considered. Naturally, smaller average grain sizes are found for these films, as is the case for the two previous cases, oxygen doping and metal seed layers, which Al doping has been likened to. Unlike the sequenced deposition-oxidation process elaborated upon previously, Gu *et al*. do not propose a particular mechanism as to *how* the addition of Al limits coarsening, but as grain sizes and morphology show little variation during growth and annealing at temperatures up to 500 °C (if only for a short annealing time), there is definitely a major reduction in Ag mass transport, as exemplified in Figure 2.8 [82], [86]. Weaver and Brown reported that separate layers of Ag and Al demonstrate a short-range and short-lived inter-diffusion of Ag and Al - even if not forming an intermetallic compound, this may still create a barrier to additional diffusion, which may be an appropriate explanation to both the short duration of this diffusion and the behavior of Al-doped Ag films [88].

In keeping with the idea of comparing Al-doped Ag, or $Ag_{(Al)}$, to $Ag_{(O)}$, it is of interest to compare their electric and optical properties, as both dopants bring very similar improvements to the film morphology. Unfortunately, studies of $Ag_{(Al)}$ describe optical constants using measurements of the dielectric function, making comparison to the refractive indices reported for $Ag_{(O)}$ somewhat clumsy. Zhang *et al*. report an increase in both ε_1 and ε_2, which reflects a drop in conductivity and an increase in losses and is equivalent to a decrease of the Ag layer's k/n ratio [86]. Liu *et al*. compare the sheet resistance of their $Ag_{(O)}$ films deposited on glass to that of the $Ag_{(Al)}$ deposited onto fused silica by Zhang, which again shows very comparable performance: there is no obvious advantage to either one, without additional context [80], [87]. Both dopants have been shown to allow highly transparent designs when reflection is properly attenuated, and as such the hardware required to implement their use or their effect on Ag durability may be a defining point in the selection of either dopant [81], [86].

Both of these dopants have the common issue that they diminish the quality of the silver layer, insofar as optical properties are concerned. Ag was chosen for this work for the simple reason that

it displays the best optical properties for the application considered, and it is therefore intuitive that the introduction of another, less desirable material would be detrimental to the optical properties, even if useful in controlling the film growth or durability. Ideally, a perfect dopant would alter the growth mode, but not permanently alter the nature of the film. Nitrogen (N) has been shown to be such a dopant. Coalescence at thicknesses as low as 5 nm, accompanied by the formation of significantly flatter (111) oriented islands suggests that it has a strong effect on the surface energy and thus coalescence behavior, (which one will recall was found to be a key indicator of the usefulness of a dopant and its effect on the system's surface energy). X-ray photoelectron spectroscopy (XPS) measurements indicate low concentrations of N remaining within the films, with very little bonding to Ag, suggesting that the small amount of residual N is mostly in the form of N_2 molecules trapped in vacancies within the film [89]. Yun *et al*. have used DFT simulations to determine the cause of this behavior, revealing that the energy required for the formation of a N atom within the Ag lattice not only changes with the site, but the crystal orientation and the distance from the Ag surface as well. More specifically, there is a negative formation energy for N at the surface of (111) and (100) Ag facets, however this changes dramatically only a few nm into the bulk, as shown in figure the left half of Figure 2.9 rendering $Ag_{(N)}$ within the bulk unstable and inciting N float-out to the surface [90].

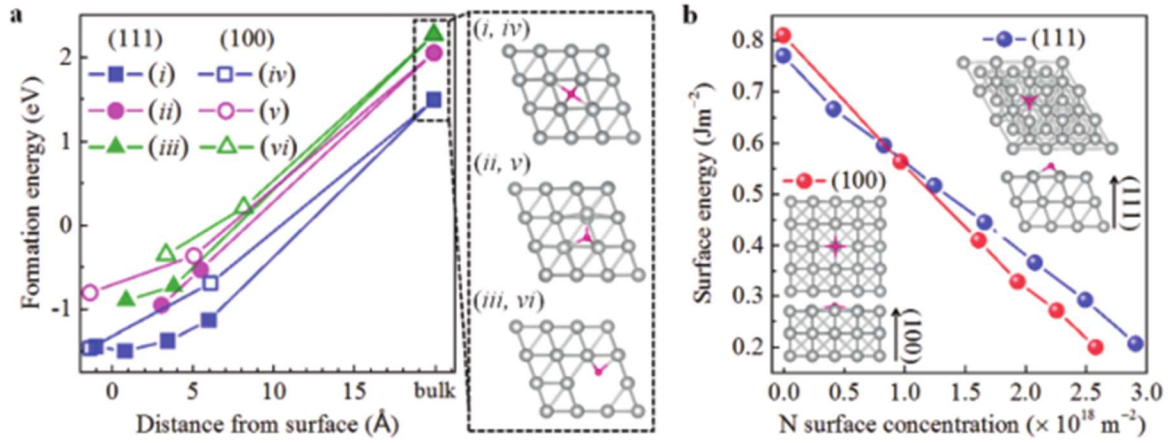

Figure 2.9: Numerical simulations showing the change in formation energy for N atom occupation at different sites, for different crystal orientations, as a function of distance from the Ag surface (right, a), and the change in surface energy for (111) and (100) Ag surface orientations as a function of N-occupied site density (left, b). Reproduced from [90].

Hu *et al*. offer the alternative explanation that substituting argon (Ar) with N_2 as the sputtering gas decreases the kinetic energy of impinging adatoms with low mobility inhibiting the formation of well ordered volumes, based on the observation that with increasing N_2 content, their films show increasing preference (100) surface orientation, smaller grain sizes, and even present holes within the film at sufficient concentrations [91]. Albeit the mechanism suggested seems far-fetched, their observations are of interest, and coherent with the other articles reviewed so far. A decrease in surface energy ought to reduce the critical cluster formation size, and thus increase nucleation density, which should in turn promote smaller grain size. Moreover, the simulations by Yun *et al*. show that the reduction in surface energy with the addition of N is dependant on both the orientation of, and the density of N atoms at, the surface. More specifically, although both (111) and (100) both show an approximatively linear decrease in surface energy with N density at the surface, past $\approx 10^{18}$ N atoms/m^2, (100) oriented surfaces have a lower surface energy [90]. Therefore, with increasing thickness, outgassed N adds itself to impinging N atoms, increasing the concentration, and shifting the preferred orientation with increasing thickness, hence the pronounced (100) orientation reported by Hu *et al*., which were studying films microns thick [90], [91]. This increase in N density with increasing thickness is also coherent with the appearance of holes within thicker films as well as the initial observations suggesting residual N_2 is trapped in vacancies; this all points to the idea that, if highly promising as a means to alter Ag growth without deteriorating its optical properties, N doping is susceptible to over-use, and must be employed accordingly.

Most of the techniques proposed as of yet improve coalescence and smoothness but promote smaller grain sizes. This is an unfortunate consequence of the thermodynamics of the system; if sufficient thermal energy is supplied to adatoms to reorganize into larger grains, the film will experience coarsening, and although the methods proposed so far should promote a flatter equilibrium surface, the flatness of certain clusters can also be associated in part to lateral growth promoted by adatom diffusion to existing clusters, which without sufficient energy to reorganize, maintain a kinetically influenced morphology [50]. It suffices to say that these methods may simply not be sufficient to ensure coalescence at low thicknesses while promoting larger grains. An alternative approach to achieve thin, continuous, large grained films is to not attempt to make them coalesce quickly, but rather to make a coalesced film thinner. As mentioned, for a given volume, a crystal's equilibrium structure should be one that minimizes the total surface energy, and thus

minimizes the surface to volume ratio – and just as this leads to adatoms stubbornly clinging together as clusters during coalescence, a continuous film should be similarly driven to remain continuous, lest it form new surfaces [49].

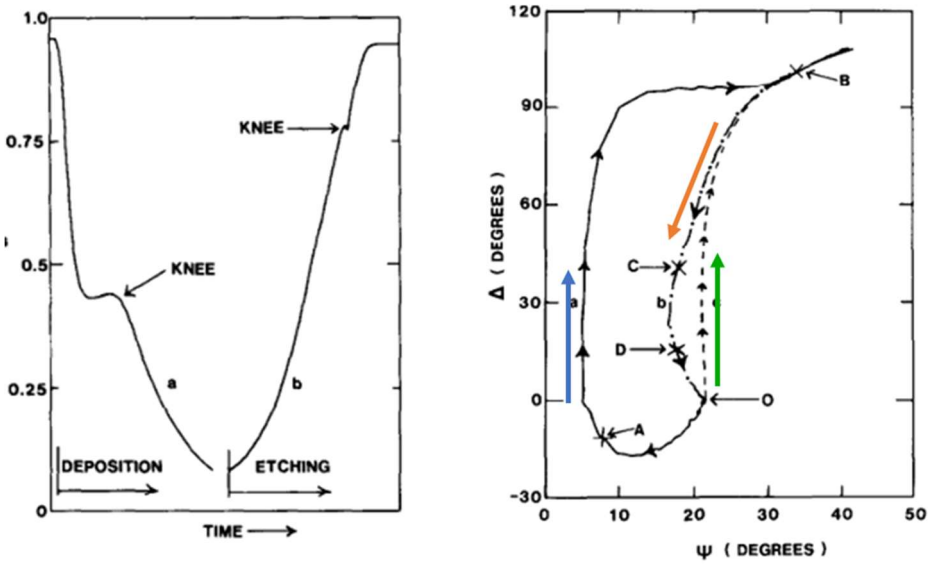

Figure 2.10: *In situ* transmission photometry as a function of time (left) and ellipsometry (right) performed at 633 nm during deposition and etching of gold films. "Knee" features are associated to film coalescence by the author. Blue, orange and green arrows correspond to ellipsometric data for deposition, etching (obtained during deposition) and modeled deposition of a continuous gold film, respectively. Adapted from [65].

Netterfield and Martin monitored the evaporation of gold films and their subsequent etching by an ion beam with *in situ* spectrophotometry and ellipsometry. Without delving into the precision of the models used to obtain quantitative results, qualitative features in both measurements (see Figure 2.10) show distinctly different behaviours during deposition and etching, indicating that continuity of the film is retained below the coalescence thicknesses found during deposition [65]. From their results, they suggest that smoothness at the interfaces, namely at the base of the layer, where the coalescence of islands with high contact angles could leave voids, would be an important factor in the re-separation of the film: they assume uniform etching of the surface, which would lead to voids at the base of the film connecting with grooves at the surface, breaking up the film at a lower thickness, as shown in Figure 2.11 [65]. One could suggest that heating due to exposure to the ion beam could enable the film to revert to islands at a low enough surface to volume ratio, however

the explanation offered by Netterfield and Martin is consistent with transmission electron microscopy (TEM) measurements performed by Hodgkinson and Lemmon, who report that more or less spherical clusters are etched almost uniformly, elongated clusters seem to break back into smaller, rounder islands before being completely removed, and continuous films begin by presenting holes which eventually expand and meet, dividing the film into islands which are then eroded following the previous behaviors [92]. Etching of tungsten films by Puik *et al*. shows an initial decrease in film roughness, followed by marked stabilization, which the authors associate to the removal of atoms at cluster edges or which are simply part of smaller clusters, both of which have lower coordination and would be sputtered more easily: beyond this, competing effects are expected lead to an approximatively constant roughness which seems consistent with previous observations [93]. Although the mechanism of film re-separation is not beyond doubt, with additional investigation this growth hysteresis behavior could potentially be made into a useful tool for controlling film morphology.

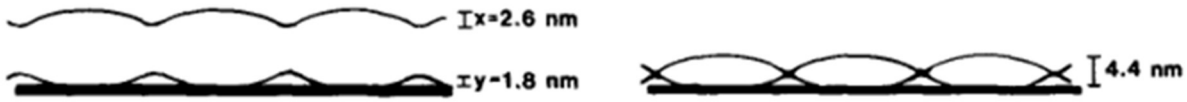

Figure 2.11: Idealized representation of gold films just after coalescence (left) and just before becoming discontinuous (right), showing the importance smooth interfaces under the assumption of uniform etching. Adapted from [65].

2.3 The durability of silver films

There remains one principal concern to address in regard to the application of thin silver films: their durability. Common actors amongst the different degradation mechanisms and methods employed to inhibit them make that a categorical separation can be somewhat complex: as such, in the interest of brevity, degradation mechanisms will be loosely separated and presented together. Following this, specific techniques used to enhance silver durability will be presented

2.3.1 Degradation mechanisms

It has already been mentioned that Ag presents poor adhesion on most dielectrics, although this primarily focused on the bond strength of Ag with these layers for the purpose of determining the growth mode. The adhesion is not only important for growth dynamics, however: it is indispensable to the mechanical integrity of the coating, which is a concern in its own right, and it has been shown to play an important role in the overall durability of silver mirrors [94]. That being said, the upper layer may adhere better to the Ag film than the Ag to the layer beneath it, even if the materials are identical, due to the different resulting growth modes [95]. This may place additional burden on the seed layer in this project, as, in mirror applications, the seed layer's optical properties are unimportant, allowing to straightforwardly select a base layer which best promotes adhesion. It should go without saying that he ductile nature of silver, if useful in the context of this project, makes it particularly vulnerable to abrasion, making a top protective dielectric layer essential for mechanically durable coatings, regardless of the needs of interferential stack design [96]. Strain in dielectric layers has not been clearly determined to be an issue for silver mirrors although Phillips *et al*. have reported mirror coatings with more stressed dielectric layers were less durable in environmental testing, which they suggested to be due to relaxation of the film caused by the high humidity associated with their testing [97]. This is consistent with previous work by Tadokoro *et al*., where cycled changes in humidity induced shrinkage, cracking, and relaxation of dielectric AR layers, an effect which Hirsch explains to be caused by electrostatic interaction of the water molecules accumulated in film pores, particularly those within an approximate radius range of 10 – 100 Å [98], [99].

Although the cracking of the dielectric layers doesn't affect the Ag layer per se, their integrity is necessary to their use in the coating as a whole, and as mentioned, they must be included within the coating to protect the ductile Ag film. This need for a non-porous, well adhered dielectric layer is a fortuitous one, as it is equally tied to the chemical and environmental durability of coatings. Although quite noble, Ag is susceptible to degradation when reacting with sulfur, chlorine, or oxygen, namely [25], [94]. In this work, focus will be mainly on chlorine (Cl), in the interest of maintaining a coherent comparison to the durability of other ophthalmic lenses [12]. Although Ag is more susceptible to sulfur, Folgner reports that in Cl_2 and mixed flowing gas tests, corrosion

behavior is similar, and Boccas *et al*. find that the same methods are effective in combatting degradation by either element [94], [96].

The corrosion of metals is typically viewed through the lens of electrochemistry, and although this work will address or complement the description of certain behaviors by this means, it will also use a more atomistic approach. Koike *et al*. have used DFT simulations to model the behavior of Ag thin films exposed to Cl, finding that, beyond the formation of soluble compounds such as $AgCl_2$, there is an aggregation behavior in which a single Cl atom can induce the formation of solid clusters of Ag_7Cl [84]. This is coherent both with the low amounts of corrosion products detected at corrosion sites studied by Folgner, and their morphologies in which Ag aggregates can be found surrounded by an area depleted of Ag, depending on different adhesion layers, as shown in Figure 2.12 [94]. Its suggested that Ag diffusion plays an important part in the degradation process, with the different morphologies being linked to diffusion perpendicular or parallel to the interface [94].

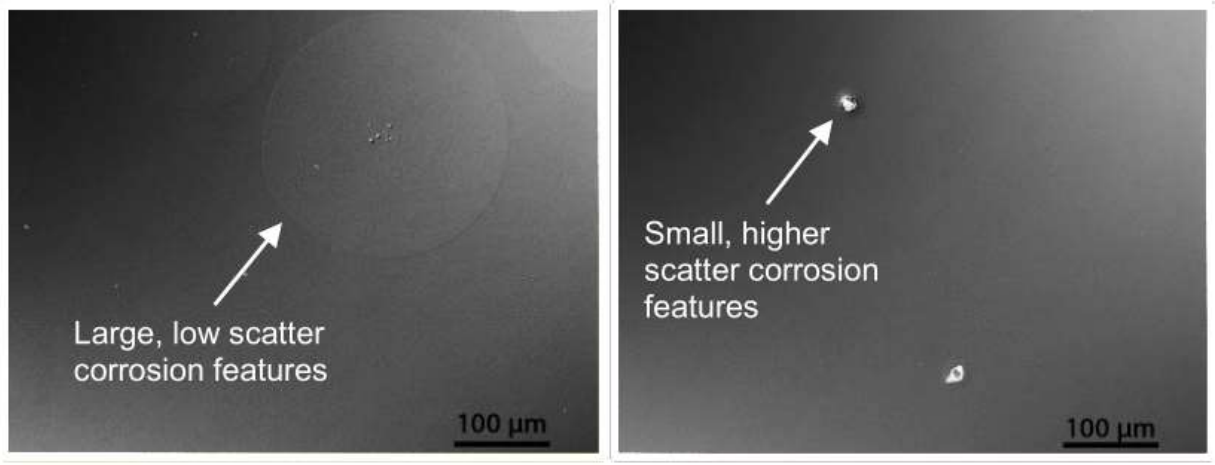

Figure 2.12: Optical micrographs of corrosion features after 10 days of mixed flowing gas exposure on a Ag mirror using a CrN_x adhesion layer (left), and a $NiCrN_x$ adhesion layer (right). Adapted from [94].

The diffusion of atoms within a material can be described by Kirkendall diffusion, which refers to diffusion mediated by the exchange of adatoms and vacancies, rather than a process of atoms exchanging sites as had been suggested previously [100]. Degradation at an interface, such as formation of an oxide or the Ag_7Cl clusters mentioned previously, can create vacancies which atoms diffuse to: one understands that the atoms which diffused to the degradation site leave

vacancies in their wake, enabling new atoms to take their place, once again adjacent to the degradation site, which can allow localized degradation to draw in additional material and depleting the surrounding area [100], [101].

In practical situations, it should come as no surprise that diffusion along grain boundaries generally occurs first, as these offer open channels for diffusion, whereas the exchange of an atom and vacancy happens under higher coordination; diffusion within the lattice only becomes comparable to diffusion at the grain boundaries for temperatures nearing half the melting point [53]. Depending on the size of the grain boundaries as opposed to the reactant, they may also allow diffusion of corrosive species to other parts of the coating, consistent with observations of passivation layers formed at grain boundaries and voids for different materials [86], [102], [103]. It has been reported that grain boundaries and their own grains can engage in galvanic coupling (where the less noble of two metals in electrical contact supplies electrons to neutralize ions of the nobler metal, and in doing so creates metal ions of its own, and is thus corroded first): how this would compare to the effect of grain boundary diffusion is unclear, but it is obvious that smaller grain size and thus additional grain boundaries contribute to Ag layer degradation [104].

Corrosion sites dominated by lateral diffusion have been associated to the adhesion of the protective layer to the Ag layer. The importance of a protective layer in itself is quite intuitive, as the simplest way to stop Ag from reacting with other chemicals is simply to isolate it from them; it follows that said protective layer should have minimal porosity and defects, as to limit diffusion of corrosive species and absorption of water, which can accelerate degradation [94], [104]. The relevance of their adhesion is less intuitive. Fuqua and Barrie suggest that an appropriate adhesion layer can promote the formation of a higher quality dielectric, which protects the coating; however, they also note that defects found on coatings without an adhesion layer coalesced on the sample of the surface, suggesting that corrosion products are spreading out, and that intentional scratches through the protective layer did not result in a significant decrease: this is consistent with Folgner's suggestion that poor adhesion at the interface allows diffusion along it, much like grain boundaries, which could both allow corrosive species to spread over the interface and allow Ag diffusion to corrosion sites [94], [105].

2.3.2 Enhancing silver durability

Practical means of enhancing the durability of thin silver films can now be discussed. Before considering them as part of a stack, one might consider the properties the metal layer on its own. Koike *et al*. propose two general types of alloying to inhibit cluster formation, and although their approach consists in using both simultaneously, they may be separated for the sake of simplicity.

The first method is to alloy Ag with a metal which does not react strongly with Cl and will disrupt the formation of clusters, namely gold and palladium. The second method is to alloy Ag with a metal which will react more strongly with Cl than it, such as copper or neodymium, capturing the Cl atom in a stable molecule where it cannot interact with Ag [84]. This is comparable to a sacrificial anode, in which a reactive metal is added so that galvanic coupling protects the nobler metal. Although an explicit link has not been made to galvanic coupling within the work of Koike *et al*., Song *et al*. report improved corrosion resistance by depositing a layer of copper *below* the Ag layer of a telescope mirror, suggesting that even contact with a more reactive metal is sufficient to slow corrosion [106]. Their observation of copper at the surface of the Ag layer is consistent with other observations in which protective layers or alloying materials segregate to the surface of coatings and/or their grain boundaries to form a passivation layer [86], [102], [107]. Al stands out amongst these, used both for the protection of copper and Ag films: that being said, the use of $Ag_{(Al)}$ has been proposed to render films without protective layers stable in atmosphere or at high temperatures, rather than in corrosion testing. Phillips *et al*. report that Ag is more durable with a copper underlayer rather than an aluminum one, which suggests, despite some durability improvements it may be better suited to promote early coalescence rather than inhibit degradation [108].

Regardless of the quality of metallic Al as part of an effective alloy, its oxide has shown itself to be a useful protective layer, drawing interest to the ability of $Ag_{(Al)}$ to form an alumina passivation layer at its surfaces and grain boundaries. Barrios *et al*. report that an alumina coating as thin as 2 nm greatly improves the chemical and mechanical wear resistance of Ag structures [109]. Moreover, it can be deposited by atomic layer deposition (ALD), a chemical vapor deposition process which allows to create extremely conformal films and can thus seal in pinholes or other defects. Phillips *et al*. report an increase in Ag durability obtained in stacks terminated with an

ALD-deposited Al_2O_3 coating, with the exception of a 280 nm thick, 5 layered coating, suggesting that ALD offers a significant advantage except when compared to the most elaborate protective coatings [97]. Their comparison of PVD deposited coatings seems to indicate that Al_2O_3 is amongst the best protective coatings for Ag, although a similar comparison by Schwinde *et al*. found them to be lacking in durability; this may be due to differences in process or testing conditions [97], [110]. Regardless, it shows promise as protective layer, particularly as an ALD coating or as a passivation layer in $Ag_{(Al)}$ films, which should equally display high conformality. However, the *de facto* protective layer of choice is generally considered to be silicon nitride (Si_3N_4) as it is both durable and can be deposited easily by sputtering, without concerning oneself about damaging the Ag layer with reactive plasma, and adheres well with nickel-chrome nitride, a highly performant protective layer discussed below [94], [110]–[113]. However, it is prone to tensile stress, which may cause cracking and failure, particularly in high humidity, as observed by Phillips *et al*. [97].

Last but not least, in order to promote high durability the Ag layer must be well adhered to the protective layer as well as to the seed layer; the latter may be under-represented in the cited literature, as much of it focuses on the durability of Ag mirrors, in which case the lower Ag interface is not optically important and can be adhered with metallic layers tens of nanometers thick. Such a design is quite clearly not an option in the case of this project. Hafezian *et al*. have reported on the diffusion of a thin Ag layer through a barrier layer of titanium, upon exposure to an oxygen plasma, as means of identifying the effect of the seed layer [101]. It is shown that seed layers with higher binding energies not only improve Ag coalescence, they limit Kirkendall diffusion, as tightly bound Ag clusters will remain immobile, diverting the chain reaction of Ag atoms diffusing into the vacancy left by the previous diffusion [101]. As such, using a ZnO seed layer to both enhance adhesion and promote Ag crystallinity is expected to assist the corrosion durability of thin Ag films, perhaps more so if the surface is treated with an oxygen plasma as suggested by Li *et al*. [23], [68], [101].

That being said, the use of such a seed layer may be supplemented, if not replaced by the use of a nickel-chrome nitride ($NiCrN_x$) adhesion layer. Initially suggested to simply improve the adhesion by virtue of presenting CrN_x as a nitride to adhere to Si_3N_4 dielectric coatings and Ni to adhere to Ag, recent work by Folgner suggests the possibility of another mechanism; as shown in Figure 2.13, XPS depth profiling shows diffusion of Ni into the Ag layer [94], [113]. This is not only an

enhancement of the adhesion: there appears to be a qualitative change in the diffusion of Ag when compared to a CrN_x adhesion layer, as shown in Figure 2.12, with Ni diffusion into the Ag layer limiting its ability to diffuse [94]. It follows that Ni diffusion being limited to near the surface, lateral diffusion is only limited near the surface as well. Then cluster formation must draw Ag in from the bulk of the layer, depleting the bulk rather than the interface, creating the different corrosion morphology observed in the right half of Figure 2.12. In the framework of Kirkendall diffusion, the diffusion of Ni into Ag would imply that Ni has a higher diffusivity than its counterpart [100]. From there things become more hypothetical: perhaps Ni then diffuses to vacancies formed during cluster formation, the absence of vacancies around the corrosion site limiting Ag interaction, or perhaps it disrupts cluster formation similarly to the suggestion of Koike *et al.* [84].

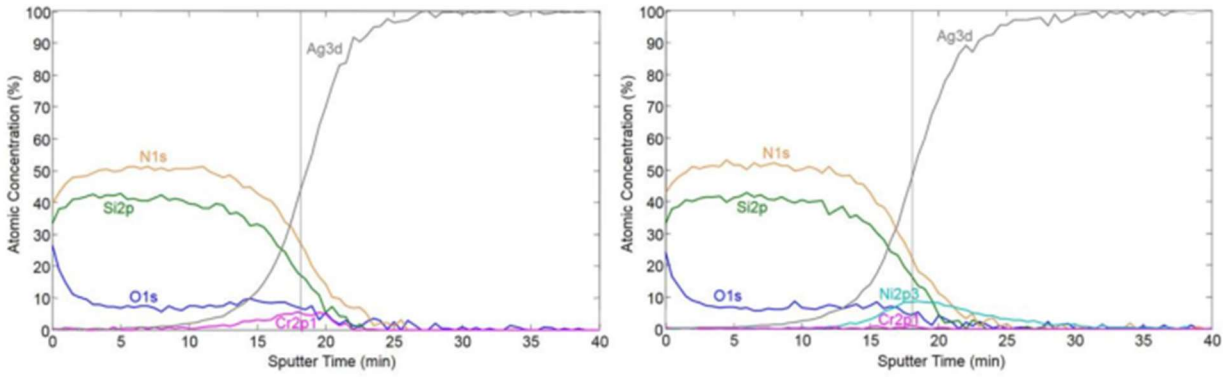

Figure 2.13: XPS depth profiles of as-deposited Ag mirrors using a CrN_x adhesion layer (left) and a $NiCrN_x$ adhesion layer (right). Adapted from [94].

Regardless of the precise functioning of it, Ni diffusion into Ag is definitely a key factor: Wolfe *et al*. reported the formation of a mixed Ni-Ag phase which noticeably increased absorption and sheet resistance of the Ag coatings, and specifically observed the optical and electronic changes on functional sample [113]. Xu *et al*. investigated the relation between $NiCrN_x$ coating thickness and durability, finding, intuitively, that thicker films promoted higher durability. More interestingly, perhaps is that this relation appears to be somewhat sensitive: for a given test, films which did not significantly degrade show no meaningful variation in their performance, implying a critical thickness of $NiCrN_x$ at which the coating was durable enough to undergo testing successfully [112].

CHAPTER 3 METHODOLOGY

The experimental methodology used in this work will now be exposed. Experiments typically proceeded by depositing stacks with different architectures or materials in different growth conditions, followed by the assessment of their optical performance as AR coatings (R_V, T_V, A_V) by spectrophotometry or of the material properties by spectroscopic ellipsometry, allowing one to make use of experimental data for predictive modeling. Rather than continually evaluating the durability of the samples created, durability was evaluated as new techniques to improve coalescence and optical quality were found to be of interest, most often using optically non-optimized samples in the goal of isolating the effect of specific techniques on coating durability. This section aims to reflect this by first detailing the deposition and cleaning processes used to fabricate samples, followed by the optical characterisation and modeling tools employed, and then the durability testing procedures. Finally, additional characterisation methods used as part of this work which do not fit into the previous categories are presented.

3.1 Sample fabrication

The samples used in this work were produced by electron beam (e-beam) evaporation and magnetron sputtering, as the former is currently used in the ophthalmic lens coating industry, whereas the latter is in use in industries already commonly using thin Ag films, such as for the production of low-emissivity glass coatings, and is better suited for implementing the deposition of durable Ag alloys [5], [114]. Each of these techniques will be very briefly described theoretically as to understand the intrinsic differences between them, followed by the practical aspects relevant to this work.

Before addressing deposition techniques, however, sample substrates and their cleaning must be addressed: appropriate cleaning is absolutely necessary as contaminants can reduce surface energy and adhesion, and lead to chemical degradation of the Ag layer if deposited directly upon the substrate [55]. Dielectrics are typically considered to suffer less from this, and as such the deposition of a dielectric seed layer followed by the deposition of the Ag film without breaking vacuum should lessen the impact of any remaining surface contamination. The presence of particles on the surface is equally an important issue, as they can lead to the formation of pinholes or other defects in the protective layer and throughout the coating, accelerating degradation [115].

Samples were deposited on circular, plane polymer substrates, pre-coated with a scratch-resistant hard coat, supplied by Essilor Canada, hereon referred to as Orma substrates, and borosilicate (B270) glass. Orma substrates are individually packaged in envelopes lined with a tissue, and are assumed to be kept clean as they are processed following the addition of the hard coat: as such, assuming that there is no contamination during manipulations, removal of any large particles (i.e. lint from the tissue lining) with dry nitrogen gas and ionic cleaning methods (detailed separately for each deposition process) were assumed to be sufficient. B270 substrates were cleaned with de-ionized water and isopropanol, once while rubbing to assist particle removal and a second time without, then dried with nitrogen, and finally exposed to ionic cleaning. B270 samples could also be prepped by CO_2 snow cleaning once the system was acquired. For this method, the substrate is heated and sprayed with a high velocity stream of CO_2 gas and solid particles which both supply mechanical removal and can be temporarily liquefied at the interface, dissolving hydrocarbons and other contaminants before being removed by the gas flow [116]. This method was shown to be equivalent to the other implemented cleaning method and was also completed with ion pre-cleaning (IPC) prior to the deposition.

3.1.1 E-beam evaporation

E-beam evaporation is a form of thermal evaporation, where the material is heated by a beam of high energy electrons; to achieve this, a cathode filament produces electrons which are accelerated and deflected by an electric potential and magnetic field, respectively. This allows to direct the electron beam to the evaporant without leaving a line of sight between it and the filament, ensuring that contamination from the latter is minimised. The crucible containing the material is cooled, which, combined with the localized heating of only a part of the evaporant, allows high deposition rates even for materials with high sublimation temperatures and limits any contamination from the crucible [53]. Naturally, as the impinging particles are merely heated to evaporation, and drift to the substrate unbothered due to the low pressure within the chamber, they impinge with a kinetic energy only of the order of 0.1 eV [22].

The samples produced by e-beam evaporation as a part of this work were deposited in a Leybold Optics BOXER Pro system, specifically made for the deposition of ophthalmic coatings in industry. Base pressure in the system is of the order of 5×10^{-7} mbar ($\approx 4\times10^{-7}$ Torr). The system uses a single

electron gun with a rotating crucible holder, and thus does not allow co-deposition of multiple materials simultaneously but permits up to 7 different materials to be evaporated without breaking vacuum. It is also equipped with a resistive evaporation source (in which a crucible containing the evaporant is heated by Joule effect), however as it allows significantly more contamination than the e-beam source, its use is strictly limited to the deposition of an optional anti-smudge coating (discussed in section 3.3.3). A crystal quartz microbalance (QCM) monitors the deposition, i.e. a quartz crystal resonator measures the change in mass per unit area through the change in its resonant frequency. As such, a precise measure of mass-equivalent thickness is available *in situ*, assuming the proper mass-to-thickness ratio is accounted for. Deposition rates are controlled by adjusting the e-beam current based on feedback from the QCM with a proportional integral derivative (PID) controller; however, to achieve a constant deposition rate, a manually defined pre-heating phase must be used so that at the start of deposition the e-beam current and material evaporation rate are within an acceptable range to avoid deviations.

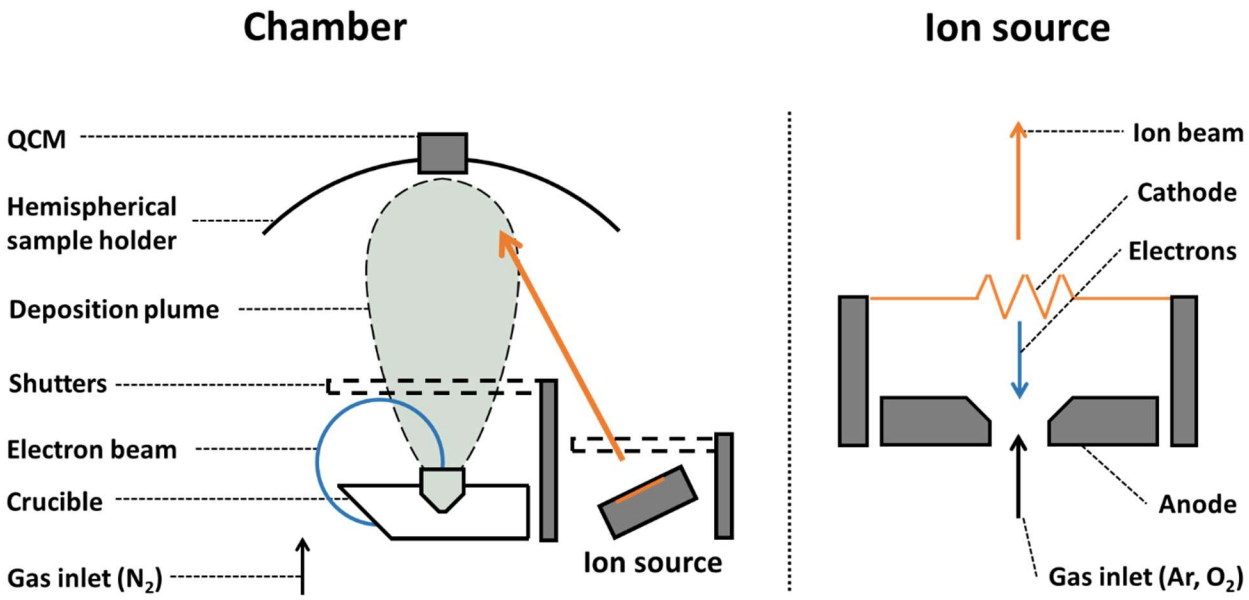

Figure 3.1: Schematic representation of the e-beam evaporation system and ion source used.

Finally, the system is outfitted with a KRI end-Hall 1000 ion source, in which electrons are produced and accelerated through an ionisation zone, just above a gas inlet; in doing so they create positive gas ions which are accelerated *away* from the source, due to their opposite charge, and onto the sample. This technique is referred to as IAD (ion assisted deposition) and can be used to

offer kinetic energy to adatoms on the surface and/or to add reactive ions to change the nature of the deposited material, depending on the type of gas used. A permanent magnet insures focusing of the produced beam, and electrons emitted *away* from the anode are sufficient to neutralize the beam [117]. The ion source is used in "auto gas" mode in this work, where the accelerating voltage (V_D) and emission (and discharge) current ($I_{E/D}$) are set manually; the gas flow is then automatically adjusted to satisfy those parameters. One can select a composition ratio to be maintained between gases, but only for O_2 and Ar gas: N_2 was not available to be configured for use in the ion source gas inlets, and is therefore inserted from a secondary inlet at a fixed flow rate, with Ar added through the ion source to adjust and stabilize the discharge variables. It should be noted that, although not systematically equivalent, (the emission current, produced by the cathode is the source for gas ionization, whereas the discharge current includes secondary electron produced from ionization) both are set to the same nominal values. Using a slightly higher emission current may reduce charging and thus arcing within the chamber, but as no such problems were observed during the course of this work, both were set to the same fixed value.

Samples produced by e-beam evaporation were, as previously mentioned, cleaned using an O ion beam, produced with an accelerating voltage of 250 V and a discharge current of 3 A, for a duration of 30 seconds, unless explicitly mentioned otherwise.

Table 3.1: Default deposition parameters for deposition processes by e-beam.

Material	**Dep. rate**	$\boldsymbol{V_D}$	$\boldsymbol{I_{E/D}}$	**Gas flow**
-	**[Å/s]**	**[V]**	**[A]**	**[sccm]**
IPC	-	250	3	O_2 : 15
ZrO_2	3.4	-	-	-
ZrO_2^{IAD}	3.4	300	2	O_2 : 10
SiO_2	7.6	-	-	-
ZnO	1.8	120	3.5	O_2 : 25
Ag	3.1	-	-	-
$Ag_{(N)}$	1.3	100	2	Ar : 5, N_2 : 25

3.1.2 Magnetron sputtering

Sputtering is a technique by which a solid target is vaporized by high energy impinging ions, which transfer sufficient kinetic energy to the target atoms to eject one or more from the solid matrix; magnetron sputtering is a specific embodiment of this technique in which the energetic ions are supplied by a plasma confined to the target surface. To accomplish this, a working gas, meant to constitute the body of the plasma, is inserted into the chamber; a potential is then applied between the target and anode; ions are formed from neutral gas atoms by collisions with electrons; finally, the ions are accelerated to the target, ejecting atoms upon impact. The magnetic aspect comes into play through the addition of a magnet behind the target, which confines the plasma in a closed circuit above the target: increased ionization and thus higher ion density significantly increases the deposition rate [53]. Of course, reactive gasses can also be used to alter the composition of the films, though reactive species can negatively impact the target (target poisoning), or even other targets within the same chamber. Naturally, the high energy involved in sputtering atoms from the target translates to significantly higher kinetic energy for atoms vaporized by sputtering than by e-beam, in the range of 5 to 10 eV, rather than ≈ 0.1 eV, which may induce morphological changes as discussed in section 2.2.2 and shown in Figure 2.6 [22], [50].

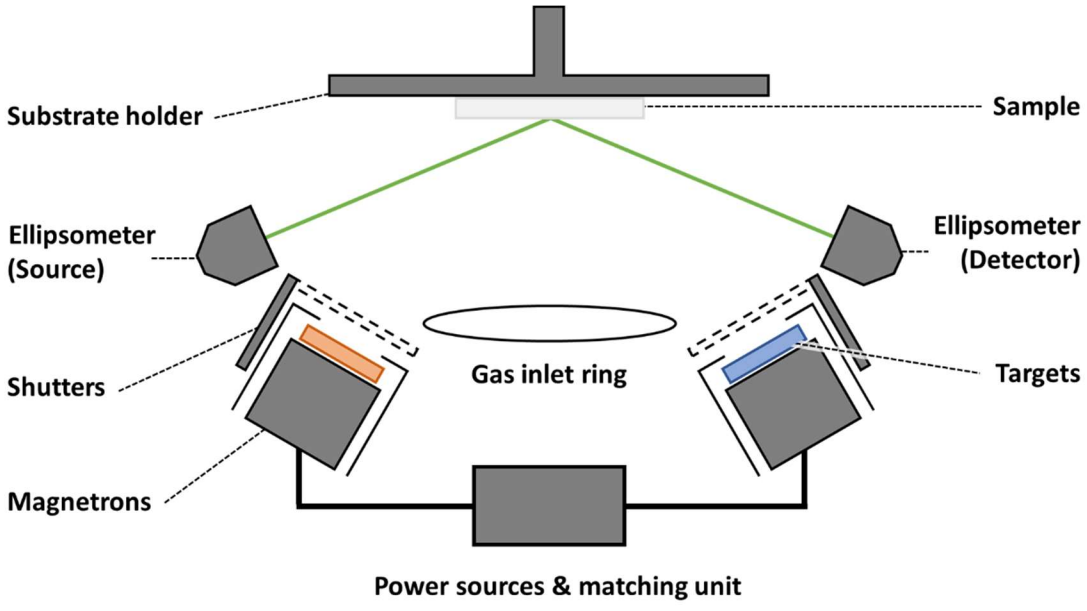

Figure 3.2: Schematic representation of the magnetron sputtering system used.

In this work, sputtered coatings were produced in a Kurt J. Lesker CMS-18 sputtering system. Base pressure within the system was of the order of $\approx 8\times10^{-8}$ Torr, with working pressures between 2 and 8 mTorr. The system is outfitted with 4 magnetrons equipped with 3-inch (76.2 mm) sputtering targets and 2 power sources, meaning that 4 different materials can be sputtered from without breaking vacuum, and 2 can be sputtered from simultaneously. One source is a DC (direct current) power source, which is embodied by the simple configuration used to theoretically describe sputtering previously, whereas the other is an RF (radio frequency) source: this latter type alternates the electric field at high frequency (typically 13.56 MHz), which, due to the higher mobility of electrons, allows one to reduce charge accumulation and use a dielectric as the cathode, i.e. the target. Gas inlets for Ar, O_2, N_2 and H_2 (hydrogen gas) allow different compositions of working gases to be used, allowing the deposition of multiple varieties of dielectrics both from metallic and non-conducting targets. The system is also equipped with a J.A. Woollam Co., Inc. M-2000 ellipsometer, (the functioning of which is detailed in section 3.2.2,) allowing one to monitor film growth and optical properties *in situ*, given that substrate rotation is not activated during acquisitions. In other cases, given the very steady deposition rate provided by sputtering, thickness can be derived from the deposition duration [6]. A quartz lamp heater can be used to heat samples over 300 °C, although temperatures above 100 °C quickly become irrelevant for use with polymer substrates.

Table 3.2: Default deposition parameters and average deposition rate for deposition processes by magnetron sputtering.

Material	**Target**	**Power**	**Pressure**	**Gas**	**Bias**	**Dep. rate.**
-	**-**	**[W]**	**[mTorr]**	**-**	**[W]**	**[Å/s]**
IPC	-	-	8	4 Ar : O_2	7	-
Ag	Ag	120 DC	4	Ar	0	≈ 3.2
$Ag_{(N)}$	Ag	120 DC	4	Ar : N_2	0	≈ 2.1
Al	Al	150 RF	4	Ar	0	≈ 0.35
NiV_x	NiV_x	150 DC	4	2 Ar : N_2	0	≈ 0.9
CrN_x	Cr	120 RF	4	2 Ar : N_2	0	≈ 0.15
Si_3N_4	Si	450 RF	5	5 Ar : 2 N_2	0	≈ 0.5
$Si_3N_4^{Bias}$	Si	450 RF	5	5 Ar : 2 N_2	5	≈ 0.35
SiO_2	Si	450 RF	2	10 Ar : 3 O_2	7	≈ 1.6

A bias voltage can be set between the chamber (which is grounded) and the substrate holder, accelerating plasma ions to bombard the surface during deposition, not unlike IAD although with less directionality and, potentially, a less defined energy distribution given the much more frequent collisions in this higher-pressure system. Biasing can be done independently of deposition, generating its own plasma to treat the surface. Ion pre-cleaning was performed in this way, using Ar gas with a working pressure of 8 mTorr, a bias power of 7 W resulting in a voltage of ≈ 100 V, for durations up to 5 minutes. Differing gas compositions and other details will be indicated whenever relevant.

3.2 Optical characterization

3.2.1 Spectrophotometry

Spectrophotometry measurements were performed with an Agilent Technologies Cary 7000 spectrophotometer outfitted with a universal measurement accessory (UMA), which allows automated transmission and reflection measurements at multiple angles. The bulk of acquisitions were simply performed with samples rotated at 6°. This allows one to measure specular reflection without disturbing the beam path and while registering minimal differences compared to normal incidence. Combining these with transmission measurements, also performed at 6°, can be used to isolate the intensity lost to absorption and scattering, which will be simply considered as absorption throughout this work, as the absorption of metallic layers is expected to far outweigh the effect of scattering. The spectra can then be converted to visual reflectance, transmittance and absorptance (R_V, T_V, A_V) using equation 3, which will be used as figures of merit of the coatings in this work.

These are useful to evaluate the overall intensity lost to absorption and that gained in transmission by decreasing the reflection; note however that these measures include the reflection from the backside of the substrate. For the substrates used in this work, the backside is expected to add approximately 4% to the reflected intensity across the visible spectrum: however, due to the presence of an absorbing metallic layer, intensity is lost before reaching the backside, inducing side-dependent reflection and absorption depending on which face the beam approaches from, all of which affects the backside reflection [32]. Thus, to reliably ascertain the effect of the coating on

the reflectivity, the reflection at the backside of the substrate must be suppressed. This is performed by making the backside scatter, obstructing specular reflection at the backside. Although this can be performed by mechanically roughening the surface, a much simpler and non-destructive process is to simply apply a piece of Scotch® tape with a matte finish; the tape has been shown to match the refractive index of substrates with $1.35 < n < 1.6$ sufficiently well that reflection at the substrate/tape interface is negligible, and scatters as well as a mechanically roughened surface [118]. With this simple technique, the reflectance of the frontside of the sample can be measured directly, allowing one to quantify the AR performance of the sample as its frontside visual reflectance, R_V^{FS}.

The system uses a wire grid polarizer to select polarization of the beam, which cannot produce unpolarized light; spectra were thus collected in *p*- and *s*-polarized light, after which the intensity spectra were averaged to obtain non-polarized equivalent spectra. The range and acquisition times for each measure varied somewhat over the course of the experiments, with signal-to-noise ratio standards being implemented to obtain higher quality data and wider acquisition ranges being used to probe degradation in the near IR, amongst others. Acquisitions always covered the visible spectrum, however, allowing to use R_V^{FS}, R_V, T_V and A_V as figures of merit in all cases.

3.2.2 Ellipsometry

Ellipsometry measures the polarization of a beam of light following reflection off a given sample (which generally results in elliptical polarization, hence the name) and compares it to the known polarization of the incident beam; it is then the ratio between the reflected amplitudes for *p*- and *s*-polarized light, r_p and r_s, which is used, as detailed in equation 18 below.

$$-\frac{r_p}{r_s} = \rho = \tan(\Psi)e^{i\Delta} \qquad 18)$$

where Ψ is the ratio of reflected amplitudes of each polarization and Δ is the dephasing between them. There is some inconsistency in the conventions used for the expression of these quantities, as discussed by Muller; however, as long as a given approach remains consistent, it shouldn't cause any problems [119]. In practice, resolving optical properties form the measured values of Ψ and Δ rapidly becomes too difficult to address, particularly in systems with multiple or absorbing thin

films, as is the case in this work. Therefore, ellipsometry is considered an indirect characterization method and used in a model-based approach.

In this work, ellipsometry modeling was performed with J.A. Woollam Co., Inc.'s *Complete EASE* software, in which Ψ and Δ of the sample are measured, a preliminary model detailing the expected thickness and optical properties of the different layers of the sample is used to calculate the expected response, and the two are compared, using the mean square error (MSE) as a figure of merit for the model. A regression algorithm can then be applied, varying the value of any number of parameters over defined ranges in an attempt to minimise the value of the MSE. This is a useful approach in the sense that it can return precise values even within complex systems, based solely off short, non-destructive measures. They are just that, however: values *based off of* measures. The model cannot create additional objective information from existing measures, and the validity of the produced values depends on the validity of the model. The regression algorithm can easily misidentify a local minimum of the MSE as the global one, leading to inaccurate measurements. As such, the first iteration of the model must be relatively accurate for this procedure to function properly.

To achieve this initial accuracy, the individual layers within a system must be well characterized, including the substrate. Using spectroscopic ellipsometry, that is ellipsometry performed over a given spectral range, one will have $2m$ data points, that is one value of Ψ and Δ for each of m studied wavelengths. There will however be at least $2m$+1 parameters to resolve for a given layer, that is m values of n and k, as well as one parameter for the thickness of the layer. There are a few manners to address this; for thin transparent films in the range where k can be neglected, the number of unknowns decreases drastically. For absorbing films, one can deposit coatings that are sufficiently thick ($\approx$ 100 nm) to suppress effects from the backside, thus eliminating the effect of the thickness, allowing a direct transformation of Ψ and Δ into n and k. As it assumes measurement from a uniform slab and does not take roughness or surface species into consideration it is therefore only approximative, and the resulting indices are referred to as pseudo-indices [6], [120]. Alternatively, supplementing ellipsometry data with transmission spectrophotometry data can help resolve the thickness of absorbing films [120]. All these means aside, perhaps the best way to utilise spectroscopic data is simply to combine it with physically appropriate models for their optical constants: in section 2.1.3, it was shown how the electronic structure of metals and dielectrics

differed and changed the analytical expressions of their optical properties. These relate the optical properties at one wavelength to the others and their feasibility can be a good marker for the validity of the results; a dielectric modeled with a Drude oscillator, for example, does not hold water regardless of whether or not it allows one to lower the MSE. Between this and the fact that thickness does not change with the wavelength, which allows an evaluation of the thickness at each wavelength, spectroscopic ellipsometry can greatly improve the evaluation of simple multilayers or allow the inclusion of other parameters such as roughness or the presence of an interphase [6]. With proper thickness monitoring during deposition and prior characterization of material properties, complex stacks can be well characterized. That being said, there are additional ways to improve characterization intrinsic to different ellipsometry systems.

In the context of this work, *ex situ* ellipsometry was performed using a J.A. Woollam Co., Inc. RC2-XI ellipsometer, equipped with dual rotating compensators, CCD detection and variable angle acquisition. This allows high measurement speed and accuracy, and acquisitions at multiple angles can introduce additional data. Acquisitions were performed over a 200 nm to 1700 nm range, (notwithstanding a system upgrade which expanded the IR range to 2500 nm,) and at angles of incidence of 45°, 55°, 65° and 75° as part of a single measurement sequence. These angles tend to surround the range in which most transparent materials would have their Brewster angles, at which the extinction of *p*-polarized light will cause important shifts in Ψ and Δ, and is thus most likely to introduce meaningful additional data in dielectric layers and in more complex stacks.

In situ ellipsometry was performed within the CMS-18 sputtering system using a J.A. Woollam Co., Inc. M-2000 ellipsometer, as mentioned previously, in section 3.1.2. This ellipsometer uses one rotating compensator as well as a CCD detector, and naturally functions only at a single angle of incidence, covering a spectral range of 300 to 1648 nm. It nevertheless benefits from fast acquisition times allowing to take measures within the deposition chamber either in between steps, to individually characterize layers and reduce the unknowns at each subsequent step of a stack formation, or continuously throughout deposition, if substrate rotation is turned off. In this case, film characteristics and thickness can be monitored over time. Normally, film characteristics are not expected to change throughout the deposition, allowing one to reliably ascertain the thickness.

Alternatively, for thin Ag layers, whose optical properties change significantly as they become continuous, one can use the change in optical properties to monitor the coalescence of the film. To do so, substrate properties are fitted before deposition. *In situ* measurements are then performed throughout the deposition; an estimate of the mass-equivalent thickness is achieved by fitting the thickness of the film after deposition, while using the reference optical properties reported by Palik. Thickness is then re-fitted along with the optical properties and compared to previous results as validation. Finally, the thickness is fitted backwards in time, with the MSE increasing as the optical properties no longer correspond to those of the continuous film fitted previously. In the remainder of this work, this technique will be referred to as time-reversed fitting. It should be noted that the model breaks down in the early stages of Ag growth. This is touched upon briefly in Appendix A.

3.2.3 Modeling

Although *Complete EASE* is able to model stack interference and predict the reflectance, transmittance and absorbance of multi-layer coatings, it is not expressly designed with this purpose in mind – therefore, stack interference modeling was performed with *Open Filters*, which will not be described at length, as it has already been thoroughly detailed by Larouche and Martinu [32]. It suffices to say that this software is particularly interesting for this work as it can optimize for a wide variety of criteria, including minimizing R_V and maximizing T_V. However, it only returns discrete solutions; thus, a home-made code was developed in *Python* to permit mapping of R_V and T_V over a wide range of parameters.

The code uses a few useful simplifications: namely it considers a 0° incident angle, which allows one to use only *s*-polarized light and simplifies the expressions for reflectivity at each interface and optical path length, it neglects backside reflectance by assuming a semi-infinite substrate, which would require to implement reverse calculation of interference in the stack, a costly addition given that it can be easily calculated for specific configurations of interest with *Open Filters*. Finally, this code condenses the calculated reflectance and transmittance spectra to R_V and T_V immediately, freeing up random access memory to allow an unremarkable computer to compute performances for a large parameter space.

The code allows one to select the illuminant and observer functions of their choice, though naturally the D65 illuminant and CIE standard observer are used by default. The user then selects optical

constants for a substrate, and the default thickness and optical constants of a given number of layers. Once the stack has been configured, the user selects two layers whose thickness is to be varied as part of the mapping and up to 3 more layers, for which one can vary the thickness or the complex refractive index, by using a linear combination of the optical constants of SiO_2 and TiO_2, referred to as CRI layers (custom refractive index). As the entirety of the resulting data is stored to be displayed (as shown in Figure 3.3), R_V, T_V, or A_V maxima or minima can be identified in a selected range, and thus the user can isolate the effect of certain parameters on the merit of the AR coating design.

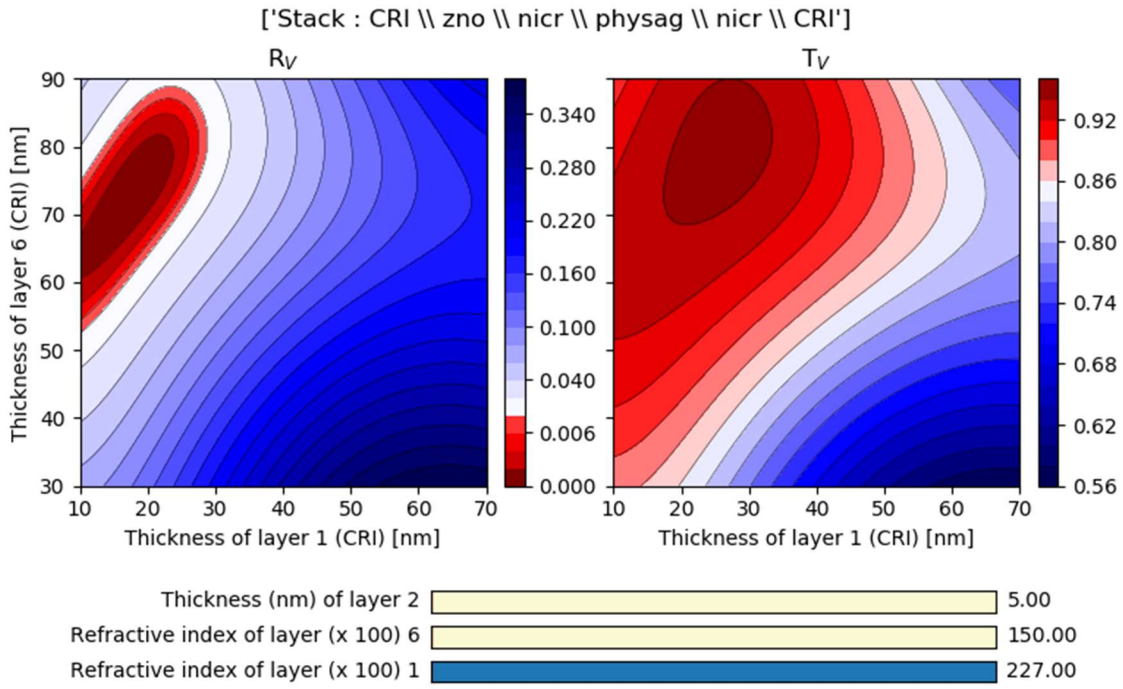

Figure 3.3: Example of R_V and T_V mapping of an AR coating produced with *Python*.

3.3 Durability testing

To maintain meaningful comparison with the durability of other ophthalmic lenses, testing was intentionally made to be as similar as possible to standardized tests used by Essilor and in the work of Caron [12]. That being said, Ag films are qualitatively different than dielectric films, and the AR stacks incorporating them were likewise expected to face different challenges from the start: thus, emphasis on certain tests and modification of the testing procedures to best suit this new type should not come as a surprise.

3.3.1 Temperature test

The resistance to thermal strain was tested by enclosing samples in a heated, dry enclosure for a duration of one hour, then removed to room temperature to visually observe for the presence of cracks: in the eventuality of no visible cracking being present, samples could be further studied by evaluating the reflection and transmission spectra or observing the sample under an optical microscope to find cracking. Samples were heated to temperatures ranging from 50 to 110 °C, by increments of 10 °C. The development of a more quantitative method of evaluating the onset of cracking is under investigation but has yet to be implementable as part of this work.

3.3.2 UV radiation test

The resistance of samples to (solar) UV radiation was performed with a *Suntest Heraeus CPS+*, with power set to reproduce solar UV intensity in the 300 to 380 nm range. Testing was performed for up to 200 hours per sample, with intermediate spectrophotometry measures at 40-hour increments to evaluate if significant degradation has begun, in which case the sample is considered to have failed, and the test can be stopped.

3.3.3 Mechanical durability test

The Nx10B (or N×10 blow) test was used to evaluate durability to abrasion and delamination as a whole: it consists of an eraser-like rubber wedge which is pressed onto the sample with a normal load of 12 N, which approximately corresponds to the weight force of 1.2 kg (or 2.5 lbs). A teacloth soaked in isopropanol is placed between the sample and wedge, with the “rough” side of the cloth against the sample. To simulate the effect of a user manually cleaning their glasses, the sample is then rubbed against the wedge in a linear reciprocating movement, with each back-and-forth pass being considered one blow to the sample: as the name indicates, one can then select a number of blows to submit the sample to, in increments of 10 blows. Durability is evaluated by observing the sample by eye, and with assistance of an optical microscope once damage becomes apparent. Observations are performed regularly up to N=12, at which point the sample is considered to have passed testing, though additional exposure can be performed as a means of insurance.

This test is typically performed on curved lenses, with the wedge applied on the convex side of the lens. Given this, the wedge is square edged and for plane Orma samples, as are used in the context

of this project, there may be discrepancies due to the corner of the wedge enhancing (or a higher contact area reducing) the degradation speed. Finally, to best replicate the reality of an ophthalmic lens, samples were coated with an anti-smudge coating (OPTOOL DSX) prior to testing. The coating is deposited by thermal evaporation from a liquid source at very low thicknesses (≈ 1 nm). Similar fluorine-based coatings are applied to the majority of ophthalmic lenses [5]. The coating's low refractive index, combined with its low thickness, induces a minor, if not negligible change in optical properties and the increased lubricity and hydrophobicity of the surface promotes sliding of the wedge over the surface; without it, the test is not representative of real usage conditions.

3.3.4 Humidity test

Sample durability under exposure to high humidity was tested by enclosing samples in a glass container, deposited on a rack above a layer of water; the container was placed on a heating plate and sealed, to ensure saturation of humidity, except for a small opening through which a thermocouple was inserted to monitor the enclosure's temperature. Testing was performed at temperatures of 60 °C and 80 °C for a duration of 2 hours each, with sample observation following each test and spectrophotometry measures being taken when relevant.

It should be noted that, albeit stress due to water intake in the film layers (or polymer substrate) can cause sample cracking under high humidity, it is only one of the failure mechanisms offered by high humidity. Water condensation at the surface, possibly mediated by the presence of small particles on the sample, can permeate through the top dielectric layer, and thus expose the samples to a solution containing common airborne contaminants, which may easily include Cl or S, and thus enable corrosion [25], [115]. Moreover, it is plain to see that cracking offers easy paths for condensed water to reach through the dielectric layer, enhancing corrosion.

3.3.5 Saline corrosion test

Finally, coating durability is evaluated following immersion in a saline solution. This may seem to be specifically targeted to Ag films given the previous discussion in section 2.3, or somewhat irrelevant to dielectric coatings, although this is not the case. Not only does immersion promote high amounts of water intake, the reactive environment provided by the saline solution can degrade dielectric coatings as well. The test used by Caron, which of course emulates the testing conditions

in industry, consists of submerging the sample in an aqueous solution with 200 g of NaCl per liter, (approximately 3.5 mol/L,) held at a temperature of 50 °C, for a duration of 20 minutes [12]. In the remainder of this work, these will be referred to as benchmark testing conditions.

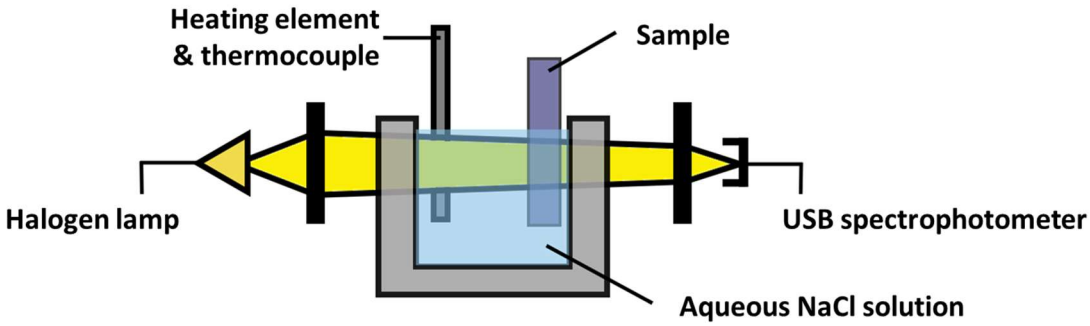

Figure 3.4: Schematic representation of saline corrosion test configured for use with *in situ* transmission spectrophotometry.

This test was too severe to extract much meaningful data from initial samples, however. Testing was first shifted to a longer immersion time at room temperature, with a much lower NaCl concentration of 0.1 mol/L, as used by Koike *et al* [121]. These will be referred to as decelerated testing conditions. To bridge these different testing conditions and allow more quantitative data, a new testing procedure was developed in which an electrochemical testing cell was reworked to allow *in situ* transmission spectrophotometry of the samples during testing. As pictured in Figure 3.4, a halogen lamp was used as a light source, which was focused through the windowed cell and to an optical fiber connecting to an *Ocean Optics* USB2000 spectrophotometer. The solution's temperature was controlled by using a resistive heating element and thermocouple, connected to a *Zesta* PID temperature controller.

Given the spectral range of both the light source and the detector, the bulk of the data used was the measured luminous intensity at 550.1 nm, approximately the peak sensitivity of the CIE standard observer: any discrepancies from this are accounted for when presented in this work. Sample durability was quantified for given concentrations and temperatures by two critical times, t_{C1} and t_{C2}, corresponding to the time at which meaningful degradation begins and ends, as shown in Figure 3.5. Naturally, there is no simple way to define 'meaningful' degradation, which introduces a qualitative element to the determination of critical times. Using the time derivative of the intensity

was initially suggested as a means to more quantitatively define t_{C1} and t_{C2}, but the majority of the data used was not an elegant sigmoid-like curve, as in Figure 3.5. Temperature and concentration both affect the noise and stability of the signal, and material erosion, partial or total delamination, or other means of degradation can qualitatively alter the evolution of the intensity, making the semi-qualitative approach more robust, if less precisely defined. More details on the effect of temperature and concentration on the signal quality and on sample degradation are presented in section 4.2.1.

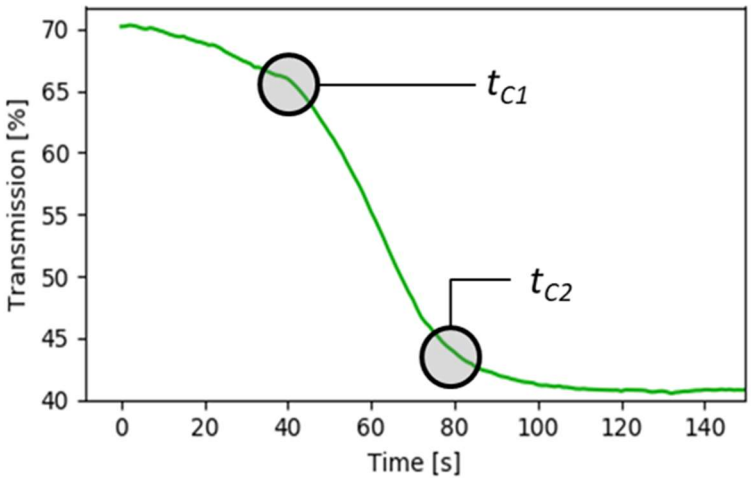

Figure 3.5: *In situ* transmission spectrophotometry measurement demonstrating the degradation of an unprotected AR stack during decelerated saline corrosion testing.

3.4 Additional characterization methods

3.4.1 Contactless sheet resistance

An alternate method of evaluating the continuity of metallic thin films is by evaluating their sheet resistance, that is the resistivity of a coating parallel to and within the plane it forms, specifically. Naturally, as a Ag coating reaches its percolation threshold, and conduction paths emerge, the sheet resistance of the layer drops extremely quickly, tapering off as the film completes coalescence [70].

In this work, sheet resistance was measured with a Delcom 737 contactless sheet resistance probe from Delcom Instruments, Inc. For a coating which is spread over a large surface, relative to the probe size, the length over which current will travel is essentially the same as the width it may

travel over, which allows a geometric simplification to rewrite the sheet resistance in ohms per square (Ω/□), which is equivalent to the resistivity (ρ) of the material divided by its thickness. Thus, as thickness decreases, even for high quality, conductive films, sheet resistance will increase. Moreover, certain samples used in this work were not deposited on sufficiently large substrates (minimum size is a 2.54 cm diameter circle) to ensure a highly stable reading; in such cases, appropriate error bars are included.

3.4.2 X-ray diffraction

For a given wavelength, constructive interference will occur if the optical path length between two parallel reflecting planes is equal to an integer multiple of the wavelength. This becomes interesting for X-rays, as their wavelength is of the order of interatomic spacing: thus, by finding the optical path length for which constructive interference is observed, one can probe the crystal structure of materials: this is X-ray diffraction (XRD).

In this work, a Bruker Discover 8 XRD system was used. Measurements were performed at a fixed grazing incidence (GIXRD) of 1 degree while the detector position is varied. This has the advantage of providing higher signal for very thin films and provides information on the overall crystalline structure rather than the crystal orientation aligned to the surface. The width of signal peaks can be used to estimate the average grain size of a given material using the Scherrer equation, performed in this work with *DIFFRAC.EVA*, an XRD analysis software. This method can be affected by a number of factors, including film stress, and tends to over-estimate grain size, and data must be treated accordingly.

3.4.3 Stylus profilometry

As mentioned, albeit a powerful tool, ellipsometry relies on model-based analysis: to obtain good results from the algorithmic optimization of these models, good starting points for input parameters are necessary. Thus, to assist ellipsometry as a means of resolving film thickness, a Bruker DektakXT stylus profilometer was used, particularly during initial characterization of newly deposited films where adding spectrophotometry data was not of use.

CHAPTER 4 RESULTS & DISCUSSION

As this work concerns itself with two highly distinct aspects of the AR coating, this chapter has likewise been separated into two main sections, concerning the coalescence of silver films (which is essential to their optical performance) and their durability within the completed stack.

It should be noted that results do not follow a strict chronological order: durability and performance were tested throughout the entirety of the project although initial experiments were carried out by e-beam evaporation, as this is what is currently used in the ophthalmic industry and offers the most insight into metal-based AR coatings' practical applicability. However, improvement of durability required a transition to magnetron sputtering where certain deposition methods were more easily implemented.

An eventual return to e-beam evaporation was planned, wherein a selection of the most useful techniques could be implemented. However, due to circumstances beyond control, namely laboratory shutdowns as part of the COVID-19 pandemic response, this and other objectives could not be accomplished. Rather, a synthesis of the main results and of likely avenues of improvement determined from current results is presented in the following chapter.

4.1 Improving silver film coalescence

4.1.1 Preliminary results

Initial depositions focused on calibrating the e-beam heating recipes for Ag and ZrO_2, which was *de facto* the basic dielectric used in e-beam evaporation, quickly implemented in a basic stack design meant to be a starting point from which to compare new developments. This design, hereon referred to as configuration A, is schematically represented in Figure 4.1. ZrO_2 layers were deposited at a nominal rate of 3.4 Å/s: optical properties were found to better replicate expected values when using IAD, with an accelerating voltage of 300 V, a discharge current of 2 A and O_2 gas as an ion supply. The upper layer was deposited without IAD to ensure that the Ag layer was not oxidized, as indicated by the (lack of) IAD superscript. IPC was performed with Ar gas instead of O_2, for a duration of 3 minutes as opposed to 30 s. Ag deposition conditions will be specified on a case-by-case basis.

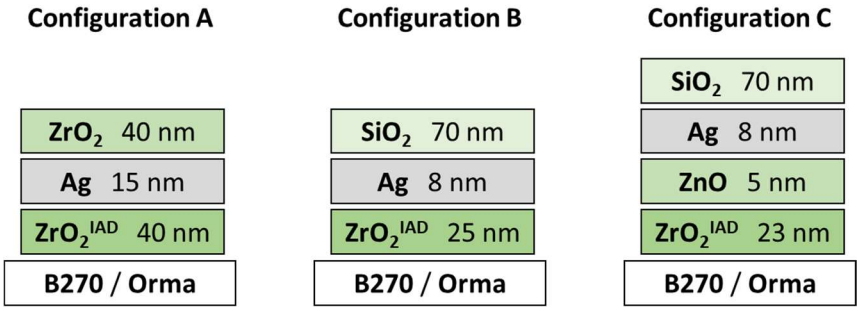

Figure 4.1: Nominal layer configurations A, B, C, used in different AR designs. Default deposition parameters can be found in Table 3.1. Other details can be found in the text.

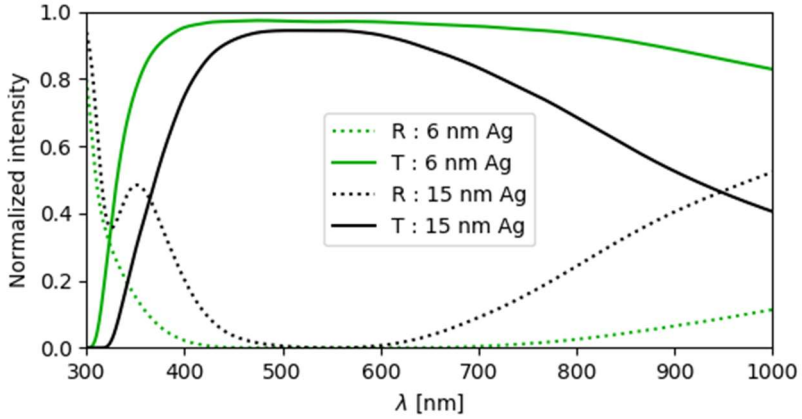

Figure 4.2: Modeled transmittance (full) and reflectance (dotted) spectra of AR coatings optimized by *Python* code and plotted with *OpenFilters* for fixed Ag thicknesses of 6 and 15 nm. Optical properties by Palik were used for the Ag layers.

Concurrently, the *Python* code was used to determine the key elements necessary to produce more performant dielectric-metal-dielectric architectures. Using default illuminants and observers and B270 as a substrate, the theoretical performance was mapped using Palik's optical constants for Ag, obtained from *Complete EASE*, over thicknesses ranging from 6 to 15 nm, with CRI layers for both dielectrics, with thicknesses ranging from 10 to 90 nm. It was found that the minimum predicted value of R_V decreased steadily with decreasing Ag layer thickness, from nearly 1% at 15 nm to 0.03% at 6 nm (shown in Figure 4.2, conditional to a decrease of the upper layer's refractive index (at 550 nm) from ≈ 2.3 to about ≈ 1.50. Therefore, improving the coalescence of Ag films is not merely a question of reducing plasmonic or intrinsic metallic absorption, but also a means of

enabling more performant AR coatings, reinforcing the association between coalescence and performance.

4.1.2 Increased deposition rate

Before approaching more elaborate methods of promoting Ag coalescence, such as doping or the use of seed layers, improvement to the performance of configuration A (the initial configuration used in this work, see Figure 4.1) was attempted in the simplest terms, to provide a good starting point for future experiments. The simplest means of doing so is, straightforwardly, to increase the deposition rate: as discussed in section 2.2, this is tantamount to an increase of the supersaturation, which is expected to increase the nucleation density in turn.

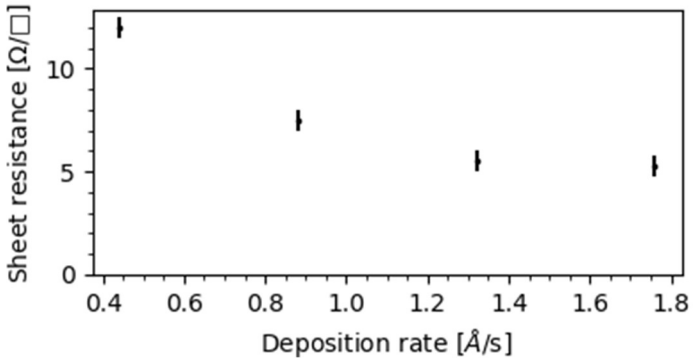

Figure 4.3: Sheet resistance of samples deposited by e-beam in configuration A (see Figure 4.1), as a function of the deposition rate.

Unsurprisingly, for a fixed thickness of 15 nm, there is a limit to which the sheet resistance converged, as shown in Figure 4.3: as the deposition rate increases and an earlier coalescence is promoted, more continuous films of even thickness are obtained, which allows for a higher conductivity, but once a fully continuous film is formed promoting an earlier coalescence does not allow to lower the sheet resistance. If anything, an increase in grain boundaries or other such scattering points could theoretically increase it, if only by a marginal amount [44].

That being said, even for significantly higher deposition rates, thinner Ag layers failed to fully coalesce, as shown in Figure 4.4. Despite taking the effect of film thickness on sheet resistance into consideration by comparing resistivity, one finds that neither of these are within the same order of magnitude as bulk Ag the 9 nm Ag film deposited at a rate of ≈ 3 Å/s has $\rho \approx 16\times10^{-8}$ Ω·m, which

is hardly more conductive than the 15 nm film deposited at a rate of ≈ 0.5 Å/s, has $\rho \approx 18\times10^{-8}$ Ω·m. More importantly, decreasing the thickness further quickly exacerbates the problem, accompanied by a predictable rise in absorption.

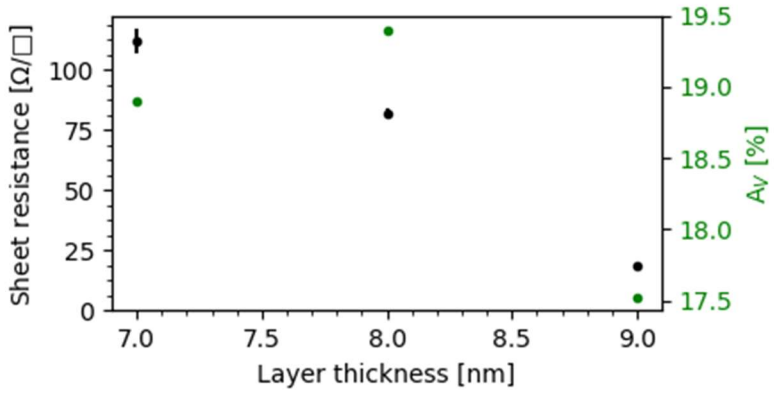

Figure 4.4: Sheet resistance and A_V of samples deposited by e-beam in configuration A (see Figure 4.1) with Ag layers deposited at a nominal rate of 3.1 Å/s, as a function of the Ag layer thickness.

This diminishing gain observed as deposition speed increases is consistent with the general trend of equation 16, implied by the logarithmic relation between critical cluster size and supersaturation. Again, though this equation is not suited for predictive, quantitative use, nor can the nucleation density be straightforwardly obtained from the critical cluster size, it is sufficient to justify large increases in deposition rate to achieve a lower coalescence threshold.

This is precisely what was done to create the first iteration of a more performant AR architecture, presented in Figure 4.1 as configuration B. In this configuration, IPC and ZrO_2 deposition parameters remain the same. To capitalize on the lower thickness of the Ag layer, the top layer of ZrO_2 is substituted with a layer of SiO_2, evaporated at a nominal rate of 7.6 Å/s. As in configuration A, IAD is not used for this layer to avoid damage to the Ag layer. Ag was deposited at a mean rate of 2.7 nm/s, i.e. approximately 10 times the deposition rate employed for previous samples. Ag deposition was supplemented with passive O_2 exposure by allowing a 1 sccm flow of O_2 into the chamber, as detailed in the following section. However, as there were no adjustments for the deposition rate, the O_2/Ag ratio is expected to likewise be about one-tenth of that which is found for 1 sccm of O_2 in Figure 4.6, and thus it is assumed to not have a major effect on the coalescence

of the film. The transmittance and reflectance spectra of the produced coating are shown in Figure 4.5.

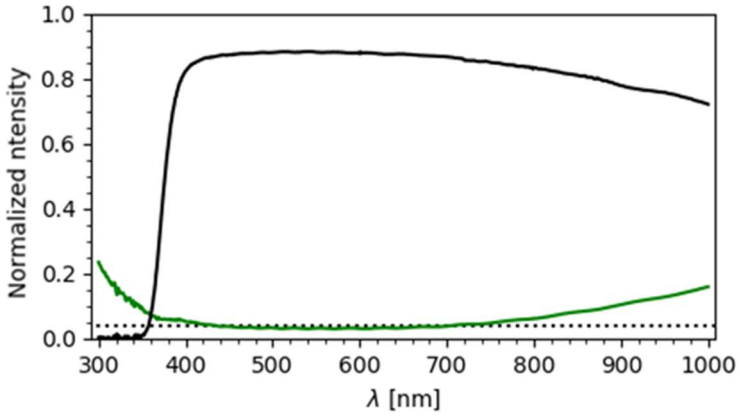

Figure 4.5: Transmittance (black) and reflectance (green) spectra of an AR coating in configuration B deposited on an Orma substrate (see Figure 4.1). The dotted line is set at 4%, the approximate contribution to the reflection from the backside of a sample. Optical properties are found in Table 4.2 and Table 5.1.

Although this sample was shown to be highly performant, with R_V = 3.2%, T_V = 88.0%, A_V = 8.8% and R_V^{FS} = 0.3%, the sheet resistance of 18.5 ± 0.5 Ω/□ (ρ = 14.8 ± 0.4 ×10^{-8} Ω·m) suggests that the Ag film is not much more continuous than previous iterations. Moreover, this coating, if more performant, makes use of such a high deposition rate for the Ag layer that it makes it prone to deviations from the nominal thickness; it goes without saying that a process with poor repeatability is of little interest for practical, industrial application. Therefore, though it does highlight controlling the deposition speed as a means to improve Ag coalescence, it will not be implemented in the rest of this work given the problems with repeatability and as deposition rates and kinetics will change significantly with transition to magnetron sputtering deposition.

4.1.3 Oxygen-doped silver films

As mentioned in the previous section, the effect of doping Ag layers with O_2 was tested in both a passive mode, in which layers were deposited normally, while adding a fixed flow of O_2 gas into the chamber, and an active mode, in which case layers were deposited with O_2 IAD.

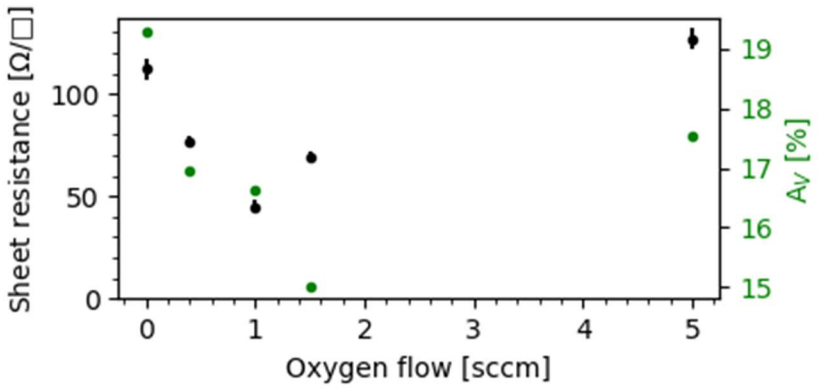

Figure 4.6: Sheet resistance and A_V of 7-nm-thick passively-doped $Ag_{(O)}$ layers deposited by e-beam evaporation in configuration A (see Figure 4.1) at a nominal rate of 3.1 Å/s, as a function of O_2 flow.

Figure 4.6 shows that the passive addition of a controlled amount of O_2 can significantly improve the coalescence of Ag films, displaying significantly lower sheet resistance and A_V. Of course, an overabundance of O within the $Ag_{(O)}$ layer reduces performance, as reported in the literature. Particularly, the observation of Wang that n increases and k decreases with O_2 content, is consistent with the observation that absorption continues to decrease as resistance increases at higher flow values, suggesting the weakening of the absorption mechanism as conductivity of the layer decreases [81]. These improvements are still lacking, particularly compared to the results of the fast-deposited sample in configuration B (see Figure 4.5).

Alternatively, $Ag_{(O)}$ deposition was performed with O_2 IAD. Using the same deposition rate, the Ag layer was deposited using an Ar:O_2 gas mixture supply to the ion source, an accelerating voltage of 250 V and a discharge current of 3A. Figure 4.7 shows important gains in performance for coatings making use of $Ag_{(O)}$ layers produced with the above-described IAD process. Unsurprisingly these gains are quite sensitive to the O_2 content of the gas mixture, with the best results found for an O_2 ratio of 1/12 of the total gas content. As total gas flow averaged approximately 12 sccm for all tested gas compositions, these results would correspond to a similarly approximate O_2 flow of 1 sccm.

Interestingly, this suggests that a similar O composition could be found in this layer as in the passively-doped $Ag_{(O)}$ layer produced with 1 sccm of O_2. However, the samples deposited with IAD perform significantly better, suggesting that the change in deposition kinetics significantly

improves coalescence as well. As previously, at higher O_2 content, absorption stays relatively low as sheet resistance increases, again in agreement with the cited literature.

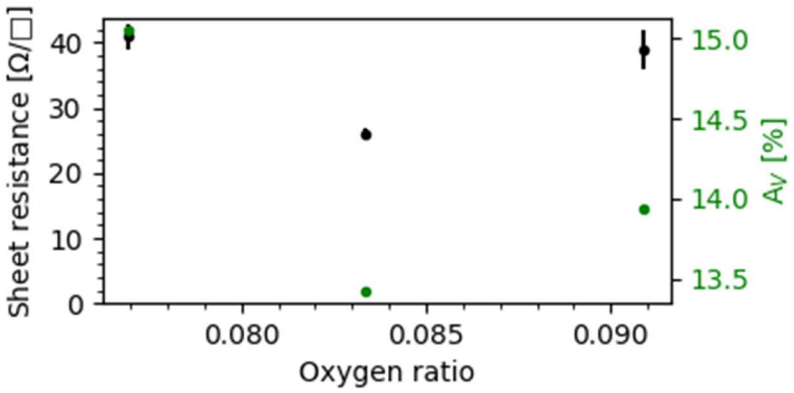

Figure 4.7: Sheet resistance and A_V of 7-nm-thick IBA-doped $Ag_{(O)}$ layers deposited by e-beam evaporation in configuration A (see Figure 4.1) at a nominal rate of 3.1 Å/s, as a function of the O_2 composition of the IBA discharge gas.

4.1.4 Dielectric seed layers

ZnO seed layers were tested as a means to promote Ag coalescence. Initial deposition tests by e-beam evaporation of ZnO pellets were inconclusive, resulting in extremely fragile films with a dark, cloudy appearance, suggesting highly sub-stoichiometric films. It was found that by using a low deposition rate, coupled with O_2 IAD, functional films could be deposited, with the expected clear appearance, no obvious fragility and measured optical properties matching expected values fairly well ($n(\lambda$=550 nm) = 2.01, compared to an expected value of 2.00).

Of course, beyond ZnO coatings which are merely functional, ZnO coatings which are performant are desired. Tentative XRD measures were performed on this first iteration of coatings; little crystallinity was observed. Varying the IAD conditions was approached as a means to promote the desired crystalline orientation, however all tested samples showed a similar lack of crystallinity. This is partly explained by low signal intensity in the measures performed; as grain structure may not be homogenous with increasing thickness, only thin (≈ 10 nm) layers were used in these measures, greatly limiting the signal. Rather than use thicker layers in XRD, however, ZnO quality was evaluated based on the performance of silver layers deposited on them, as shown in Figure 4.8.

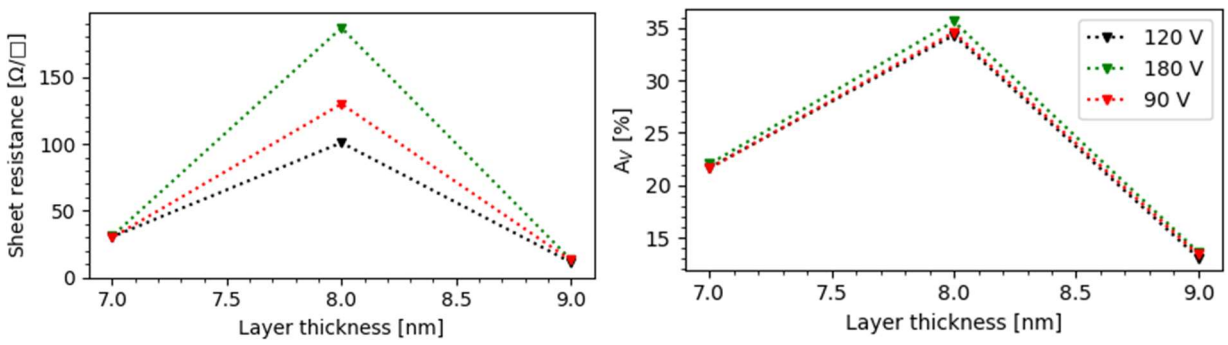

Figure 4.8: Sheet resistance and A_V of stacks in configuration C (see Figure 4.1), as a function of the Ag layer thickness, for underlying ZnO seed layers produced under different V_D. A PLC error occurred for the sample at 8 nm thickness. Dotted lines added for clarity.

To this end, samples were deposited in configuration C, wherein essentially all layers were prepared with the same parameters as previously; Ag was deposited at the *de facto* standard nominal rate of 3.1 Å/s, and ZnO was deposited at a nominal rate of 1.8 Å/s with O_2 IAD utilizing a discharge current of 3.5 A. Other than in Figure 4.8, the accelerating voltage was set to 120 V.

Figure 4.8 shows extremely minor changes upon variation of the acceleration voltage, in agreement with XRD data, except for the samples deposited with 8 nm of Ag, where a communication error with the PLC (programmable logic controller) caused an uncontrolled drop in deposition rate for the 8 nm thick Ag layer. Despite poor performance of this sample, it appears to indicate that the accelerating voltage of 120 V produces marginally better ZnO samples.

Beyond a simple fluke, possible explanations of this behavior would be that between 90 V and 120 V, ions become sufficiently energetic to effectively assist in re-structuring the layer. However, as voltage continues to increase for a fixed current, ionization efficiency increases and the gas flow required to maintain the discharge decreases (≈ 28 sccm of O_2 is used to sustain the 120 V discharge whereas only ≈ 21 sccm are used for the 180 V discharge). Thus, this change could be related to a change in stoichiometry due to the higher O_2 content. Wu *et al*., however, report O_2 pressure as having little effect on the crystal structure of ZnO, whereas increased substrate temperature in conjunction with IAD promotes epitaxial films, suggesting that adatom mobility and void dislodging would be the two main mechanisms leading to better ZnO films [122]. This is in agreement with modelling results by Müller, which suggest that ion energy must be past a certain

energy threshold to be effective, following which ion impingement rate must increase relative to the deposition rate [123]. Thus, it could be that at higher energies and lower O_2 pressure a *slightly* smaller amount of ions are formed, resulting in a *slight* decrease of ZnO efficiency. The possibility of improving ZnO films produced through an increase in ion current, amongst other means, is discussed in greater depth in 4.2.6; for now it suffices to say that due to the marginal improvement observed for films deposited at V_D = 120 V, these parameters were kept in following work with ZnO seed layers.

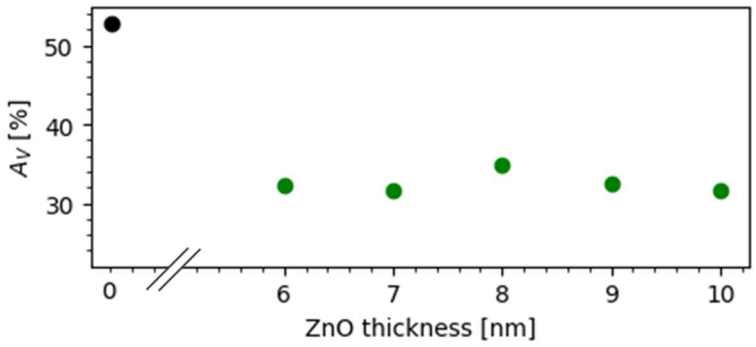

Figure 4.9: A_V of stacks in configuration C (see Figure 4.1) with 7-nm-thick Ag layers, as a function of the ZnO layer thickness.

The effect of ZnO thickness on performance was also evaluated similarly to Fukuda *et al*. who reported improved coalescence for thinner films, whereas the work of Tripathi *et al*. seems to suggest that although roughness or crystallinity change with film thickness, it should only be meaningful for higher ranges [73], [124]. Figure 4.9 shows no trend other than that the addition of ZnO is preferable to its absence. ZnO and ZrO_2 being both non-absorbing dielectrics with a real refractive index around 2.0, both are well suited as a seed layer, from an interference point of view. To validate that ZnO was better suited to promoting the coalescence of silver, two stacks, using each a different seed layer, but Ag films of the same thickness, deposited in the same conditions, were compared, as shown in Figure 4.10. The sheet resistance and A_V were measured at 11.5 ± 0.5 Ω/□ and 13.1% for the sample using ZnO as a seed layer, and at 18.7 ± 0.5 Ω/□ and 19.4% for the ZrO_2 seed layer. The significantly different configurations make comparison of reflectance somewhat irrelevant here, however. The increase in reflection in the NIR is expected for more

conductive films whereas that in the UV is due to interference with ZnO (which has an absorption band in the UV); neither has a significantly effect on the AR's performance.

When sample production started moving primarily to magnetron sputtering methods, it became necessary to validate whether or not ZnO substrates coated by e-beam evaporation would remain effective when transferred to magnetron sputtering, requiring to test this before finishing work by e-beam and switching to the other system.

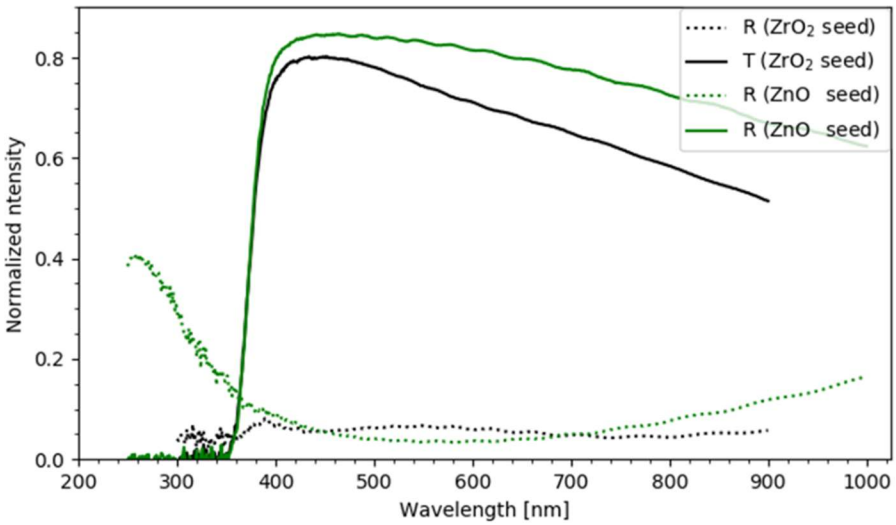

Figure 4.10: Transmittance (full) and reflectance (dotted) spectra of AR coatings in configuration B (black) and C (green) (see Figure 4.1). Both Ag layers were 9-nm-thick and deposited at a nominal rate of 3.1 Å/s.

It should be noted that in the model-based time-reversed fitting approach, the addition of ZnO layer to the stack introduces additional parameters to the initial fit; although the time-reversed fitting process is only performed on the thickness of the Ag layer, errors on other parameters will increase the model's overall MSE; thus the results with a ZnO seed layer will tend to have slightly higher MSE than simpler configurations with fewer parameters. Figure 4.11 shows the coalescence behavior of Ag deposited by magnetron sputtering on ZnO seed layers prepared by e-beam evaporation, as opposed to bare B270 glass substrates, showing that there is indeed a clear reduction of the coalescence thickness, despite the additional modeling error caused by the addition of the seed layer (the negative thickness observed is simply an artefact from modeling results at extremely low coverage). Moreover, it will also be demonstrated that even for thicknesses at which

Ag would fully coalesce, regardless of ZnO, the presence of this seed layers improves film quality and reduces A_V (see Figure 4.18). Moreover, it was found that an oxygen ion treatment was particularly useful when using transferred substrates. Although not shown for ZnO samples, it is exemplified by the gap in performance between B270 glass substrates pre-treated using an O_2-containing gas mixture (as described in section 3.1.2) and pure Ar gas. Whether this is due to O_2 surface activation (consistent with the paper of Li *et al.*) or superior cleaning of organic residue remains unclear at the time of writing.

Other types of dielectrics were considered as seed layers, namely Si_3N_4 layer produced by sputtering; however non-biased Si_3N_4 layers produced by magnetron sputtering were shown to have high roughness, inhibiting coalescence at low thicknesses. Biased Si_3N_4 layers did not display any particular issues as a seed layer but were not of any particular interest in increasing performance.

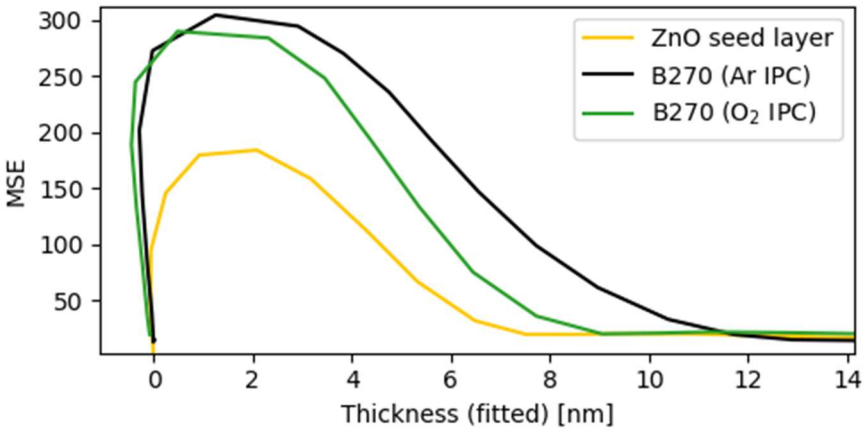

Figure 4.11: Time-reversed fitting of the thickness of continuous Ag layers to *in situ* ellipsometry data demonstrating coalescence behavior for different substrate conditions.

4.1.5 Nitrogen-doped silver films

The different approaches to depositing continuous Ag layers presented so far fail to yield performances equal to the fast-deposited sample presented in Figure 4.5. Indeed, such a high deposition rate is prone to inconsistencies; however as shown in Figure 4.3, a change in deposition rate can dramatically effect the coating's performance.

As a means of bypassing this issue, $Ag_{(N)}$ coatings were tested using N_2 IAD. As mentioned in section 3.1.1, the N_2 supply used in the e-beam evaporation system is not compatible with the automatic gas flow control of the ion source. N_2 flow was therefore set at a fixed rate, with a variable flow of Ar gas to ensure stability of the other parameters. For all samples tested, the discharge current was set to 2 A, with variation of the voltage changing the required gas flow. Gas flows were appropriately chosen so that Ar flow would remain at approximately 20% the value of the N_2 flow. A dozen samples deposited on Orma and B270, containing Ag layers of 6 nm nominal thickness, deposited in configuration C (or with minimal departures from it), were deposited using different Ag deposition rates and N_2 IAD conditions. To evaluate the best IAD conditions and the feasibility of using a lower deposition rate, the average A_V of different deposition conditions were compared, as shown in Table 4.1.

Table 4.1: Mean A_V of coatings using $Ag_{(N)}$ layers produced with different deposition parameters in e-beam evaporation.

Discharge voltage	**N_2 flow rate**	**Nominal dep. rate**	$\overline{A_V}$
[V]	[sccm]	[Å/s]	[%]
200	10	1.3	6.0
200	10	3.1	5.8
100	25	3.1	5.2
100	25	1.3	5.0

In Table 4.1, interesting trends emerge, none the least of which is that all samples tested easily outperform the sample tested in Figure 4.5 (A_V = 8.8%), cementing the value of $Ag_{(N)}$ as a dopant. Perhaps more interestingly, however, is the variation with deposition parameters. For higher voltages, and accordingly, lower amounts of N_2, the usual trend prevails; the higher deposition rate slightly outperforms the lower one; the difference between their performances is much smaller than normally, however, indicating the important effect of N_2 addition. When using a lower accelerating voltage and a higher N_2 flow, the overall performance increases and the relation between deposition rate and A_V is inversed.

The overall increase in performance with lower accelerating voltage would appear to simply be a kinetic issue. This could be interpreted in a number of ways: Marinov reported that IAD can create

depleted zones around clusters, where additional mobility imparts the ability to adatoms to join larger clusters, inhibiting coalescence: for lower energies this could lead to removing some atoms from larger clusters while promoting smaller depleted zones; this would be consistent with Netterfield and Martin, who reported an improvement of coalescence which was specific to low-energy IAD [64], [65]. The improvement reported by Netterfield and Martin was also specific to the usage of O_2 IAD, purporting that such an effect is *not* only kinetic. It has been shown that N atoms are stable in the Ag lattice only when very close to the surface, which promotes their strong float-out behavior. The low deposition rate used here may limit the formation of voids filled with trapped N_2 or otherwise influence the saturation level of the surface with N atoms, which has been shown to change the preferred orientation and surface energy of Ag crystals [90], [91]. Without additional investigation of the nucleation behavior or investigations performed without reactive gases, no definite conclusion can be made.

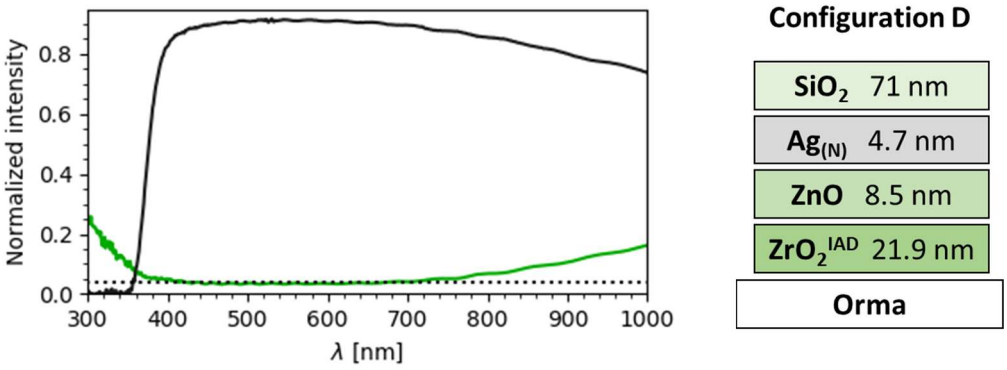

Figure 4.12: Transmittance (black) and reflectance (green) spectra of an AR coating in configuration D, shown on the right. The dotted line is set at 4%, the approximate contribution to the reflection from the backside of a sample. Default layer deposition parameters are found in Table 3.1. Optical properties are found in Table 4.2 and Table 5.1.

Nevertheless, this provides a satisfying method for the deposition of thin $Ag_{(N)}$ films, allowing both well-coalesced thin films and a low deposition rate (more accurate control over the thickness of the film). Using the low discharge voltage and deposition rate, a highly performant AR coating was deposited, with nominal thicknesses, reflectance and transmittance spectra shown in Figure 4.12. The sample is significantly more performant than the sample from Figure 4.5, with R_V = 3.5%, T_V = 91.0%, A_V = 5.5% and R_V^{FS} = 0.25%.

Table 4.2 compares the opto-electronic properties of the most notable AR coating configurations produced with e-beam as part of this project, showing the clear improvement in reflectivity achieved by thinning the Ag layer and in absorption by enhancing Ag quality and continuous film formation; it does not, however, comment on their durability. As will be shown in Table 5.1, the durability of these samples is unacceptable on multiple key points; thus, from this point on, experimental work shifted strongly to magnetron sputtering, with the aim of improving durability while retaining the improvements made to optical performance.

Table 4.2: Opto-electronic properties of notable AR coating configurations produced by e-beam.

Config.	**Ag th.**	**Sheet res.**	$\boldsymbol{\rho}$	$\boldsymbol{R_V^{FS}}$	$\boldsymbol{A_V}$	$\boldsymbol{T_V}$	$\boldsymbol{R_V}$
X : Fig.	**[nm]**	**[Ω/□]**	**[10^{-8} Ω·m]**	**[%]**	**[%]**	**[%]**	**[%]**
A : 4.1	15.0	6.0 ± 1.5	9.0 ± 2.3	1.60	12.7	82.5	4.8
B : 4.1	8	18.5 ± 0.5	14.8 ± 0.4	0.30	8.8	88.0	3.2
D : 4.12	4.7	15.0 ± 1.5	7.1 ± 0.7	0.25	5.5	91.0	3.5

$Ag_{(N)}$ having been extremely useful in the production of well-coalesced, performant Ag coatings, as the need to address coating durability became more pressing and experiments were transferred to the magnetron sputtering system it was imperative to implement its use there as well. To produce $Ag_{(N)}$ coatings by magnetron sputtering, the same deposition conditions were used as for other magnetron-produced Ag coatings (120 W DC, 4 mtorr working pressure), simply substituting the pure Ar working gas for an Ar:N_2 mixture. Figure 4.13 demonstrates the earlier coalescence of films deposited in this way.

It appears from Figure 4.13 that starting from a composition of 25% N_2, at most, the effect of additional N_2 content on coalescence becomes negligible; Zhao *et al*. use lower N_2 partial pressure though approximately the same ratio (≈ 25% of 3 mTorr), suggesting that less than 25% N_2 would be required for the deposition conditions used in this work, although this has not yet been properly explored at the time of writing [89]. Although the precise N_2 percentage values are not the same, this remains in accord with the general trends outlined in the cited literature: Hu *et al.*, who report that grain size decreases quickly with increasing N_2 content up to 10% N_2, followed by a marked stabilization with mostly stable values past 33% [91]. This should be taken with particular

consideration, as Hu *et al.* report these findings for much thicker (> 1 μm) films; following the work of Yun *et al.* as, despite an almost linear decrease in surface energy with increasing N density at the surface, the effect of "buried" N atoms' float-out to the surface is expected increase N density at the surface with increasing thickness, as indicated by the shift in preferred crystalline orientation over the first few nm of growth, meaning that the effect of additional N_2 should be exacerbated in Hu *et al.*'s results [90], [91].

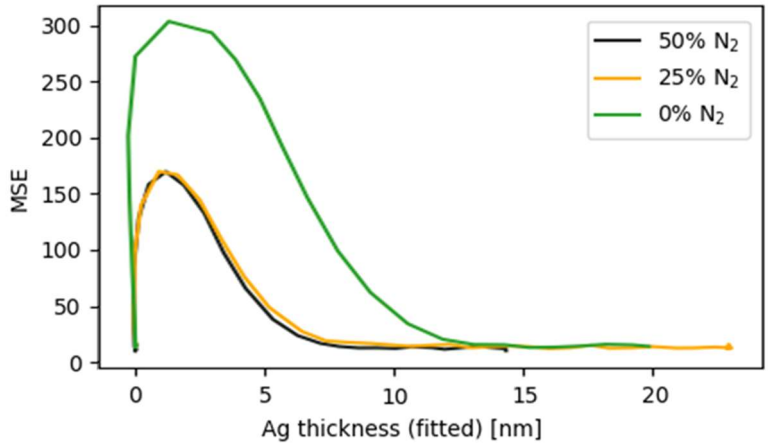

Figure 4.13: Time-reversed fitting of the thickness of continuous $Ag_{(N)}$ layers to *in situ* ellipsometry data demonstrating coalescence behavior for different Ar:N_2 compositions.

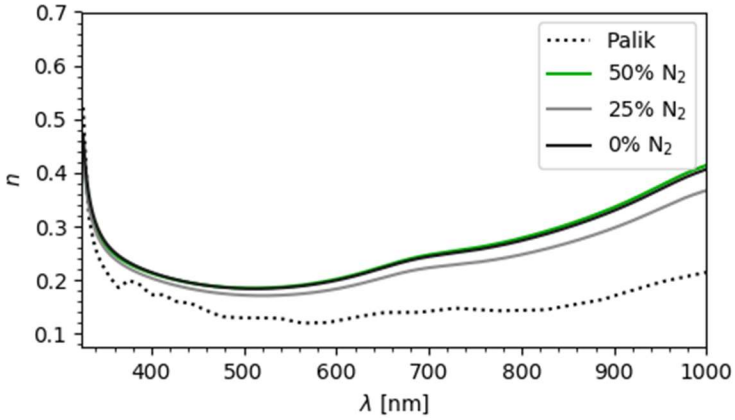

N_2 %	n	k
Palik	0.125	3.34
0%	0.189	3.48
25%	0.173	3.47
50%	0.188	3.44

Figure 4.14: Real refractive index (n) of $Ag_{(N)}$ layers sputtered in different Ar:N_2 compositions, obtained from *in situ* ellipsometry measurements. Given the small changes between the complex refractive index (k) of different layers and the large variation of k over the spectra studied, a table containing values of n and k at 550 nm are appended instead of a second graph.

The reported decrease of grain size is similarly accompanied by an increase in resistivity: as was explained in section 2.1.3, this is expected to lessen the optical properties of the Ag films produced. The optical properties of the layers produced in Figure 4.13 are presented in Figure 4.14. One can see that the refractive indices of measured films are somewhat higher than that of the reference properties by Palik; this is not unexpected, given that these are compiled from multiple different measures, including some using bulk Ag, which are bound to differ from the data obtained with single-angle ellipsometry of much thinner films [125]. That being said, the film produced at 25% N_2 content appears to outperform the other two, with *slightly* lower n, especially at higher wavelengths. This may point to a gas composition at which improved film coalescence improves optical properties, but the reduction of grain size has yet to significantly impact them. At the time of writing this remains a point to investigate and will be addressed in Chapter 5. As initial experiments were already underway with a 50% N_2 composition and no outstanding advantage was found for films deposited with a lower composition at that time, sputtered $Ag_{(N)}$ films continued to be produced using a gas mixture composed of 50% of N_2 for the majority of this work.

4.1.6 Aluminum-doped silver films

Al doping has been reported to increase the durability of Ag films and improve durability; thus, as coating fabrication transferred to magnetron sputtering largely in the name of producing more durable coatings, it should come as no surprise that it was quickly implemented. $Ag_{(Al)}$ films were produced by co-sputtering: as with pure Ag, the working gas was Ar set at a pressure of 4 mTorr. Ag deposition parameters likewise were not changed. Simply, deposition of Al by RF magnetron sputtering was performed alongside Ag deposition, varying the sputtering power to control Al content. Using stylus profilometry, the deposition rate of Al for different sputtering powers was tested: as Ag and Al have the same crystal structure and very similar lattice parameters, their molar density is quite similar, allowing to estimate the atomic percentage composition from their thickness with only minor corrections. It was found in this way that by applying 90 W and 150 W RF sputtering on the Al target, films with approximately 5 and 10 at. % could be produced, respectively. The optical properties of these films are presented in Figure 4.15.

With increasing Al content optical properties deviate from those of Ag, making them increasingly less desirable, as expected based on the work of Zhang *et al.* [86]. The remarkable decrease of the

coalescence threshold induced by the addition of Al, as shown in Figure 4.16, was successfully employed to create relatively performant AR coatings. Namely, a coating using a biased Si_3N_4 seed layer, a 5 nm $Ag_{(Al)}$ layer (produced with 150 W RF Al) and a Si_3N_4 protective layer was created with R_V^{FS} = 1.1% and A_V = 9.3%. Nominal layer thicknesses and coating properties can be found in Figure 5.1, as configuration I, and Table 5.1, respectively. Samples with lower R_V^{FS} were produced with thicker, more continuous $Ag_{(Al)}$ films, albeit these all had higher absorptance, highlighting a balance between plasmon resonance and the effect of doping the Ag layer with a significantly less optically performant metal. Given the shortcomings in their durability, which will be discussed in section 4.2, $Ag_{(Al)}$ layers were not studied at length nor particularly optimized, albeit certain improvements would be easily implementable, such as the use of a ZnO seed layer.

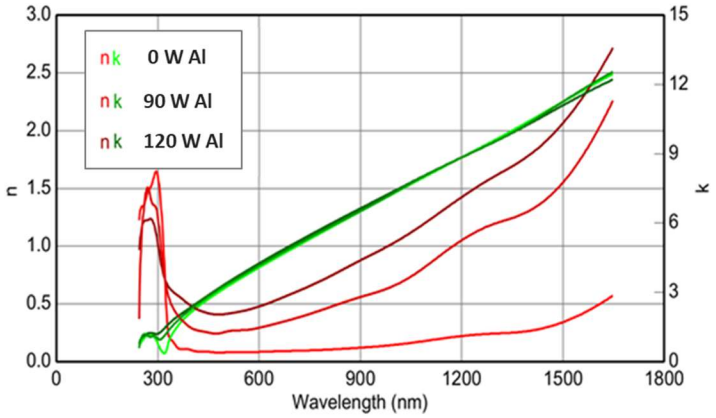

Figure 4.15: Optical properties of $Ag_{(Al)}$ coatings with different Al content obtained by *ex situ* ellipsometry.

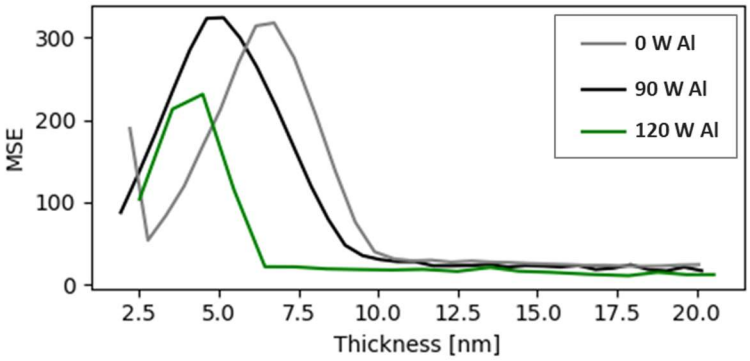

Figure 4.16: Time-reversed fitting of the thickness of continuous $Ag_{(Al)}$ layers to *in situ* ellipsometry data demonstrating coalescence behavior for different levels of Al content.

4.1.7 Metallic seed layers

Similarly to Al doping, Al seed and protective layers were briefly tested, although no important improvement to optical properties or coalescence was found before they were retired due to a lack of durability. Section 4.2.4 details how a certain composition of NiV_x-CrN_x came to be the favored type of metallic seed layer within this work: as such, this section will not concern itself with previous iterations of this seed layer.

It suffices to say that NiV_x-CrN_x layers were deposited by co-sputtering from a NiV target (7 wt. % V) at 150 W DC and from a Cr target at 120 W RF at a working pressure of 4 mTorr in a Ar:N_2 gas mixture composed of 33% of N_2, as detailed in Table 3.2. Figure 4.17 shows the change in coalescence behavior of $Ag_{(N)}$ (deposited in 50% N_2) for different combinations of metallic and dielectric seed layers. All NiV_x-CrN_x layers have a nominal thickness of 0.3 nm; deposition rate was calibrated by deposition of thick layers measured by stylus profilometry.

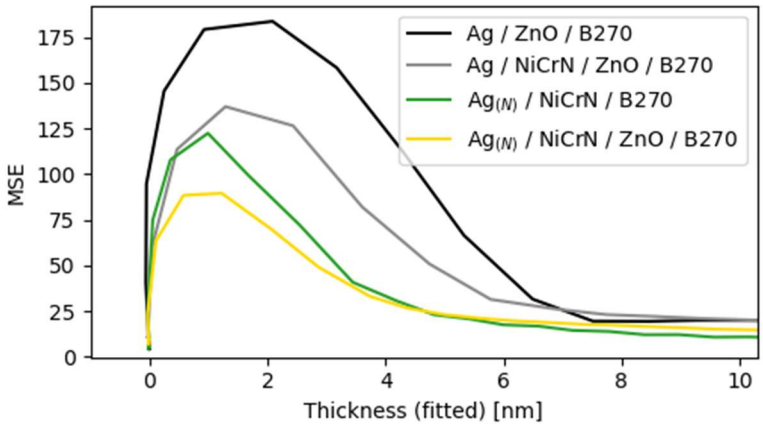

Figure 4.17: Time-reversed fitting of the thickness of continuous $Ag_{(N)}$ layers to *in situ* ellipsometry data demonstrating coalescence behavior for different metal-dielectric seed layer combinations.

It may appear from Figure 4.17 that the addition of ZnO is no longer a meaningful one: with the combination of NiV_x-CrN_x as a metallic seed layer and N as a dopant to promote coalescence, the presence of ZnO does not appear to change the coalescence threshold significantly, allowing its removal from AR coatings. That would be wrong however, as, despite the early coalescence

achieved without ZnO, the metallic seed layer does not improve the optical quality of the Ag layer in a readily observable way.

Figure 4.18 compares the A_V of different samples produced, all with a 0.3 nm thick NiV_x-CrN_x seed layer, as used previously, for different Ag types and thicknesses, with and without ZnO as a dielectric seed layer; it is abundantly clear that, regardless of the continuous film formation threshold , the addition of ZnO is essential to mitigate the absorptance of the metallic AR coatings produced in this work.

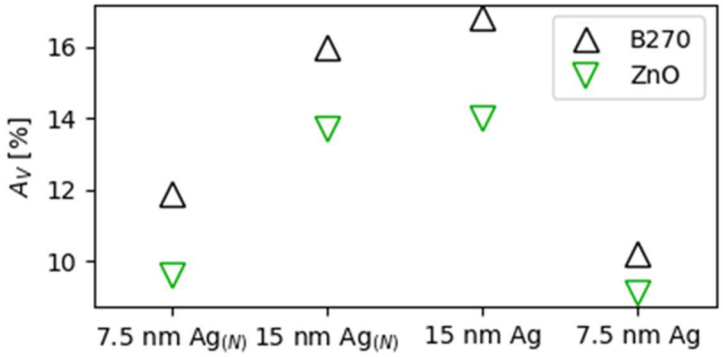

Figure 4.18: A_V of different samples deposited on ZnO coated and B270 dielectric surfaces. Sample configurations are shown in Figure 4.26. Nominal thickness and usage of N doping (50% N_2 sputtering) of the Ag layer is specified for each sample.

Metallic seed layer usage may very well be further optimized, as the coalescence of Ag over discontinuous metal coatings is quite sensitive to the nominal metal thickness, as demonstrated by Anders *et al.* and Fukuda *et al.* [72], [73]. In this respect, the addition of new layers makes the study of coalescence by *in situ* ellipsometry more difficult, particularly in the case of discontinuous metal layers, where the filling of gaps by Ag will make for a heterogenous mixed layer, which may be complicated even further by Ni diffusion into Ag, assuming this occurs on a relatively short timescale.

4.2 Improving silver film durability

4.2.1 Preliminary observations

Initial results were mostly performed with samples fabricated by e-beam evaporation, deposited in configuration A, shown in Figure 4.1, to broadly judge the effect of varying certain parameters, although this section will also include the results of tests on other samples which proved informative enough to be worth mention but not sufficiently so to be included in other sections; as such this section does not only report chronologically preliminary observations, but also those which are important to understand the progression of this chapter. As a reminder, Table 4.3 summarizes tests used.

Table 4.3: Summary of different durability tests used. Full descriptions are found in section 3.3.

Test type	Test conditions
Temperature	Heating in dry gas from 50 to 110 °C, 1 hour at each 10 °C increment
UV radiation	Exposure to solar-equivalent radiation for 200 hours
Mechanical (Nx10B)	N×10 reciprocating swipes of isopropanol-soaked cloth under 12 N load
Humidity	Exposure to ≥ 90% humidity at 60 °C and 80 °C for 2 hours each
Saline corrosion	Immersion in 200 g/L NaCl solution at 50 °C for 20 minutes

The results of temperature testing are highly encouraging, with no degradation observed for tests up to 110 °C, at which point further increase in temperature is expected to damage the Orma substrates (samples on B270 glass substrate were tested without meaningful degradation being observed up to 150 °C). While there is a subjective aspect to this test as cracking needs to be verified by eye, spectrophotometry and resistivity measurements do not change significantly throughout testing, supporting that there is indeed no crack formation, and validating the thermomechanical durability of metal-based AR coatings.

Samples submitted to the UV radiation test show no decrease in performance, which comes as no surprise. Inorganic dielectrics are generally durable to UV radiation; the polymer Orma substrates may be more likely to suffer from UV exposure than the coatings themselves. Although Hwang *et*

al. have reported that UV absorption by Ag nanowires can locally heat and recrystallize atoms at the layer's surface, in their work the protective top layer, which generally inhibits mass transport, is delaminated; it thus seems unlikely that the UV exposure from environmental testing would be sufficient to alter any Ag layer which is well-adhered to both its seed and protective layer [126].

Problems start to emerge with mechanical testing; samples fail the mechanical durability test after only a few series of testing ($N \leq 3$). Worse still, certain samples of other configurations are damaged even by simple handling mistakes. This is expected; the poor adhesion of Ag on glass and other dielectrics has oft been mentioned in this work. Fortunately, as highlighted by Folgner, Ag layer adhesion is firmly correlated to environmental durability, allowing simultaneous pursuit of both improvements [94].

Humidity testing is, in a way, a test in two parts: as Caron points out, it is another thermomechanical durability test, exposing samples to high temperatures this time in high humidity rather than dry gas [12]. Otherwise, in the case of Ag samples, it is a type of corrosion test, wherein airborne contaminants may reach the Ag layer. Initial testing showed that for metal-based AR coatings, degradation is dominated by this second corrosive behaviour, with clearly visible, opaque, whitish-yellow defects appearing during the first iteration at 60 °C, increasing in number and size during the second iteration, as shown in Figure 4.19.

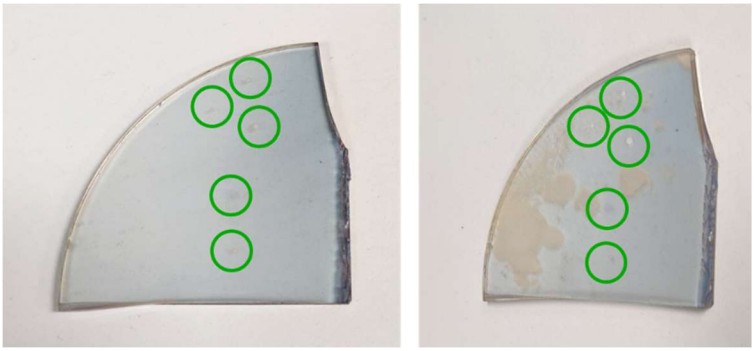

Figure 4.19: Photographs of an AR coating using Ag samples with Al protective layers following humidity testing at 60 °C (left) and 80 °C (right). Initial defect formation (circled in green) is punctual and localized, with much larger swathes of the coating being corroded at 80 °C.

$Ag_{(O)}$ and $Ag_{(Al)}$ both show some improvements in regard to the appearance of corrosion features; samples using an Al interlayer between the Ag layer and protective layer and adding a thick (≈ 150

nm) ZrO_2 layer produced with IAD above the normal protective layer, however, display almost no corrosion features. This suggests that while improving the intrinsic durability of the Ag film helps, isolating the Ag layer from the humid environment may be the better approach. Unfortunately, Al was shown to be vulnerable to Cl corrosion whereas the thick dielectric layer suffers from thermomechanical failure, with clear cracking visible.

As mentioned in section 3.3.5, the initial iteration of saline testing was far too harsh, completely degrading and/or delaminating all samples, without allowing to distinguish a difference in durability between them. Test conditions were changed, with heating removed and NaCl concentration reduced to 0.1 mol/L, to allow a more progressive, observable degradation process. Nominal testing time was left long (17 h) emulating Koike *et al*., with verifications throughout the test allowing to cut it short if the sample was compromised [121]. In this set up, Al doping and protective/seed layers were shown to delay degradation of the Ag layer, though not sufficiently to meet durability expectations, with Al capped films in particular tending to delaminate during corrosion testing.

Once again referring back to section 3.3.5, a new testing set up using *in situ* spectrophotometry to monitor degradation of the Ag layer was designed with the intent of quantifying the degradation process, with the ability to vary severity of the testing by changing the testing temperature as shown in Figure 4.20.

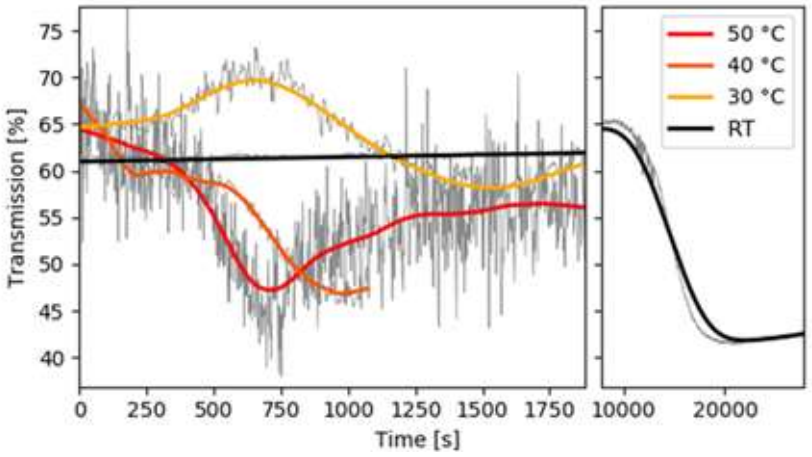

Figure 4.20: : *In situ* transmission data in saline testing performed in a 200 g/L NaCl solution, for varying temperatures, measured at 550.1 nm.

Increasing temperature not only accelerates degradation, it also creates significant noise and large-period signal variations; the former appears to be caused by convection currents agitating the solution, with NaCl concentration gradients interfering with the signal, as removing the heat source or decreasing the NaCl concentration both decrease noise. The cause of large-period signal variations has yet to be confirmed, but is likely of similar origin, as they have only been observed for high temperature testing. To this effect, testing is supplemented with visual inspection to insure that these variations do not cause mistakes during data interpretation.

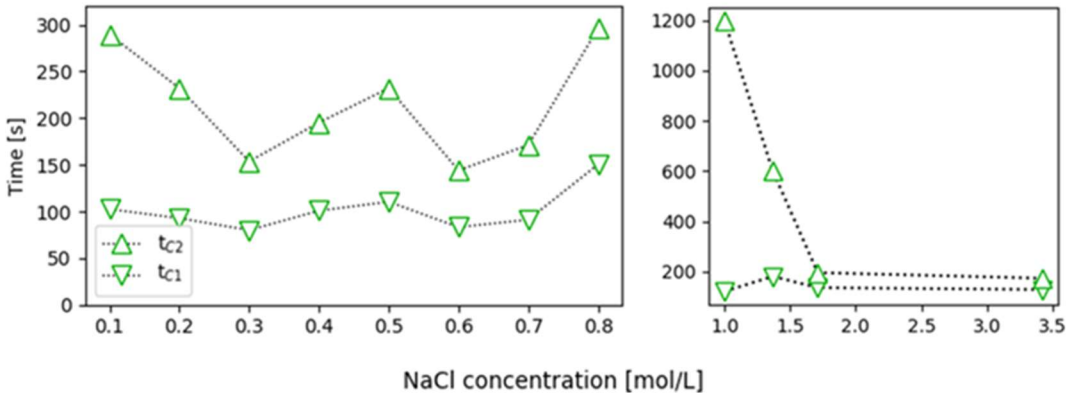

Figure 4.21: Critical degradation times for different concentrations of NaCl at room temperature (left) and at 50 °C (right). Different sample types are used for each temperature.

In attempts to find whether or not test severity could be modulated with concentration rather than temperature, it was found that, at least at low temperatures, concentration does not affect degradation times significantly, leading to the choice of low concentrations for use in decelerated testing (0.1 mol/L ≈ 5.8 g/L, room temperature). Later on, once sample configurations which resisted to benchmark testing (200 g/L, 50 °C) were developed, additional refinement of the design was made difficult due to issues interpreting the noisy, oscillation prone data. Here, the effect of concentration was significant, but only seems to affect t_{C2}, suggesting that increase in temperature is mainly responsible for Cl ions reaching the Ag layer whereas concentration changes the Cl 'load' placed upon it. Although not implemented at the time of writing, improvements allowing clearer durability testing results are proposed in Chapter 5.

To summarize, samples passed temperature and UV testing without any issue and other failed all other tests. However, good stack adhesion has been linked to corrosion durability and failure during

humidity testing seems to be mostly if not entirely a result of Ag corrosion. Given this, as well as the gradual, quantitative durability testing allowed by saline corrosion, the following sections will focus on saline corrosion, following which the mechanical durability of a variety of corrosion-resistant designs will be tested for validation.

4.2.2 Dielectric protective layers

The simplest way to protect Ag from corrosion is to simply isolate it away from corrosive species, by use of a good protective layer, which should be insoluble, impermeable, and non-porous. For a given film material, appropriate substrate cleaning, as described in section 3.1, can limit defects and judicious selection of deposition conditions can help create a film with limited porosity and diffusion paths. More specifically, increasing the effective energy flux and/or substrate temperature can reduce porosity. As high temperatures promote the dewetting of the Ag film, improvement of dielectric protective layers was attempted via kinetic bombardment.

Unfortunately, improvement of Si_3N_4 protective layers by substrate biasing failed outright; all samples prepared with a biased protective layer showed signs of degradation even before testing could be performed, with cracks, highlighted by the localized tarnishing of the Ag layer around them, being observed. This appears to be caused by internal stress of the biased Si_3N_4 layers, consistent with the work by Phillips *et al*. in which unexpectedly poor performance of Si_3N_4 protective layers was linked to high intrinsic stress [97]. However, as Si_3N_4 layers have shown themselves to be of little to no interest as a seed layer, have a high refractive index for a protective layer ($n \approx 2$, higher than what is suggested by modeling approaches), and any process optimization performed on them will be lost upon retransfer to e-beam evaporation, it was not considered to be worthwhile to invest further time into improving their quality as protective layers.

In lieu of this, improvement of SiO_2 protective layers deposited by e-beam was attempted. Using an IAD ZrO_2 seed layer and a 15 nm Ag layer, SiO_2 layers with a nominal thickness of 70 nm were deposited with a discharge current of 2 A and various accelerating voltages. Ar was used as the main gas source; O_2 was added to certain depositions (1 sccm without IAD, 10% O_2 composition with IAD) to gauge the effect of reactive evaporation on SiO_2's protective properties, as shown in Figure 4.22.

One can see that, other than the sample deposited with an accelerating voltage of 100 V, in pure Ar, which is wholly off-trend, sample durability increases with accelerating voltage and decreases with addition of O_2. The improvement with increasing ion energy is not unexpected, though whether the mechanism of improvement is densification of an otherwise porous structure, or otherwise, cannot be determined with these measurements alone. Similarly, there is no obvious, outstanding explanation as to why oxygen addition diminishes the SiO_2 layer's effectiveness as a productive layer. Oxidation of the Ag surface reducing its surface energy may reduce adhesion quality at the top interface, just as excess O_2 may negatively impact the SiO_2 layer's structure [95]. Given the small amount of O_2 used, and that this negative change is also present without the use of IAD, kinetic effects can be ruled out at the very least.

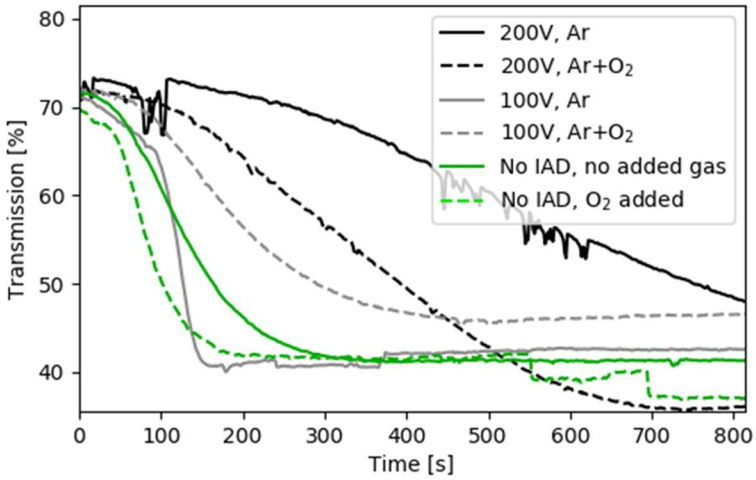

Figure 4.22: : *In situ* transmission data in decelerated saline corrosion testing for evaporated Ag layers, coated with SiO_2 deposited under different IAD conditions, measured at 550.1 nm.

Before any additional investigation is made into this, it would be worthwhile to study the durability of SiO_2 coated stacks in harsher testing conditions, as what is a meaningful change in these conditions is likely to not extend to them, given the poor results observed in humidity testing; other techniques will be required to improve performance.

4.2.3 Doped silver films

Given that $Ag_{(O)}$ layers did not perform particularly well optically or in preliminary durability tests, coupled with the fact that sputtering with an O_2 gas mixture could promote poisoning of the Ag target with O, $Ag_{(O)}$ was not implemented in sputtering and will not be discussed in this section.

Figure 4.23 compares the durability of 'standard' Ag films, $Ag_{(N)}$ films produced in 50% N_2, and $Ag_{(Al)}$ films co-sputtered with Al deposited at 150 W in RF sputtering, each deposited at nominal thicknesses of 7.5 nm and 15 nm, as a means of investigating the effect of thickness and doping on durability, particularly to evaluate if there should be any interest in $Ag_{(Al)}$ films as high durability comes to the forefront of this project. These layers were deposited on B270 glass and capped with a 40 nm Si_3N_4 protective layer, then tested in decelerated testing conditions.

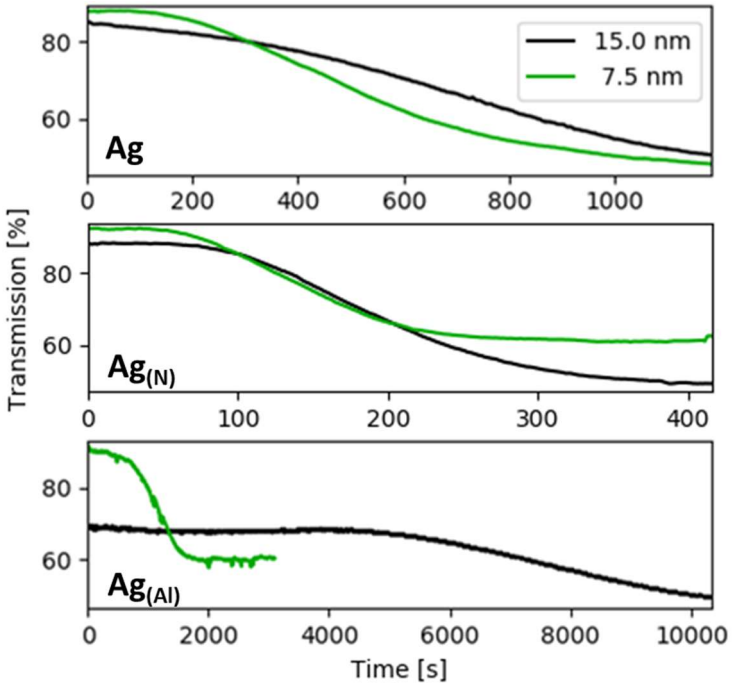

Figure 4.23: *In situ* transmission data in saline testing performed in decelerated testing conditions for sputtered Ag layers deposited with different dopants and coated with Si_3N_4, measured at 550.1 nm.

Noting the different timescales, it is found that $Ag_{(N)}$ is significantly less durable than Ag, which is likely due to a decrease in grain size; this has been linked to accelerated corrosion and increased diffusion paths at grain boundaries [53], [104]. This is consistent with both XRD measurements and with the results reported by Hu *et al*., which show a decrease in grain size for $Ag_{(N)}$ films [91]. No marked relation is found as a variation of thickness, both for Ag and $Ag_{(N)}$, however. Thicker layers appear to degrade at approximately the same rate, though in the case of $Ag_{(N)}$ (and potentially for Ag, had measure duration been longer) these may degrade further before the signal stabilises, which would simply be due to the formation of a thicker layer of Ag-Cl corrosion by-products.

On the other hand, $Ag_{(Al)}$ layers are significantly more durable than Ag layers, and this durability is *highly* dependant on the layer's thickness, unlike Ag. Given that both thicknesses have the same Al composition, it would appear that the total quantity of Al is the key parameter. It has been shown in a number of different contexts that metals can diffuse to reactive sites, Al in particular being used as a dopant or as coating so that it may diffuse to vulnerable sites and form a passivating layer there [102], [107], [109]. This is generally highly effective as Al_2O_3 is a performant protective layer. However, it has been shown that in environments rich in Cl, oxide formation is not as effective; many explanations have been put forward, but the key point is that Cl ions disrupt the formation of effective passivation layers and can diffuse through the bulk of such layers, leading to corrosion [127]. It thus seems likely that an Al_2O_3 layer is formed, but is not sufficiently thick or impermeable to protect the Ag layer in the long term, with thicker $Ag_{(Al)}$ layers having more Al available to protect corrosion sites; this would explain the resistance of Al-doped coatings as a function not necessarily of thickness, but of Al content. This is also consistent with $Ag_{(Al)}$ layers showing high durability in scenarios where they are submitted to oxidation or otherwise form a decent passivation layer unimpeded. Pre-forming a protective oxide layer may present some advantages in corrosion testing, though further experimentation would be required to validate this.

Given that increasing Al content decreases optical quality quickly, and that, even at current compositions, the $Ag_{(Al)}$ layers produced lack durability, it seems unlikely that these would prove useful going forward. On the other hand, whereas $Ag_{(N)}$ has shown itself to be highly useful for promoting continuous film formation, it is now apparent that it introduces additional vulnerability to corrosion. Its usage will have to depend on whether or not this vulnerability can be circumvented by other means.

4.2.4 Metallic protective layers and seed layers

As mentioned in section 4.1.7, NiV_x-CrN_x seed layers used in this work are co-sputtered from NiV (7 wt. % V) and Cr targets. Evaluation of the effect on durability and optical performance of CrN_x layers composition was attempted by evaluating the degradation time and absorbance of coatings composed of 15 nm Ag samples deposited on B270 glass and capped with Si_3N_4 layers of 40 nm nominal thickness; between the Ag and Si_3N_4 layers, Cr was sputtered for a fixed nominal deposition time of 15 seconds, with 200 W DC sputtering at a working pressure of 4 mTorr. The

N_2 composition of the Ar:N_2 working gas was varied to adjust the properties of the CrN_x layer from more metallic (which was shown to provide high durability but to be highly absorbant) to more dielectric (with the opposite response). Saline testing was performed in decelerated testing conditions.

Table 4.4: A_V and t_{C2} (decelerated conditions) of coatings containing Ag layers protected by CrN_x layers produced in an Ar-N_2 working gas with varying amounts of N_2.

Gas composition	A_V	t_{C2}
[N_2 %]	[%]	[s]
20	25.2	≈ 1800
33	18.3	≈ 700
50	17.0	≈ 450

As expected, the addition of N_2 gas during sputtering leads to the formation of less absorbing, less durable films, with films produced in 33% N_2 seeming to yield the best optical properties. However, these changes in performance are not strictly due to a change in chemical composition of the CrN_x layers, as target poisoning affects the deposition rate. Following Berg's model of reactive sputtering, the formation of the desired compound, CrN_x, at the Cr target's surface is expected to have decreased the sputtering deposition rate, with the removal of this compound requiring additional sputtering at lower N_2 partial pressures, causing hysteresis of the deposition rate under varying exposure to the reactive gas [128]. Thus, while it was found that CrN_x coatings offered improved durability and that an increase of N_2 content during sputtering could decrease both this gain in durability and their absorbance, the effect of their thickness as opposed to their composition could not be reliably resolved without further testing. However, experiments quickly showed that CrN_x films alone could not ensure sufficient durability to meet the goals of this project, and rather than optimize them independently, the addition of NiV_x was made a priority.

To limit the effect of dielectric formation on the Cr target and enable NiV_x co-sputtering, CrN_x deposition conditions were changed to 120 W RF magnetron sputtering, again at 4 mTorr with the 33% N_2 composition being retained from previous experiments; ellipsometry measurements indicate very similar optical properties as for DC sputtering under the same conditions, indicating

a similar CrN_x composition. Stylus profilometry was used to calibrate the new deposition rate. N_2 composition and other deposition conditions were kept fixed for CrN_x deposition following this experiment; deposition rate and film properties remained stable.

It is worth noting that encapsulation of the Ag layer in symmetric CrN_x layers, greatly improved sample durability, which is associated to the stabilization and proper adhesion of both interfaces, with t_{C2} increasing all the way to ≈ 20 000 s, while keeping A_V below 24%, an enormous improvement when opposed to results reported in Table 4.4. Despite the remarkable improvement, this configuration is not sufficiently durable and degrades much more quickly when undergoing saline corrosion testing in benchmark conditions; this is the configuration used as a demonstration of accelerated degradation with increasing temperature in Figure 4.20.

Table 4.5: T_V (0° incidence) and t_{C2} of samples using 15 nm of Ag protected by various combinations of metallic layers. All samples are deposited on B270 and capped with Si_3N_4 protective layer with a nominal thickness of 40 nm.

Seed layer		**Protective layer**		T_V	t_{C2}
[Material]	**[nm]**	**[Material]**	**[nm]**	**[%]**	**[s]**
NiV_x-Cr	2.4	NiV_x-Cr	2.4	39.3%	-
NiV_x	2.3	NiV_x	2.3	49.6%	-
NiV_x-CrN_x	2.4	NiV_x-CrN_x	2.4	53.0%	-
NiV_x-CrN_x	0.6	NiV_x-CrN_x	0.3	64.7%	-
CrN_x	1.5	NiV_x-CrN_x	0.6	69.6%	≈ 700
CrN_x	0.5	NiV_x-CrN_x	0.6	72.5%	≈ 700
NiV_x-CrN_x	0.3	NiV_x-CrN_x	0.3	70.4%	-

Therefore, as mentioned previously, NiV_x implementation was made a priority; CrN_x deposition conditions and working gas composition were kept the same as described above, with NiV_x being deposited at 150 W by DC magnetron sputtering. Although no chemical analysis was performed,

based on the corrected deposition rates for each material, validated by stylus profilometry, a broad estimate places metal composition at approximately 80 % Ni, 5% V and 15% Cr; this was found to be sufficiently close to what is used in industry (80% Ni, 20% Cr) that deposited NiV_x-CrN_x should be similarly performant [111]. Once again using B270 glass as a substrate, with a 15 nm Ag layer and a 40 nm Si_3N_4 protective layer, the effect of different combinations of metallic seed and protective layers on the durability and transmittance (measured at normal incidence, exceptionally) of samples was investigated. It should be noted that saline corrosion testing was now performed in benchmark conditions for a duration of 20 minutes (1200 s), following the test standard.

As can be seen in Table 4.5, the addition of Ni is a major improvement as far as durability is concerned; all samples tested having NiV_x in both their seed layer and protective layer underwent the full test duration without showing any degradation which is visible to the naked eye; *ex situ* spectrophotometry measurements, as shown in Figure 4.24, show extremely small variation of optical properties following testing. That being said, one can see that the addition of only a few nm of NiV_x can cause a decrease in visual transmittance of over 20%, and it follows that use of NiV_x should be kept to a minimum. The final sample listed in Table 4.5 attempts a compromise between durability and optical properties; its transmittance and reflectance curves, measured before and after corrosion testing are shown in Figure 4.24 below.

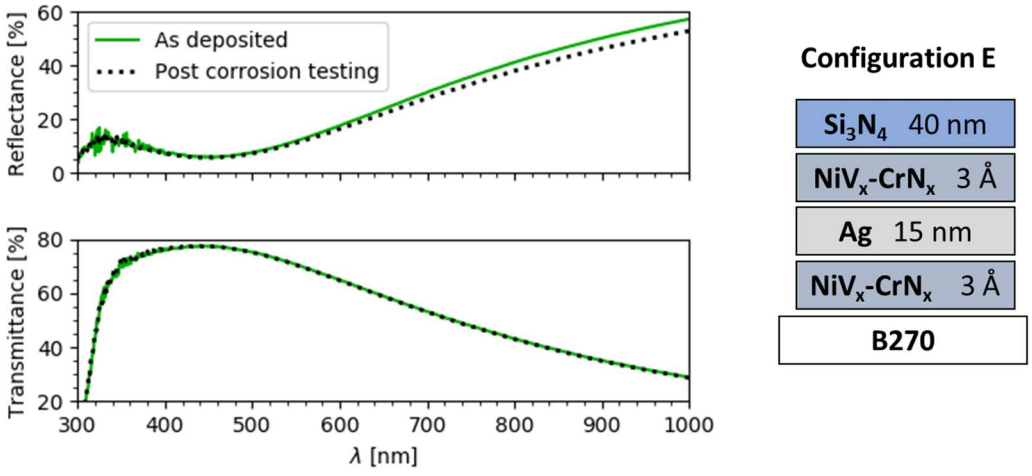

Figure 4.24: Transmittance and reflectance spectra of an AR coating in configuration E (right), before and after 20 minutes of saline corrosion testing in benchmark conditions. Deposition parameters can be found in Table 3.2. Other details can be found in the text

One can see that indeed, following testing, optical properties remain mostly unchanged: T_V merely drops from 70.1% to 70.0%, A_V increases from 17.2% to 18.2% and R_V goes from 12.7% to 11.8%, the latter two of these changes mediated by a shift in the NIR which creeps into the visible spectra. These features can be associated to a loss of conductivity, similarly to thin Ag coatings becoming bluer as plasmonic absorption increases. This is interesting in a practical sense as well, demonstrating that IR monitoring of samples during testing could improve early detection of degradation, which is currently being implemented in an improved corrosion testing system. Moreover, it highlights a difference in protecting Ag layers for low-E glass versus metal AR for ophthalmic applications; the different spectral regions of interest impose different durability requirements.

Attempting to protect the Ag layer with thinner layers of NiV_x-CrN_x to improve transmittance, while a worthwhile pursuit, is one that will eventually introduce durability issues. To maximize the optical gains that can made by reducing the thickness of metallic seed and protection layers, this cut-off point at which they are no longer effective enough must be pushed back by using metal films as effectively as possible.

4.2.5 Improvement of metallic layers

Ironically, what may be the simplest means to strategically use metallic layers to protect Ag coatings has nothing to do with said metallic layers; it is the choice of the dielectric seed layer. ZnO has been shown to be a desirable seed layer insofar as the improvement of Ag coalescence is concerned, which is attributed both to its high surface energy and strong binding with Ag at its O-terminated polar surfaces, which is also expected to lead to improvements in Ag durability, as indicated by the results of Hafezian *et al*. [101].

This has been found to be the case in experiments carried out as a part of this work: in decelerated saline corrosion testing conditions, sputtered Ag coatings of 15 nm nominal thickness, deposited in identical conditions and capped with the same protective layers reached full degradation (t_{C2}) in ≈ 2500 s when deposited on ZnO, rather than in ≈ 700 s when deposited on B270 glass.

Although a notable increase in durability, it is largely insufficient to reach the goals set forward in this work; as has been shown in section 4.2.4, metallic seed layers appear to be necessary to meet

the objectives of this project. That being said, in section 4.1.4 it is shown that ZnO seed layers may still improve the optical properties of Ag films deposited on them despite the presence of a discontinuous metallic seed layer beneath them. Thus, it is of interest to see whether there will be a maintained advantage in durability as well. To that effect, the critical degradation times of samples making use of metallic seed layers both with and without an underlying ZnO seed layer are presented in Figure 4.25; sample configurations are shown in Figure 4.26. It is worth noting that these are the same samples as shown in Figure 4.18.

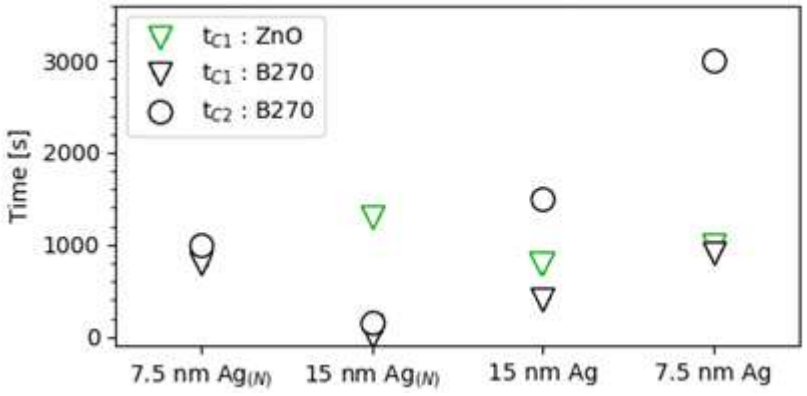

Figure 4.25: Critical degradation times of samples deposited on ZnO and B270 (see Figure 4.26 for sample configurations). Nominal thickness and usage of 50% N_2 sputtering for the Ag layer is specified for each sample. Tests were performed in benchmark conditions for a duration of 1 hour (3600 s). Samples deposited on ZnO did not degrade completely: their durability is compared qualitatively in the text below.

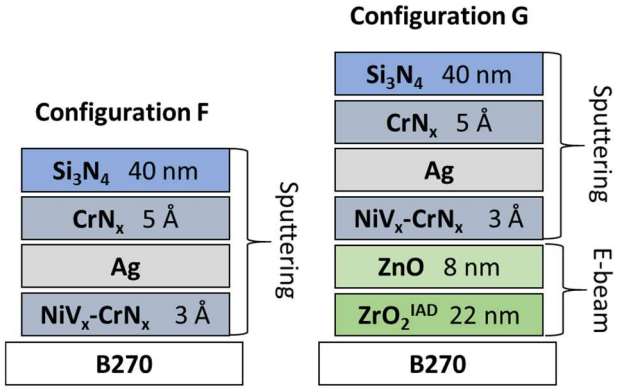

Figure 4.26: Nominal layer configurations F, G, used in Figure 4.25. Default deposition parameters can be found in Table 3.1 and Table 3.2. Other details can be found in the text.

Despite the uncertainty caused by the important amount of noise in high temperature testing and other issues – namely, for the 7.5 nm $Ag_{(N)}$ deposited on ZnO, spectrophotometry data was lost to file corruption – interesting observations can be made, particularly by qualitatively rating the samples after deposition, as done by Phillips *et* al. [97]. In this way, it was found that the aforementioned sample completed testing without suffering total degradation, despite lost data. Although samples tested as part of this work were not systematically photographed, Figure 4.27 presents samples with representative levels of degradation which will be used as a means of comparison. All samples deposited on B270 showed opaque, uniform corrosion, similar to a) or b) in Figure 4.27. Samples deposited on ZnO were clearly degraded, albeit much less so; both 15 nm samples and the 7.5 nm $Ag_{(N)}$ showed non-uniform corrosion akin to c) in Figure 4.27. Most importantly, it was found that the 7.5 nm Ag sample outperformed its counterparts; the sample was simply bluer, as shown by d) in Figure 4.27, indicating a loss of conductivity and an increase in plasmon absorption, although with no haze or corrosion features (with the exception of the strip at the top of the sample, where solution temperatures are slightly higher and corrosion is accelerated).

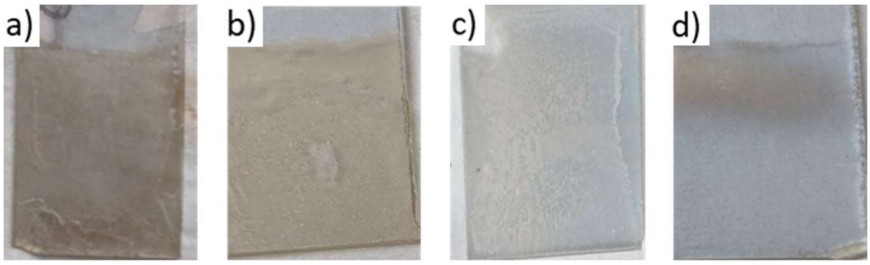

Figure 4.27: Photographs of samples following corrosion testing showing a) Dark uniform corrosion; b) pale uniform corrosion; c) non-uniform corrosion; d) enhanced plasmon resonance (note the much paler blue tone at the top of the image, an un-immersed part of the sample).

Using both this qualitative approach and the quantitative data shown in Figure 4.25 a number of interest trends emerge. Namely, the usage of a ZnO seed layer systematically improves the durability of Ag coatings, even when using metallic seed layers. This is attributed to an increase in grain size, consistent with the higher durability of standard Ag layers sputtered in Ar and the dramatic increase in durability of $Ag_{(N)}$ films which go from degrading completely in a few hundred seconds to not degrading completely over the course of an hour. XRD measurements performed on $Ag_{(N)}$ films with 7.5 nm nominal thickness show an increase of grain size from 9 to 14 nm when deposited on a ZnO substrate rather than on B270 glass; although these measures were performed

without a metallic seed layer, they support the other trends pointed out so far and are consistent with the significant increase in durability found for $Ag_{(N)}$ layers prepared with a ZnO seed layer.

Another interesting trend is that durability decreases at higher thicknesses, regardless of the underlying dielectric. Of course, no such trend was shown in Figure 4.23, suggesting that the increased durability observed for thin samples in Figure 4.25 is not merely due to a difference in Ag thickness itself, but a difference of the thickness *in relation* to the metallic seed layer which is present there, driven by an increase of the quantity of NiV_x-CrN_x relative to that of Ag, or its closer proximity to the front interface, changing the repercussions of Ni diffusion into Ag.

Observing the effect of NiV_x deposition at the upper interface on durability seems to indicate that Ni diffusion dynamics, rather than proximity is driving this change; one can see that (using identical B270 substrates, Si_3N_4 thicknesses, Ag deposition parameters and thicknesses), coatings protected with CrN_x as the seed layer and NiV_x-CrN_x as the top layer degrade in about 700 s (see Table 4.5), whereas those with a significantly thinner NiV_x-CrN_x *seed layer* and a CrN_x *protective layer* degrade in about 1500 s (see Figure 4.25).

In spite of some differences in the configuration used and data collected for each sample, which make a more formal comparison tenuous, the effect observed here is non negligible and could be an important tool in improving Ag durability with minimal NiV_x usage. The root cause of this change requires investigation; asymmetric adhesion at Ag-dielectric interfaces due to the different growth dynamics, as described by Barthel *et al*., may inherently improve durability at the upper interface, sufficiently so that additional protection can be focused at the base [95]. That being said, the diffusion of Ni into the Ag layer, reported by Folgner, is a qualitatively different process which may also change significantly depending on the order of depositions; it stands to reason that during the energetic deposition of Ag films, while these are still discontinuous, enhanced Ni diffusion would be possible, changing its effectiveness as a protective layer [94]. At the moment, though a change in diffusion dynamics seems a likely explanation, no explanations for this behavior can currently be discounted. If further durability testing is conclusive, depth-resolved chemical analysis or observation of the nanostructure, or both, could be used in attempts to ascertain the mechanism by which durability is increased.

The idea that Ag layer durability could so bolstered by an improvement of Ni's diffusion into it is a highly interesting one, which begs the question of what other means would be available to improve Ni diffusion. Wolfe *et al*. show that even at nominal thicknesses higher than those used in this work, $NiCrN_x$ layers form in islands as an admixture, which was credited for the dramatic improvement in adhesion and durability [113]. The formation of this admixture may however limit Ni diffusion into Ag; thus, sequenced deposition of NiV_x and CrN_x was attempted as a means of improving Ag durability, as shown in the right side of Figure 4.28.

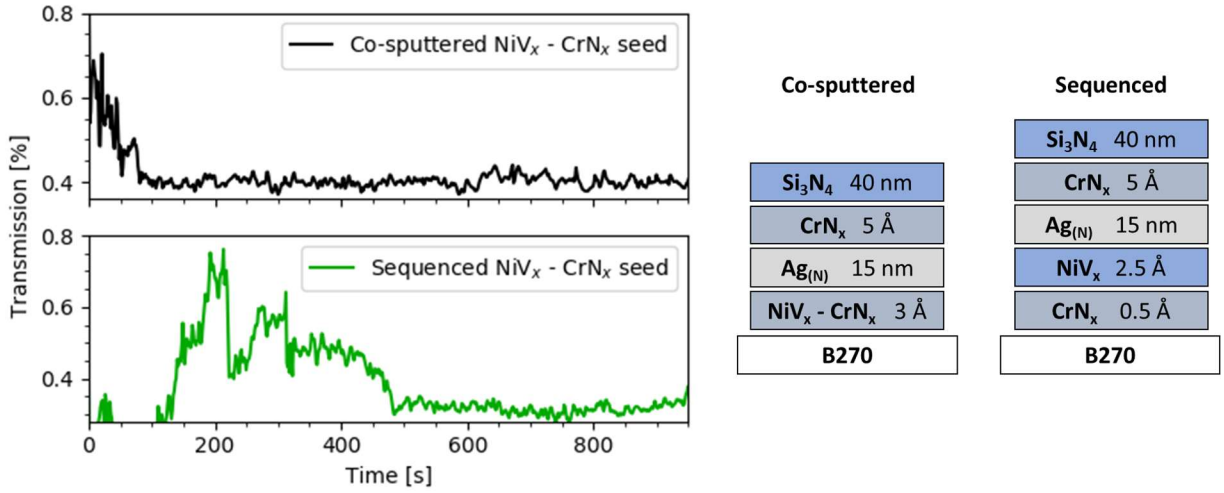

Figure 4.28: *In situ* transmission data in saline testing performed in benchmark conditions for coatings using co-sputtered and sequenced NiV_x-CrN_x seed layers, as shown to the right, measured at 550.1 nm.

Unfortunately, the only sample with this sequenced type of seed layer that could be tested before laboratory shutdown used a 15 nm $Ag_{(N)}$ layer; one will recall from Figure 4.25 that such a Ag layer is extremely susceptible. Thus, the short degradation time is particularly vulnerable to signal noise and fluctuations. Nonetheless, these preliminary results are extremely encouraging, as they seemingly show an increase of approximately 350 s for t_{C2}, which is particularly important given the low degradation times. Of course, additional durability testing will be required to validate this effect, with similar depth-resolved chemical analysis or observation of the nanostructure conditional to it, as suggested previously, though with current information available, outlook is optimistic. Regardless of whether or not this improvement remains as meaningful in other configurations as it is here, as long as it doesn't lower durability it will remain useful as it will

allow more easily controllable deposition of NiCrN type layers by e-beam evaporation. Of course, other solutions are available, but co-deposition from a second e-beam evaporation source would be costly and difficult to implement, whereas evaporation by resistive heating is likely to reduce film purity [114]. Similarly, evaporation from an alloy would require careful calibration given different vapor pressures and different temperature dependencies of these, making sequenced evaporation a clearly more convenient technique.

4.2.6 Mechanical durability

Finally, as a separate matter, the mechanical durability of Ag coatings will be presented. This section has so far been overwhelmingly focused on the durability of Ag to corrosion, which is not inappropriate; high temperature, UV radiation and the thermomechanical aspect of humidity testing have all proved to be no problem to metal AR coatings in the preliminary results. With viable solutions to the problems of Ag growth and corrosion well identified, one simply needs to validate whether these are compatible with mechanical durability. To this effect, an array of samples was deposited, each of them based on a standard design, (labelled configuration H, shown in Figure 4.29) with individual parameter variations allowing evaluation of their effect on mechanical durability testing, as shown in Table 4.6.

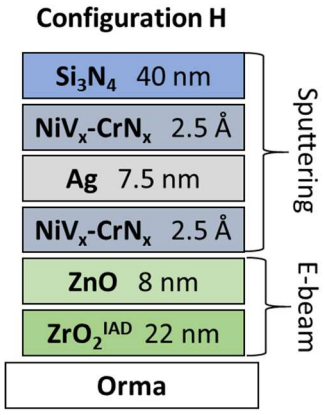

Figure 4.29: Nominal layer configuration H used as the standard stack in Table 4.6. Default deposition parameters can be found in Table 3.1 and Table 3.2. Other details can be found in the text.

Table 4.6: Mechanical durability and opto-electronic properties of various samples based on configuration H shown in Figure 4.29. All samples have a DSX anti-smudge overcoat, as specified in section 3.3.3.

Sample design variation	**Nx10B**	A_V	**Sheet res.**
-	**[Nx10]**	**[%]**	**[Ω/□]**
Standard design	> 20	10.7	19.7 ± 0.5
Ag thickness: 15 nm	> 20	12.6	6.0 ± 0.5
Both NiV_x-CrN_x thicknesses: 1.8 nm	> 20	25.1	21.2 ± 0.5
Both NiV_x-CrN_x replaced by 1.5 nm CrN_x	> 20	24.4	35.5 ± 0.5
Both NiV_x-CrN_x deposited in sequence	> 20	10.7	20.5 ± 0.5
ZnO / ZrO_2 removed	> 20	15.9	27 ± 0.5
ZnO / ZrO_2 replaced with biased Si_3N_4	7	20.1	43.5 ± 0.5
$Ag_{(N)}$ deposited in 50% N_2	1	9.1	16.5 ± 0.5
75 °C NiV_x-CrN_x / Ag dep., etch to 7.5 nm	2	14.8	10.8 ± 0.5

Matters become more interesting upon consideration of the dielectric seed layer. Surprisingly, the removal of the ZnO / ZrO_2 sub-layers, and therefore deposition on a bare Orma substrate, does not seem to affect the mechanical durability negatively. Their replacement by a Si_3N_4 layer, deposited with a 5 W substrate biasing power, on the other hand, significantly decreases film durability, with thin scratch-like delamination appearing as N reaches 7, which grow wider and more obvious with increasing testing duration. In section 4.2.2 it is mentioned that such biased Si_3N_4 films exhibit apparent stress cracking; it therefore seems a logical explanation that stress at the Ag – Si_3N_4 interface is lowering adhesion.

Again, $Ag_{(N)}$ proves itself to be not only susceptible to corrosion, but to delamination as well: immediately after testing begins, at N=1, sections of the coating are scratched off, increasing in size with additional testing, until they coalesce into a large patch at about N=8. Why exactly this

occurs remains to be seen; Yun *et al*. mention that nitrogen can form stable oxides with the oxygen residue from ZnO which *could* decrease adhesion at the ZnO-Ag interface, though it shouldn't affect adhesion from the NiV_x-CrN_x seed, as NiCrN coatings have been used successfully alongside Ag deposited in N_2, with Wolfe *et al*. going so far as to report an improvement of Ag mechanical properties when deposited with N_2 [90], [113]. The particular microstructural evolution of $Ag_{(N)}$ may have an effect which has not been accounted for; Zhang *et al*. explain metals, including Ag, shifting from (111) orientation to (100) under annealing as a strain energy relaxation process [129]. The shift from (111) to (100) observed during growth of $Ag_{(N)}$ layers may be a matter of film stress and not just a shift of surface energy with N density [89], [90].

Finally, the heated-and-etched sample (the fabrication and properties of which is detailed and discussed in the following section) shows a similar pattern of degradation, though its deposition could hardly be more different than that of $Ag_{(N)}$. The annealing of Ag films is commonplace and is not considered to negatively impact adhesion, though deposition at higher temperatures may decrease the contact area at the dielectric interface. Anders *et al*. suggests that the improved wetting brought by discontinuous metallic layers is due to their cluster formation in a kinetically limited 2-D growth mode; at high temperatures, said seed layers may have sufficient mobility to assume a different, less advantageous morphology [72]. Without further information, there is little other to be done other than investigate the poor mechanical durability of both these types of layers.

CHAPTER 5 GENERAL DISCUSSION

As mentioned in the previous section, laboratory shutdowns made it impossible to carry out all the experiments which would have ideally been included in this work, namely the fabrication of a durable, optically performant AR coating drawing from the results of the previous work. Despite having no new experimental data on the subject, however, enough distinct findings and potential means of improvement have been found that they warrant being summarized and discussed in the particular context of fabricating such an AR coating.

Table 5.1: Opto-electronic properties and durability of notable AR coating configurations.

Config.	**Ag th.**	**Sheet res.**	$\boldsymbol{\rho}$	$\boldsymbol{R_V^{FS}}$	$\boldsymbol{A_V}$	$\boldsymbol{T_V}$	$\boldsymbol{R_V}$	**D-code**
X : Fig.	**[nm]**	**[Ω/□]**	**[10^{-8} Ω·m]**	**[%]**	**[%]**	**[%]**	**[%]**	**-**
A : 4.1	15.0	6.0 ± 1.5	9.0 ± 2.3	1.60	12.7	82.5	4.8	C0M0
B : 4.1	8.0	18.5 ± 0.5	14.8 ± 0.4	0.30	8.8	88.0	3.2	C0*M0*
D : 4.12	4.7	15.0 ± 1.5	7.1 ± 0.7	0.25	5.5	91.0	3.5	C0*M0*
I : 5.1	5.0	33 ± 3	16.5 ± 1.5	1.10	9.3	86.0	4.7	C1
E : 4.24	15.0	-	-	-	17.2	70.1	12.7	C2M2*
J : 5.1	7.5	-	-	0.80	10.7	86.0	3.3	C2M0*
H : 4.29	7.5	19.7 ± 0.5	14.7 ± 0.4	-	10.7	85.8	3.5	C2*M2

Table 5.1 presents the opto-electronic properties of some of the most notable AR coatings developed as a part of this work including the film resistivity, ρ, and a quantifier for their durability, "D-code" considers corrosion (C) and mechanical (M) durability and ranks each from 0 to 2, with 0 corresponding to samples which degrade immediately upon testing, 1 to samples which degrade but not immediately and 2 to samples which undergo testing with none or very little degradation. Asterisks indicate that the precise sample mentioned did not undergo the durability test concerned but that its performance can safely be judged from that of similar samples which underwent testing.

Reading through Table 5.1, one sees an evolution of the fabricated samples, starting with the first low-performance, fragile design deposited by e-beam evaporation, with optical properties improving up to the highly performant configuration D. Then, depositions are performed with

magnetron sputtering (occasionally making use of ZnO coated substrates) as focus shifts to depositing more durable samples, and while durable coatings are produced, they are, of course, not as optically performant. This begs the question; how performant can a sample be, while retaining its durability?

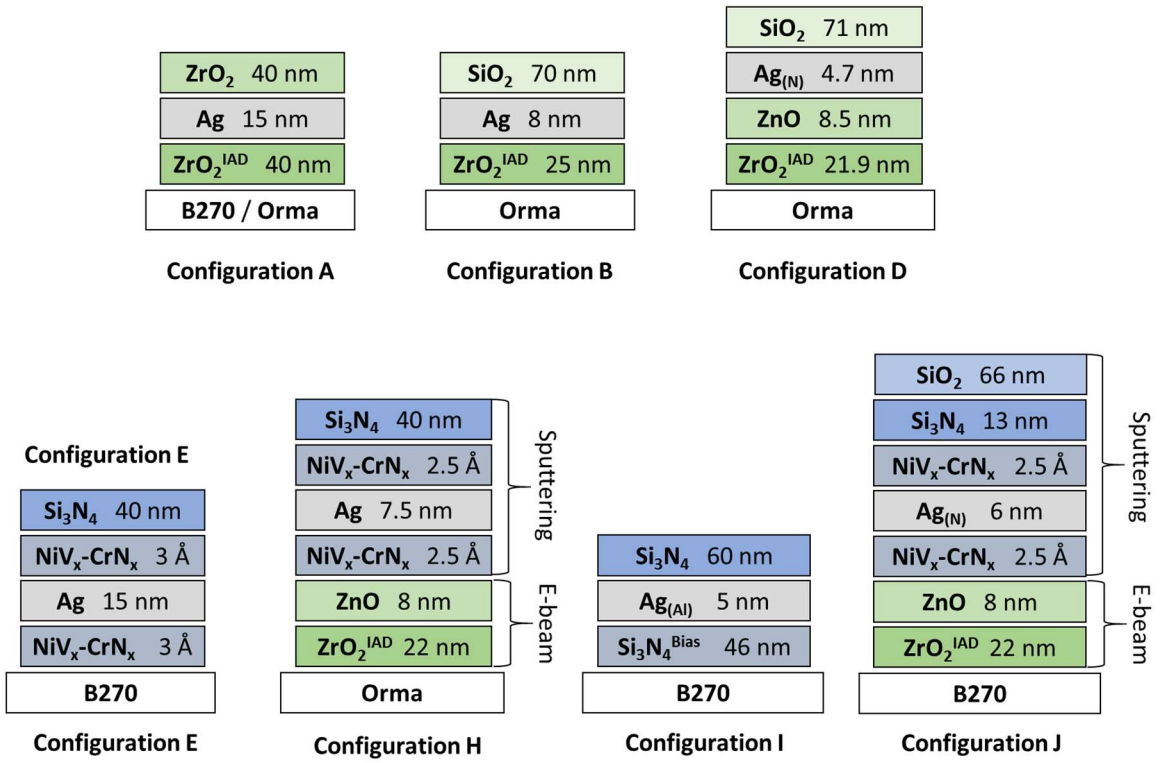

Figure 5.1: Review of nominal layer configurations shown in Table 5.1. Default deposition parameters can be found in Table 3.1 and Table 3.2. Optical properties are found in Table 5.1. Other details can be found in the text.

The sample presented in configuration J shows AR performance which, while unimpressive when compared to configuration D, has R_V^{FS} below 1% and T_V above 85% (it should have $T_V \approx 88\%$, if one discounts the backside reflection), satisfying the project's optical goals, if just barely. It was shown to be durable in corrosion testing, though due to usage of $Ag_{(N)}$, it is expected to have poor adhesion, however. Comparing it to configuration H, which has outstanding mechanical durability and is expected to have even better corrosion resistance, as it does not use an $Ag_{(N)}$ layer, one finds similar optical performance, which suggests that the former is poorly optimized – and that durable samples with improved performance are well within reach.

While modeling suggests extremely low values of R_V are achievable, one should temper their expectations with the information that the models used in this work do not account for roughness, the discontinuity of NiV_x-CrN_x layers, Ni diffusion into Ag (which may decrease its conductivity), thickness dependant Ag properties, and other such issues [44], [113]. Moreover, R_V and A_V could be difficult to reduce simultaneously, as absorption is one of the ways in which a metallic AR can attenuate reflected beams; examples can be seen in Figure 3.3, where the minimum of R_V, while close to, doe not coincide with the maximum of T_V, or in the work of Maniyara *et al*., who succeed in fabricating an ultra-low absorption Ag-containing coating, although it is not a particularly good AR [130]. That being said, it is entirely reasonable to expect that, using a selection of the techniques presented in this work, an AR coating with $R_V < 0.5\ \%$ and $A_V < 10\ \%$, satisfying all of the project's goals, can be produced by e-beam evaporation while maintaining impeccable durability.

Critically, to achieve and surpass this goal, a thin, highly conductive Ag layer is required, as used in configuration D. Repeating the deposition of such a film should not be a difficult matter as long as the implementation of a metallic seed layer doesn't outright obstruct coalescence, as the deposition conditions used were well investigated in section 4.1.5. The matter at hand is whether such a film will be sufficiently durable for use: sputtering experiments showed significantly decreased durability for $Ag_{(N)}$ films, which has been linked to their decreased grain size, with the source of adhesion issues being unclear but potentially linked to film stress. They could potentially be improved simply by using lower amounts of N_2; Hu *et al*. report monotonically decreasing grain size with increasing N_2 content, whereas Figure 4.13 shows that even for significantly lower N_2 concentrations, $Ag_{(N)}$ coalescence remains unaffected [91]. Thus, a simple decrease of N_2 content during $Ag_{(N)}$ deposition may be sufficient to retain the advantages insofar as coalescence is concerned while mitigating durability issues. Although there is no explicit link, this is also consistent with the work of Zhao *et al*., who report using $Ag_{(N)}$ films in highly flexible transparent electrodes, suggesting appropriate durability – to achieve this, they use a lower N_2 ratio and lower pressure, (thus much lower N_2 partial pressure), as well as much lower power density [89]. Again, albeit there is no explicit mention of it in their work, this lower power density likely results in a lower deposition rate, as was used for e-beam evaporation of $Ag_{(N)}$, which seems encouraging. E-beam produced $Ag_{(N)}$ samples should be investigated with XRD and substrate deflection measurements as a means of evaluating the film's crystalline structure and stress, and the effect of

IAD parameters on growth kinetics, which was somewhat overlooked in this work, should be linked to these properties.

It is imperative that the issue of $Ag_{(N)}$ adhesion be resolved; with a ZnO seed layer and appropriate NiV_x-CrN_x usage, the lack of corrosion durability can be addressed, as demonstrated by configuration J, but if films do not adhere properly, even with adhesive layers, the coating will be unacceptable and a different means of obtaining ultra thin, highly conductive films must be introduced. To that end the approach proposed in works such as that of Netterfield and Martin, that is the etching of continuous films, will be presented [65].

This will be studied as the coalescence of films was studied previously, with all steps being performed the same way; however, for the etching of thin films, once the film has been deposited, the substrate is biased to form a plasma at the Ag surface to etch it. *In situ* ellipsometry performed during the etch is used, fitting the thickness through time while going from a continuous to discontinuous film. An example is shown in Figure 5.2: the orange curve overlaying the data was obtained by applying a Savitzky-Golay filter to the data as part of attempts to develop a more rigorous quantification – other figures in this section are likewise produced with such a filter, and while this does not affect broad features, it should be duly noted.

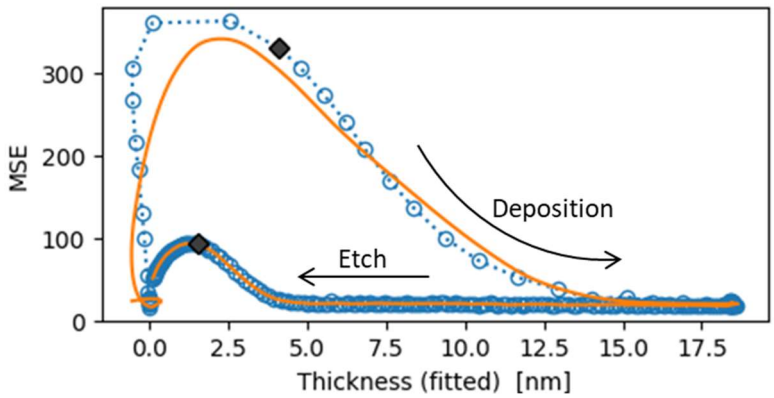

Figure 5.2: Fitting of the thickness of continuous Ag layers to *in situ* ellipsometry data demonstrating (de-)coalescence behavior during deposition and etching with a substrate-bias plasma (4 mTorr Ar, 6 W). Blue: raw data. Orange: data smoothed with Savitzky-Golay filter. Critical times found with Stokes' parameter analysis are identified by black squares.

More importantly, Figure 5.2 shows a dramatic change in the coalescence threshold: an undoped Ag layer deposited with the normal sputtering conditions, on a bare B270 substrate, prepared with an Ar IPC would normally coalesce just above 13 nm or so, as shown in Figure 4.11 and Figure 5.2 – the slightly higher value observed for the latter (≈ 14 nm) is possibly due to a difference in substrate cleanliness or fitting quality. However, using a simple Ar etch (at a pressure of 4 mTorr, using a 6 W substrate bias) the thickness can be reduced to approximately 4 nm before the MSE indicates a loss of continuity. Even so, the relatively low values at which the MSE peaks during etching suggests different or lesser plasmonic effects: this may arise from a different island morphology and/or distribution, consistent with the results reported by Hodgkinson and Lemmon [92].

Figure 5.3 shows the etch results of samples heated during deposition and cooled before etching; although de-coalescence occurs at slightly higher thicknesses than non-heated films, which may be an effect of higher surface roughness, poorer wetting at the interface, or a combination of both, as suggested by Netterfield and Martin [65]. Regardless, this shows that he fabrication of thin Ag films at high temperature becomes possible with the use of etching; this is of interest as heated films are expected to have larger grain sizes, leading to better conductivity and optical properties. The grain size of thin (7.5 nm nominal thickness) $Ag_{(N)}$ films produced in a 50% N_2 gas mixture was estimated at 9 nm based on XRD measurements, whereas heated-and-etched samples of the same thickness produced in pure Ar had an estimated grain size of 16 nm. Of course, one will recall that grain sizes estimated from XRD measurements tend to be higher than reality, but even as a broad indicator, this reveals a potential advantage to the etching of heated films. Moreover, it is shown that $Ag_{(N)}$ remains highly effective in promoting coalescence, even at high temperatures, which may have its advantages.

Unfortunately, as can be seen in Table 4.6, the adhesion of $Ag_{(N)}$ and heated Ag films both pose significant problems. Indeed, the heated-and-etched sample from Table 4.6 shows particularly low sheet resistance, highlighting the potential this method has for creating thin, well-coalesced Ag films. Given the very positive results found without heating or N_2 usage in Figure 5.2, and knowing that this method has been deployed with some degree of success using an ion beam ([65], [92]), suggesting it could be implemented for use with e-beam evaporation, this method remains a potentially useful asset in the event that $Ag_{(N)}$ adhesion issues cannot be resolved efficiently.

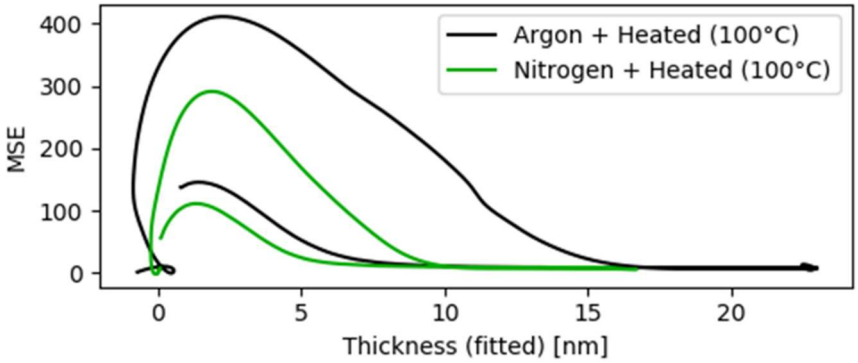

Figure 5.3: Fitting of the thickness of continuous $Ag_{(N)}$ layers to *in situ* ellipsometry data demonstrating (de-)coalescence behavior for samples deposited at 100 °C and etched at room temperature. Data smoothed with Savitzky-Golay filter.

Although it may be difficult given the constraints of Orma substrates, improvement of the ZnO layer should be investigated; it already offers outstanding improvements in durability at no cost to the optical properties, even improving them, which is a set of properties too useful to neglect. As mentioned in section 4.1.4, there appears to be a slight improvement of ZnO quality with appropriate IAD conditions. Following the work of Müller, decreasing the ZnO's deposition rate or increasing the IAD current should help improve crystallinity, but given the absence of meaningful changes observed by XRD and the somewhat more pessimistic assessment of Wu *et al*., this may be rather ambitious [122], [123]. A more realistic approach might be to promote higher efficiency of the ZnO layer by replacing the ZrO_2 sublayer. Deposition on Al_2O_3 substrates has been used to create thin polycrystalline (001) aligned ZnO layers, which promote single crystal Ag growth, as their polycrystallinity reflects the Al_2O_3 structure, which has very low mismatch with Ag [54]. Similar ZnO films have been produced on TiO_2 deposited by e-beam [131]. Despite that these were deposited at high temperature on a crystalline substrate, suggesting that a lesser effect would be achieved, if at all, modeling shows TiO_2 would be an excellent sub-layer to ZnO optically; thus, despite the challenges, this seems like a potential path to improvement which is worth pursuing. It should be noted that samples which underwent temperature durability testing in this work had no adjacent dielectric layers (other than the seed layer and the substrate, of course). If the presence of adjacent dielectric seed layers reduces performance in temperature durability testing, rather than remove the ZrO_2 or TiO_2 sub-layer, it may be better to attempt substituting ZnO by Al-

doped ZnO, which has been shown to be mechanically compliant and resistant to humidity exposure, suggesting good thermomechanical properties overall [132].

Improvement of both the protective layers should be performed, though paths to improvement of the dielectric protection layer are somewhat unclear; IAD deposition of the dielectric protective layers should be further optimized, following the lead laid out in section 4.2.2, but no other interesting methods of improvement have been identified of this time, short of depositing a protective layer by ALD or substituting SiO_2 for a less permeable material. That being said, the low refractive index of SiO_2 is important to AR performance, and it seems best to keep it and simply optimize it as much as possible.

The metallic protective layer should be made as thin as possible; as discussed in section 4.2.4 and exemplified by the results shown in Figure 4.25, its presence is not as critical as that of the metallic seed layer. As sequenced deposition and substitution by CrN_x of the NiV_x-CrN_x layers have been shown to not negatively impact adhesion, the protective layer could be composed strictly of CrN_x or, potentially, CrO_x or CrO_xN_y. CrO_x films are significantly less absorbant than CrN_x and both CrO_x and CrO_xN_y type coatings have shown corrosion resistance and adherence as thick films [133]–[135]. Alternatively, Ni could be substituted with a reactive metal rather than entirely removed; Koike *et al*. suggest that the most effective Ag doping configurations make use of one dopant which inhibits corrosion and one sacrificial doping which limits the effect of eventual corrosion products on Ag [84]. A patent for protected Ag layers in low-E glass touts a similar idea, suggesting that the top of the topmost Ag layer should have some form of doping to increase resistance [83]. Although co-deposition is not an option in this case, Cu has optical properties similar those to Ag, is cited as a potential dopant in both of the aforementioned cases, and has been shown to easily diffuse to reactive sites, making it an ideal choice if implementation of a sacrificial dopant is performed [83], [84], [102], [106].

As a final improvement to the AR coatings designed in this work, the metallic seed layer must be optimized; as for the metallic protective layer, the thickness of Ni used must be minimized to limit absorbance all while ensuring durability is retained. Sequenced film deposition requires further testing to validate the increase of durability it can provide; however, regardless of whether the gain proves to be small or large when incorporated into a sample with higher intrinsic durability, sequencing is of interest as it allows one to substitute CrN_x for CrO_x or CrO_xN_y, which could not

be performed in co-sputtering without excessively oxidising the Ni. Based on the data in Table 5.1, sequencing does not appear to effect Ag growth whatsoever, although substitution of CrN_x or a change in morphology due to the different kinetic limits of the metal seed growth could significantly influence Ag coalescence [72].

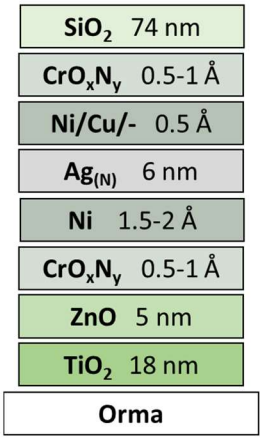

R_V^{FS}	0.03%
T_V	93.1%
A_V	6.9%

Figure 5.4: Nominal layer configuration of an AR design with high durability and optical performance potential (Left). Modeled optical properties (Right). Modeling details can be found in the text.

Assembling all these potential improvements into a single coating, a final, potential configuration is presented in Figure 5.4, complete with approximative optical properties predicted by the *Python* model. In the model used, the coating was composed of a dielectric sublayer with variable thickness and a CRI, a ZnO seed layer of variable thickness, a 6 nm $Ag_{(N)}$ layer (using the optical properties of the 25 % N_2 layer presented in Figure 4.14), and a top protective dielectric with variable thickness and a CRI; as optical properties of potential CrO_xN_y films are not known, a 2.5 Å NiV_x-CrN_x seed layer and a 1.5 Å NiV_x-CrN_x protective layer were used. As the optical properties of CrO_xN_y layers are supposed to be better than those of NiV_x-CrN_x layers deposited in this work, this is considered to be a prudent substitution. The optimal CRI values correspond closely to the reference optical properties of TiO_2 and SiO_2 found in *Complete EASE*. Optimal thicknesses are as presented.

To confidently validate and efficiently implement the techniques presented into such a coating, improved methods to probe the limits of durability and coalescence are required. To this end, improved durability testing methods should be implemented; going forward, qualitatively different

designs should undergo all types of durability testing to identify weaknesses. Once these weaknesses are addressed, testing should be performed once more to ensure no new weaknesses have come up throughout the changing design iterations. More specifically, improvements to temperature resistance testing should be implemented to reduce the test's reliance on the user's ability to notice crack formation by eye. Samples undergoing humidity testing should be carefully cleaned and coated with the hydrophobic DSX coating used in the mechanical adhesion test to limit droplet formation on the sample surface, as pointed out by Schwinde *et al*. [115]. Although droplet formation should not be a durability issue, sample permeability to liquid water is already tested in corrosion testing; with this detail implemented humidity testing should focus on vapor adsorption and its thermomechanical consequences. Last but not least, saline corrosion testing could be improved in the following ways: heating the saline solution in a configuration similar to that of a double boiler, rather than using a heating element may reduce noise and signal fluctuations due to erratic convection currents. Moreover, the usage of an IR source and spectrophotometer to monitor the loss of IR reflectivity of the Ag coating as it loses conductivity, preferably simultaneously performed with monitoring in the visible spectra should help detect the early signs of degradation much more reliably. In the event that these improvements cannot be implemented, intermediate testing conditions at lower temperature and concentration should be used for the purpose of comparing average samples; as shown in Figure 4.20 and Figure 4.21, this should decrease noise and degradation speed, allowing for better data analysis. Benchmark testing can then be reserved for the most durable samples, with *ex situ* spectrophotometry performed over the visible and NIR spectra before and after testing to quantify degradation and compare performances. As of writing, however, the implementation of the previously suggested improvements is underway.

Finally, to most effectively optimise optical performance, using a combination of different approaches to evaluate Ag coalescence would be best. As useful as it is, the approach used in this work is a model-based one, which leaves it susceptible to errors included in the model. Fortunately, Hafezian *et al*. suggest a novel approach in which raw ellipsometric data can be used to detect the early onset of metal cluster coalescence [70]. The mathematical aspect will be left to the original work; it suffices to say that Ψ is converted into the Stokes parameter, S_1, which describes the difference between the reflected intensity of *s* and *p*-polarized light. Hafezian *et al*. stipulate that with changing cluster size, the resonant frequency of plasmonic dipoles shifts and therefore that a

maximum of S_1, which corresponds to a minimum in *p*-polarized reflected intensity, represents a shift in morphology. For higher wavelengths, the times at which S_1 peaks converge to a fixed value, which Hafezian *et al*. have identified as being the percolation threshold using *in situ* conductivity measurements [70]. While this work does not outright endorse the mechanisms suggested, the results are particularly interesting, despite that they identify percolation, and not continuous film formation. Even more interesting is that Monard and Sabary similarly report that discontinuous metal films display resonance which decreases the reflected intensity of *p*-polarized light, but attribute its redshift to metallic islands becoming more oblate; islands coalescing into longer conduction paths at the percolation threshold would there make the S_1 peaks quickly redshift, as observed by Hafezian *et al*. [136]. This is particularly interesting as Zhao *et al*. propose that the non-circularity of clusters may be the defining factor that promotes coalescence – being able to evaluate this from ellipsometry measurements while simultaneously using the model based approach employed in this work could have significant potential [51].

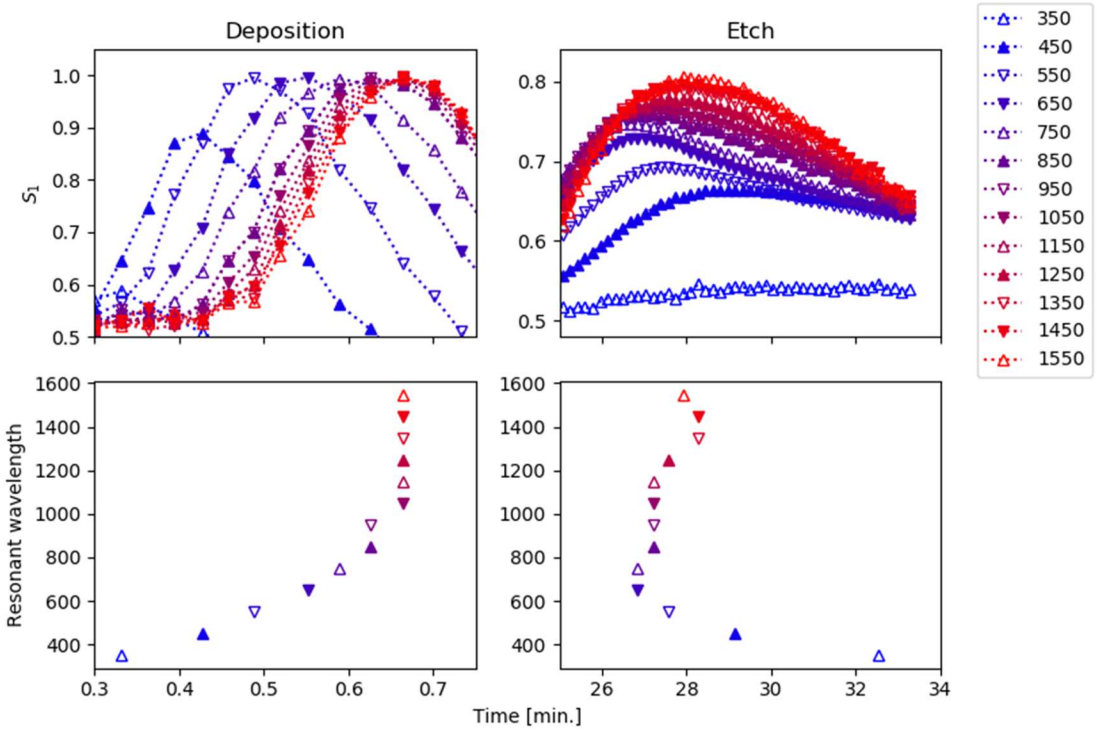

Figure 5.5: S_1 curves for different wavelengths, measured during deposition and etching (Top). Peak positions by resonant wavelength showing expected asymptotic behavior during deposition and novel behavior during etching (Bottom).

As a preliminary test, the proposed analysis by Stokes parameters was employed on the Ag etching data from Figure 5.2, with results shown in Figure 5.5. It is extremely interesting to see that during etching, the pattern of S_1 peaks is not merely reversed but qualitatively different, suggesting a cluster distribution and morphology arising from the etching of a continuous layer which is significantly different, which may be consistent with the observations of Hodgkinson and Lemmon [92]. Using the time from the first peak observed during etching as the "de-percolation" threshold, two critical times were identified, represented in Figure 5.2 as black squares. Of course, further testing would be required to properly assess the interest of this technique, but the interest of having a model-free technique which allows to discern key changes in morphology, and which requires no additional hardware should not be understated.

In addition to this technique, and as a means to better associate its results to island morphology, high resolution imaging or profilometry techniques, such as atomic force microscopy (AFM), transmission electron microscopy (TEM) or field-effect scanning electron microscopy (FE-SEM), should be employed.

CHAPTER 6 CONCLUSION & RECOMMENDATIONS

Throughout the course of this work the techniques and elements relevant to the fabrication of durable, high performance metal-based AR coatings were identified and implemented in a variety of designs, satisfying the general objectives of the work.

Modeling approaches demonstrated that highly antireflective and transparent coatings could be created, contingent on the use of a well-coalesced, ultra thin Ag layer, and using a standard e-beam evaporation system, it was demonstrated that such coatings could be produced with existing industrial systems. From this point, a variety of techniques were employed to engineer the early growth stages of Ag films and improve their coalescence. Concurrently, the durability of these coatings was evaluated, both demonstrating their outstanding resistance to thermomechanical stress and their unacceptable vulnerability to corrosion and delamination.

In situ ellipsometry of sample deposition by magnetron sputtering and a customized corrosion testing bench were used in tandem to evaluate the influence of coalescence promoting techniques on durability and vice-versa. In this way, it was demonstrated that while it is an incredible asset in developing thin, highly conductive Ag films, the small-grained nanostructure promoted by the use of immiscible nitrogen ions as a dopant greatly reduces corrosion durability. Moreover, although no explicit cause has been identified $Ag_{(N)}$ films have shown particularly poor adhesion. Using a ZnO seed layer, however, it was possible to promote larger grains while maintaining improved coalescence, resulting in significantly better optical properties and corrosion durability. Usage of NiV_x and CrN_x seed layers enabled the emulation of NiCrN protective layers commonly used in low-E and telescope mirror applications, greatly increasing durability. It was found that, particularly for very thin Ag layers, Ni-containing seed layers could offer significantly higher durability increases than otherwise, suggesting a different inter-diffusion dynamic. Finally, preliminary data indicates that sequencing rather than co-depositing Ni and CrN_x does not affect adhesion as suggested by the literature and can potentially improve Ag durability.

To achieve the ultimate goal of this project, the fabrication of a durable and highly optically performant metal-based AR coating (with $R_V \leq 0.5\%$, $T_V \geq 90\%$) will require additional work. On the positive side, samples which met those goals without having high durability and samples satisfying the optical requirement ($R_V \leq 1\%$, $T_V \geq 85\%$) and which has high durability were independently produced, all of them well below the maximum thickness of 150 nm. Moreover, a

detailed overview of potential design improvements has been added as a guide to further development of the high-performance, durable AR which this work aimed to create, including materials and process understanding, methodological improvements and information on an alternative etching technique which can be implemented if $Ag_{(N)}$ adhesion issues are not resolved. With the progress achieved in this work, an AR coating configuration which is expected to have high durability, high optical performance and be less than 150 nm thick was designed.

REFERENCES

[1] “Global Optical Coatings Market Size, Share | Industry Report, 2019-2025,” *Grand View Research*. https://www.grandviewresearch.com/industry-analysis/optical-coatings-industry (accessed Mar. 18, 2020).

[2] “Anti-reflective Coatings Market Size | AR Coatings Industry Report, 2025,” *Grand View Research*. https://www.grandviewresearch.com/industry-analysis/anti-reflective-coatings-market (accessed Mar. 20, 2020).

[3] H. K. Raut, V. A. Ganesh, A. S. Nair, and S. Ramakrishna, “Anti-reflective coatings: A critical, in-depth review,” *Energy Environ. Sci.*, vol. 4, no. 10, pp. 3779–3804, Sep. 2011, doi: 10.1039/C1EE01297E.

[4] S. B. Khan, H. Wu, C. Pan, and Z. Zhang, “A Mini Review: Antireflective Coatings Processing Techniques, Applications and Future Perspective,” *Res. Rev. J. Mater. Sci.*, vol. 5, no. 4, pp. 1–19, Oct. 2017, doi: 10.4172/2321-6212.1000192.

[5] D. Meslin, *Materials & Treatments*. Paris, France, 2010.

[6] H. A. Macleod, *Thin-Film Optical Filters, Fifth Edition*. CRC Press, 2017.

[7] D. J. Griffiths, *Introduction to Electrodynamics*, 4th ed. Cambridge University Press, 2017.

[8] M. Keshavarz Hedayati and M. Elbahri, “Antireflective Coatings: Conventional Stacking Layers and Ultrathin Plasmonic Metasurfaces, A Mini-Review,” *Materials*, vol. 9, no. 6, Art. no. 6, Jun. 2016, doi: 10.3390/ma9060497.

[9] K. H. Nielsen, T. Kittel, K. Wondraczek, and L. Wondraczek, “Optical breathing of nano-porous antireflective coatings through adsorption and desorption of water,” *Sci. Rep.*, vol. 4, no. 1, Art. no. 1, Oct. 2014, doi: 10.1038/srep06595.

[10] H. Ishizawa, S. Niisaka, T. Murata, and A. Tanaka, “Preparation of MgF2-SiO2 thin films with a low refractive index by a solgel process,” *Appl. Opt.*, vol. 47, no. 13, pp. C200–C205, May 2008, doi: 10.1364/AO.47.00C200.

[11] G. Womack, P. M. Kaminski, A. Abbas, K. Isbilir, R. Gottschalg, and J. M. Walls, “Performance and durability of broadband antireflection coatings for thin film CdTe solar cells,” *J. Vac. Sci. Technol. A*, vol. 35, no. 2, p. 021201, Jan. 2017, doi: 10.1116/1.4973909.

[12] M. Caron, “Stabilité environnementale des couches minces hybrides organiques/inorganiques sur substrats de plastique,” masters, École Polytechnique de Montréal, 2016.

[13] U. Schulz and R. W. schaffer, “13 - Optical coatings on plastic for antireflection purposes,” in *Optical Thin Films and Coatings*, A. Piegari and F. Flory, Eds. Woodhead Publishing, 2013, pp. 519–539.

[14] F. Cverna, *ASM Ready Reference: Thermal properties of metals*. ASM International, 2002.

[15] S. A. Maier, *Plasmonics: Fundamentals and Applications*. Springer Science & Business Media, 2007.

[16] M. Born and E. Wolf, *Principles of Optics*, 4th ed. Pergamon Press, 1970.

[17] H. A. Macleod, “A New Approach to the Design of Metal-dielectric Thin-film Optical Coatings,” *Opt. Acta Int. J. Opt.*, vol. 25, no. 2, pp. 93–106, Feb. 1978, doi: 10.1080/713819742.

[18] Y. C. Han, M. S. Lim, J. H. Park, and K. C. Choi, “ITO-free flexible organic light-emitting diode using ZnS/Ag/MoO3 anode incorporating a quasi-perfect Ag thin film,” *Org. Electron.*, vol. 14, no. 12, pp. 3437–3443, Dec. 2013, doi: 10.1016/j.orgel.2013.09.014.

[19] P. H. Berning and A. F. Turner, “Induced Transmission in Absorbing Films Applied to Band Pass Filter Design,” *JOSA*, vol. 47, no. 3, pp. 230–239, Mar. 1957, doi: 10.1364/JOSA.47.000230.

[20] P. B. Johnson and R. W. Christy, “Optical Constants of the Noble Metals,” *Phys. Rev. B*, vol. 6, no. 12, pp. 4370–4379, Dec. 1972, doi: 10.1103/PhysRevB.6.4370.

[21] C. Moosbrugger, *ASM Ready Reference: Electrical and Magnetic Properties of Metals*. ASM International, 2000.

[22] J. E. Greene, “Chapter 13 - Nucleation, Film Growth, and Microstructural Evolution,” in *Handbook of Deposition Technologies for Films and Coatings*, 2nd ed., R. F. Bunshah, Ed. Boston: William Andrew Publishing, 1994, pp. 707–765.

[23] P. Ries, D. Mergel, and M. Wuttig, “Silver thin films : improving the efficiency of low-E coatings by employing different seed layers,” 2015.

[24] P. Benjamin and C. Weaver, “The Adhesion of Evaporated Metal Films on Glass,” *Proc. R. Soc. Lond. Ser. Math. Phys. Sci.*, vol. 261, no. 1307, pp. 516–531, 1961.

[25] T. E. Graedel, “Corrosion Mechanisms for Silver Exposed to the Atmosphere,” *J. Electrochem. Soc.*, vol. 139, no. 7, pp. 1963–1970, Jul. 1992, doi: 10.1149/1.2221162.

[26] N. Ohta and A. Robertson, *Colorimetry: Fundamentals and Applications*. John Wiley & Sons, 2006.

[27] T. M. Goodman, T. Bergen, P. Blattner, Y. Ohno, J. Schanda, and T. Uchida, “CIE Technical Note : The Use of Terms and Units in Photometry – Implementation of the CIE System for Mesopic Photometry.” CIE, 2016, Accessed: Apr. 07, 2020. [Online]. Available: http://files.cie.co.at/841_CIE_TN_004-2016.pdf.

[28] “CIE standard illuminants,” *e-ILV | CIE*, 2014. http://eilv.cie.co.at/term/168 (accessed Apr. 28, 2020).

[29] “Colorimetric Illuminants,” *CIE*. http://cie.co.at/publications/colorimetric-illuminants (accessed Apr. 28, 2020).

[30] R. Berns S., *Billmeyer and Saltzman’s Principles of Color Technology, 4th Edition | Wiley*, 4th ed. Wiley, 2019.

[31] A. Macleod, “The Admittance Diagram,” *SVC 2008 Summer Bull.*, 2008, Accessed: May 08, 2020. [Online]. Available: https://www.svc.org/DigitalLibrary/documents/2008_Summer_AMacleod.pdf.

[32] S. Larouche and L. Martinu, "OpenFilters: open-source software for the design, optimization, and synthesis of optical filters," *Appl. Opt.*, vol. 47, no. 13, pp. C219–C230, May 2008, doi: 10.1364/AO.47.00C219.

[33] Z. Knittl, *Optics of Thin Films: An Optical Multilayer Theory*. Wiley, 1976.

[34] M. C. Troparevsky, A. S. Sabau, A. R. Lupini, and Z. Zhang, "Transfer-matrix formalism for the calculation of optical response in multilayer systems: from coherent to incoherent interference," *Opt. Express*, vol. 18, no. 24, pp. 24715–24721, Nov. 2010, doi: 10.1364/OE.18.024715.

[35] J. Piprek, *Handbook of Optoelectronic Device Modeling and Simulation: Lasers, Modulators, Photodetectors, Solar Cells, and Numerical Methods, Vol. 2*. CRC Press, 2017.

[36] F. Abelès, "Recherches sur la propagation des ondes électromagnétiques sinusoïdales dans les milieux stratifiés - Application aux couches minces," *Ann. Phys.*, vol. 12, no. 5, Art. no. 5, 1950, doi: 10.1051/anphys/195012050596.

[37] N. W. Ashcroft and N. D. Mermin, *Solid State Physics*. Holt, Rinehart and Winston, 1976.

[38] A. S. Baburin *et al.*, "Toward a theoretically limited SPP propagation length above two hundred microns on an ultra-smooth silver surface [Invited]," *Opt. Mater. Express*, vol. 8, no. 11, pp. 3254–3261, Nov. 2018, doi: 10.1364/OME.8.003254.

[39] J. L. Hammond, N. Bhalla, S. D. Rafiee, and P. Estrela, "Localized Surface Plasmon Resonance as a Biosensing Platform for Developing Countries," *Biosensors*, vol. 4, no. 2, Art. no. 2, Jun. 2014, doi: 10.3390/bios4020172.

[40] H. Yasuda, R. Matsuno, N. Koito, H. Hosoda, T. Tani, and M. Naya, "Anti-reflective coating for visible light using a silver nanodisc metasurface with a refractive index of less than 1.0," *Appl. Phys. Lett.*, vol. 111, no. 23, p. 231105, Dec. 2017, doi: 10.1063/1.5000531.

[41] O. Hunderi, "Influence of Grain Boundaries and Lattice Defects on the Optical Properties of Some Metals," *Phys. Rev. B*, vol. 7, no. 8, pp. 3419–3429, Apr. 1973, doi: 10.1103/PhysRevB.7.3419.

[42] T. Stefaniuk *et al.*, "Localized plasmon resonances on grains in smooth Ag films," in *2015 17th International Conference on Transparent Optical Networks (ICTON)*, Jul. 2015, pp. 1–4, doi: 10.1109/ICTON.2015.7193633.

[43] I. A. Rodionov *et al.*, "Quantum Engineering of Atomically Smooth Single-Crystalline Silver Films," *Sci. Rep.*, vol. 9, no. 1, pp. 1–9, Aug. 2019, doi: 10.1038/s41598-019-48508-3.

[44] A. F. Mayadas and M. Shatzkes, "Electrical-Resistivity Model for Polycrystalline Films: the Case of Arbitrary Reflection at External Surfaces," *Phys. Rev. B*, vol. 1, no. 4, pp. 1382–1389, Feb. 1970, doi: 10.1103/PhysRevB.1.1382.

[45] Y. Jiang, S. Pillai, and M. A. Green, "Grain boundary effects on the optical constants and Drude relaxation times of silver films," *J. Appl. Phys.*, vol. 120, no. 23, p. 233109, Dec. 2016, doi: 10.1063/1.4972471.

[46] H. Lüth, *Solid Surfaces, Interfaces and Thin Films*, 5th ed. Berlin Heidelberg: Springer-Verlag, 2010.

[47] S. A. Burke, J. M. Topple, and P. Grütter, “Molecular dewetting on insulators,” *J. Phys. Condens. Matter*, vol. 21, no. 42, p. 423101, Sep. 2009, doi: 10.1088/0953-8984/21/42/423101.

[48] L. Vitos, A. V. Ruban, H. L. Skriver, and J. Kollár, “The surface energy of metals,” *Surf. Sci.*, vol. 411, no. 1, pp. 186–202, Aug. 1998, doi: 10.1016/S0039-6028(98)00363-X.

[49] R. C. Sill, “Wulff Relation and the Total Surface Free Energy in the Surface for Equilibrium Crystals,” *Nat. Phys. Sci.*, vol. 231, no. 22, Art. no. 22, May 1971, doi: 10.1038/physci231100a0.

[50] J. E. Greene, “Chapter 12 - Thin Film Nucleation, Growth, and Microstructural Evolution: An Atomic Scale View,” in *Handbook of Deposition Technologies for Films and Coatings (Third Edition)*, P. M. Martin, Ed. Boston: William Andrew Publishing, 2010, pp. 554–620.

[51] G. Zhao *et al.*, “Strategy for improving Ag wetting on oxides: Coalescence dynamics versus nucleation density,” *Appl. Surf. Sci.*, vol. 510, p. 145515, Apr. 2020, doi: 10.1016/j.apsusc.2020.145515.

[52] R. Tran *et al.*, “Surface energies of elemental crystals,” *Sci. Data*, vol. 3, Sep. 2016, doi: 10.1038/sdata.2016.80.

[53] M. Ohring, *The Materials Science of Thin Films*. Academic Press, 1992.

[54] B.-G. Jung *et al.*, “Wafer-scale high-quality Ag thin film using a ZnO buffer layer for plasmonic applications,” *Appl. Surf. Sci.*, vol. 512, p. 145705, May 2020, doi: 10.1016/j.apsusc.2020.145705.

[55] D. L. Williams and T. M. O’Bryon, “Chapter 5 - Cleanliness Verification on Large Surfaces: Instilling Confidence in Contact Angle Techniques,” in *Developments in Surface Contamination and Cleaning*, R. Kohli and K. L. Mittal, Eds. Oxford: William Andrew Publishing, 2013, pp. 163–181.

[56] D. V. Schroeder, *An Introduction to Thermal Physics*. Addison Wesley, 1999.

[57] G. L. Kellogg, “Field ion microscope studies of single-atom surface diffusion and cluster nucleation on metal surfaces,” *Surf. Sci. Rep.*, vol. 21, no. 1, pp. 1–88, Dec. 1994, doi: 10.1016/0167-5729(94)90007-8.

[58] S. Esch, M. Breeman, M. Morgenstern, T. Michely, and G. Comsa, “Nucleation and morphology of homoepitaxial Pt(111)-films grown with ion beam assisted deposition,” *Surf. Sci.*, vol. 365, no. 2, pp. 187–204, Sep. 1996, doi: 10.1016/0039-6028(96)00744-3.

[59] A. Anders, “A structure zone diagram including plasma-based deposition and ion etching,” *Thin Solid Films*, vol. 518, no. 15, pp. 4087–4090, May 2010, doi: 10.1016/j.tsf.2009.10.145.

[60] W. Ensinger, “Low energy ion assist during deposition — an effective tool for controlling thin film microstructure,” *Nucl. Instrum. Methods Phys. Res. Sect. B Beam Interact. Mater. At.*, vol. 127–128, pp. 796–808, May 1997, doi: 10.1016/S0168-583X(97)00010-4.

[61] J.-M. Wen, J. W. Evans, M. C. Bartelt, J. W. Burnett, and P. A. Thiel, “Coarsening Mechanisms in a Metal Film: From Cluster Diffusion to Vacancy Ripening,” *Phys. Rev. Lett.*, vol. 76, no. 4, pp. 652–655, Jan. 1996, doi: 10.1103/PhysRevLett.76.652.

[62] M. Schwartzkopf *et al.*, "Role of Sputter Deposition Rate in Tailoring Nanogranular Gold Structures on Polymer Surfaces," *ACS Appl. Mater. Interfaces*, vol. 9, no. 6, pp. 5629–5637, Feb. 2017, doi: 10.1021/acsami.6b15172.

[63] K. Müller, "Dependence of thin-film microstructure on deposition rate by means of a computer simulation," *J. Appl. Phys.*, vol. 58, no. 7, pp. 2573–2576, Oct. 1985, doi: 10.1063/1.335885.

[64] M. Marinov, "Effect of ion bombardment on the initial stages of thin film growth," *Thin Solid Films*, vol. 46, no. 3, pp. 267–274, Nov. 1977, doi: 10.1016/0040-6090(77)90182-1.

[65] R. P. Netterfield and P. J. Martin, "Nucleation and growth studies of gold films prepared by evaporation and ion-assisted deposition," *Appl. Surf. Sci.*, vol. 25, no. 3, pp. 265–278, Apr. 1986, doi: 10.1016/0169-4332(86)90059-0.

[66] J. Zhang, Y. Zhang, K. Tse, B. Deng, H. Xu, and J. Zhu, "Surface energy calculations from Zinc blende (111)/(-1-1-1) to Wurtzite (0001)/(000-1):a study of ZnO and GaN," *J. Appl. Phys.*, vol. 119, no. 20, p. 205302, May 2016, doi: 10.1063/1.4952395.

[67] D. Cornil, H. Wiame, B. Lecomte, J. Cornil, and D. Beljonne, "Which Oxide for Low-Emissivity Glasses? First-Principles Modeling of Silver Adhesion," *ACS Appl. Mater. Interfaces*, vol. 9, no. 21, pp. 18346–18354, May 2017, doi: 10.1021/acsami.7b03269.

[68] P. Li *et al.*, "Structural Optimization of Oxide/Metal/Oxide Transparent Conductors for High-Performance Low-Emissivity Heaters," *Adv. Mater. Interfaces*, vol. 5, no. 24, p. 1801287, Dec. 2018, doi: 10.1002/admi.201801287.

[69] A. Christensen and E. A. Carter, "First-principles study of the surfaces of zirconia," *Phys. Rev. B*, vol. 58, no. 12, pp. 8050–8064, Sep. 1998, doi: 10.1103/PhysRevB.58.8050.

[70] S. Hafezian, B. Baloukas, and L. Martinu, "Percolation threshold determination of sputtered silver films using Stokes parameters and in situ conductance measurements," *Appl. Opt.*, vol. 53, no. 24, p. 5367, Aug. 2014, doi: 10.1364/AO.53.005367.

[71] C. T. Campbell, "Ultrathin metal films and particles on oxide surfaces: structural, electronic and chemisorptive properties," *Surf. Sci. Rep.*, vol. 27, no. 1, pp. 1–111, Jan. 1997, doi: 10.1016/S0167-5729(96)00011-8.

[72] A. Anders, E. Byon, D.-H. Kim, K. Fukuda, and S. H. N. Lim, "Smoothing of ultrathin silver films by transition metal seeding," *Solid State Commun.*, vol. 140, no. 5, pp. 225–229, Nov. 2006, doi: 10.1016/j.ssc.2006.08.027.

[73] K. Fukuda, S. H. N. Lim, and A. Anders, "Coalescence of magnetron-sputtered silver islands affected by transition metal seeding (Ni, Cr, Nb, Zr, Mo, W, Ta) and other parameters," *Thin Solid Films*, vol. 516, no. 14, pp. 4546–4552, May 2008, doi: 10.1016/j.tsf.2007.05.080.

[74] N. A. Sonmez, M. Donmez, B. Comert, and S. Ozcelik, "Ag/M-seed/AZO/glass structures for low-E glass: Effects of metal seeds," *Int. J. Appl. Glass Sci.*, vol. 9, no. 3, pp. 383–391, 2018, doi: 10.1111/ijag.12331.

[75] Logeeswaran VJ *et al.*, "Ultrasmooth Silver Thin Films Deposited with a Germanium Nucleation Layer," *Nano Lett.*, vol. 9, no. 1, pp. 178–182, Jan. 2009, doi: 10.1021/nl8027476.

[76] W. Chen, M. D. Thoreson, S. Ishii, A. V. Kildishev, and V. M. Shalaev, "Ultra-thin ultra-smooth and low-loss silver films on a germanium wetting layer," *Opt. Express*, vol. 18, no. 5, pp. 5124–5134, Mar. 2010, doi: 10.1364/OE.18.005124.

[77] H. Liu *et al.*, "Enhanced Surface Plasmon Resonance on a Smooth Silver Film with a Seed Growth Layer," *ACS Nano*, vol. 4, no. 6, pp. 3139–3146, Jun. 2010, doi: 10.1021/nn100466p.

[78] S. Sonoda, T. Yoshihiro, K. Umeda, Y. Itai, and S. Nakamura, "Optical Thin Film, Optical Element, Optical System, and Method for Producing Optical Thin Film," 20200033508, Jan. 30, 2020.

[79] G. Zhao *et al.*, "Ultrathin Silver Film Electrodes with Ultralow Optical and Electrical Losses for Flexible Organic Photovoltaics," *ACS Appl. Mater. Interfaces*, vol. 10, no. 32, pp. 27510–27520, Aug. 2018, doi: 10.1021/acsami.8b08578.

[80] Y. Liu, C.-F. Guo, S. Huang, T. Sun, Y. Wang, and Z. Ren, "A new method for fabricating ultrathin metal films as scratch-resistant flexible transparent electrodes," *J. Materiomics*, vol. 1, no. 1, pp. 52–59, Mar. 2015, doi: 10.1016/j.jmat.2015.03.005.

[81] W. Wang *et al.*, "Transparent Ultrathin Oxygen-Doped Silver Electrodes for Flexible Organic Solar Cells," *Adv. Funct. Mater.*, vol. 24, no. 11, pp. 1551–1561, Mar. 2014, doi: 10.1002/adfm.201301359.

[82] D. Gu, C. Zhang, Y.-K. Wu, and L. J. Guo, "Ultrasmooth and Thermally Stable Silver-Based Thin Films with Subnanometer Roughness by Aluminum Doping," *ACS Nano*, vol. 8, no. 10, pp. 10343–10351, Oct. 2014, doi: 10.1021/nn503577c.

[83] Y. Lu *et al.*, "Coated article with low-e coating having protective doped silver layer for protecting silver based ir reflecting layer(s), and method of making same," US20190203340A1, Jul. 04, 2019.

[84] K. Koike, K. Shimada, and S. Fukuda, "Aggregation in thin-film silver: Induced by chlorine and inhibited by alloying with two dopants," *Corros. Sci.*, vol. 51, no. 11, pp. 2557–2564, Nov. 2009, doi: 10.1016/j.corsci.2009.06.044.

[85] C. Loka and K.-S. Lee, "Preparation of TiO2/Ag/TiO2 (TAT) multilayer films with optical and electrical properties enhanced by using Cr-added Ag film," *Appl. Surf. Sci.*, vol. 415, pp. 35–42, Sep. 2017, doi: 10.1016/j.apsusc.2016.11.082.

[86] C. Zhang *et al.*, "High-Performance Doped Silver Films: Overcoming Fundamental Material Limits for Nanophotonic Applications," *Adv. Mater.*, vol. 29, no. 19, p. 1605177, May 2017, doi: 10.1002/adma.201605177.

[87] C. Zhang *et al.*, "An Ultrathin, Smooth, and Low-Loss Al-Doped Ag Film and Its Application as a Transparent Electrode in Organic Photovoltaics," *Adv. Mater.*, vol. 26, no. 32, pp. 5696–5701, Aug. 2014, doi: 10.1002/adma.201306091.

[88] C. Weaver and L. C. Brown, "Diffusion in evaporated films of silver–aluminium," *Philos. Mag. J. Theor. Exp. Appl. Phys.*, vol. 17, no. 149, pp. 881–897, May 1968, doi: 10.1080/14786436808223171.

[89] G. Zhao *et al.*, “Nitrogen-Mediated Growth of Silver Nanocrystals to Form UltraThin, High-Purity Silver-Film Electrodes with Broad band Transparency for Solar Cells,” *ACS Appl. Mater. Interfaces*, vol. 10, no. 47, pp. 40901–40910, Nov. 2018, doi: 10.1021/acsami.8b13377.

[90] J. Yun *et al.*, “An unexpected surfactant role of immiscible nitrogen in the structural development of silver nanoparticles: an experimental and numerical investigation,” *Nanoscale*, vol. 12, no. 3, pp. 1749–1758, Jan. 2020, doi: 10.1039/C9NR08076G.

[91] Y. Hu *et al.*, “Understanding the Preferred Crystal Orientation of Sputtered Silver in Ar/N2 Atmosphere: A Microstructure Investigation,” *Advances in Materials Science and Engineering*, 2019. https://www.hindawi.com/journals/amse/2019/3079393/ (accessed Feb. 17, 2020).

[92] I. J. Hodgkinson and J. Lemmon, “Morphology of gold films thinned by argon ion sputter etching,” *J. Appl. Phys.*, vol. 67, no. 11, pp. 6876–6881, Jun. 1990, doi: 10.1063/1.345078.

[93] E. J. Puik, M. J. van der Wiel, H. Zeijlemaker, and J. Verhoeven, “Ion etching of thin W layers: enhanced reflectivity of W-C multilayer coatings,” *Appl. Surf. Sci.*, vol. 47, no. 1, pp. 63–76, Jan. 1991, doi: 10.1016/0169-4332(91)90103-Q.

[94] K. A. Folgner, “Towards Understanding the Environmental Durability and Corrosion Behavior of Protected Silver Mirrors,” Ph.D., University of California, Los Angeles, United States -- California, 2019.

[95] E. Barthel, O. Kerjan, P. Nael, and N. Nadaud, “Asymmetric silver to oxide adhesion in multilayers deposited on glass by sputtering,” *Thin Solid Films*, vol. 473, no. 2, pp. 272–277, Feb. 2005, doi: 10.1016/j.tsf.2004.08.017.

[96] M. Boccas, T. Vucina, C. Araya, E. Vera, and C. Ahhee, “Coating the 8-m Gemini telescopes with protected silver,” USA, Sep. 2004, p. 239, doi: 10.1117/12.548809.

[97] A. C. Phillips *et al.*, “Update on UCO’s advanced coating lab development of silver-based mirror coatings,” in *Advances in Optical and Mechanical Technologies for Telescopes and Instrumentation II*, Aug. 2016, vol. 9912, p. 99122G, doi: 10.1117/12.2233009.

[98] N. Tadokoro *et al.*, “Investigation of shrinkage and cracking of ophthalmic lens coating by a cycle test of UV radiation and high humidity,” *Thin Solid Films*, vol. 520, no. 12, pp. 4169–4173, Apr. 2012, doi: 10.1016/j.tsf.2011.04.097.

[99] E. H. Hirsch, “Stress in porous thin films through absorption of polar molecules (and relevance to optical coatings),” *J. Phys. Appl. Phys.*, vol. 13, no. 11, pp. 2081–2094, Nov. 1980, doi: 10.1088/0022-3727/13/11/018.

[100] Y. Yin, R. M. Rioux, C. K. Erdonmez, S. Hughes, G. A. Somorjai, and A. P. Alivisatos, “Formation of Hollow Nanocrystals Through the Nanoscale Kirkendall Effect,” *Science*, vol. 304, no. 5671, pp. 711–714, Apr. 2004, doi: 10.1126/science.1096566.

[101] S. Hafezian, R. Beaini, L. Martinu, and S. Kéna-Cohen, “Degradation mechanism of protected ultrathin silver films and the effect of the seed layer,” *Appl. Surf. Sci.*, vol. 484, pp. 335–340, Aug. 2019, doi: 10.1016/j.apsusc.2019.04.043.

[102] P. Bellchambers, J. Lee, S. Varagnolo, H. Amari, M. Walker, and R. A. Hatton, "Elucidating the Exceptional Passivation Effect of 0.8 nm Evaporated Aluminium on Transparent Copper Films," *Front. Mater.*, vol. 5, 2018, doi: 10.3389/fmats.2018.00071.

[103] H. Aboulfadl, I. Gallino, R. Busch, and F. Mücklich, "Atomic scale analysis of phase formation and diffusion kinetics in Ag/Al multilayer thin films," *J. Appl. Phys.*, vol. 120, no. 19, p. 195306, Nov. 2016, doi: 10.1063/1.4968013.

[104] N. Perez, *Electrochemistry and Corrosion Science*. Springer, 2016.

[105] P. D. Fuqua and J. D. Barrie, "Optical Properties and Corrosion Resistance of Durable Silver Coatings," *MRS Online Proc. Libr. Arch.*, vol. 555, 1999, doi: 10.1557/PROC-555-85.

[106] D.-Y. Song, R. W. Sprague, H. A. Macleod, and M. R. Jacobson, "Progress in the development of a durable silver-based high-reflectance coating for astronomical telescopes," *Appl. Opt.*, vol. 24, no. 8, pp. 1164–1170, Apr. 1985, doi: 10.1364/AO.24.001164.

[107] Y. Sasaki, M. Kawamura, T. Kiba, Y. Abe, K. H. Kim, and H. Murotani, "Improved durability of Ag thin films under high humidity environment by deposition of surface Al nanolayer," *Appl. Surf. Sci.*, vol. 506, p. 144929, Mar. 2020, doi: 10.1016/j.apsusc.2019.144929.

[108] A. C. Phillips *et al.*, "Progress toward high-performance reflective and anti-reflection coatings for astronomical optics," in *Advanced Optical and Mechanical Technologies in Telescopes and Instrumentation*, Jul. 2008, vol. 7018, p. 70185A, doi: 10.1117/12.789862.

[109] C. A. Barrios, A. V. Malkovskiy, A. M. Kisliuk, A. P. Sokolov, and M. D. Foster, "Highly Stable, Protected Plasmonic Nanostructures for Tip Enhanced Raman Spectroscopy," *J. Phys. Chem. C*, vol. 113, no. 19, pp. 8158–8161, May 2009, doi: 10.1021/jp8098126.

[110] S. Schwinde *et al.*, "Protected silver coatings for reflectors," *CEAS Space J.*, vol. 11, no. 4, pp. 579–587, Dec. 2019, doi: 10.1007/s12567-019-00257-9.

[111] K. W. Hartig and P. J. Lingle, "High performance, durable, low-E glass," US5344718A, Sep. 06, 1994.

[112] X. Xu, B. Li, W. He, C. Wang, and M. Wei, "NiCrNx interlayer thickness dependence of spectral performance and environmental durability of protected-silver mirrors," *Opt. Eng.*, vol. 57, no. 4, p. 045101, Apr. 2018, doi: 10.1117/1.OE.57.4.045101.

[113] J. D. Wolfe, R. E. Laird, C. K. Carniglia, J. P. Lehan, and O. S. of America, "Durable silver-based antireflection coatings and enhanced mirrors," in *Optical interference coatings: summaries of the papers presented at the topical meeting: June 5-9, 1995, Tuscon, Arizona*, Postconference ed., Washington, DC: Optical Society of America, 1995, pp. 115–117.

[114] A. S. Baburin, A. M. Merzlikin, A. V. Baryshev, I. A. Ryzhikov, Y. V. Panfilov, and I. A. Rodionov, "Silver-based plasmonics: golden material platform and application challenges [Invited]," *Opt. Mater. Express*, vol. 9, no. 2, pp. 611–642, Feb. 2019, doi: 10.1364/OME.9.000611.

[115] S. Schwinde, M. Schürmann, N. Kaiser, and A. Tünnermann, "Protected and enhanced silver for mirrors: damage mechanisms and how to prevent them," in *Optical Systems Design 2015: Advances in Optical Thin Films V*, Sep. 2015, vol. 9627, p. 96271R, doi: 10.1117/12.2191216.

[116] “Cleaning Mechanisms,” *co2clean*. https://www.co2clean.com/cleaning-mechanisms (accessed Jun. 25, 2020).

[117] “What is an end hall gridless ion source?” http://www.ionbeam.co.uk/what_is_an_end_hall_gridless_ion_source.php (accessed Jun. 26, 2020).

[118] R. A. Synowicki, “Suppression of backside reflections from transparent substrates,” *Phys. Status Solidi C*, vol. 5, no. 5, pp. 1085–1088, May 2008, doi: 10.1002/pssc.200777873.

[119] R. H. Muller, “Definitions and conventions in ellipsometry,” *Surf. Sci.*, vol. 16, pp. 14–33, Aug. 1969, doi: 10.1016/0039-6028(69)90003-X.

[120] J. N. Hilfiker, R. A. Synowicki, and H. G. Tompkins, “Spectroscopic ellipsometry methods for thin absorbing coatings,” presented at the Society of Vacuum Coaters Tech Con, Chicago, IL, 2008.

[121] K. Koike, F. Yamazaki, T. Okamura, and S. Fukuda, “Improvement of corrosion resistance of transparent conductive multilayer coating consisting of silver layers and transparent metal oxide layers,” *J. Vac. Sci. Technol. Vac. Surf. Films*, vol. 25, no. 3, pp. 527–531, May 2007, doi: 10.1116/1.2722758.

[122] H. Z. Wu, K. M. He, D. J. Qiu, and D. M. Huang, “Low-temperature epitaxy of ZnO films on Si (001) and silica by reactive e-beam evaporation,” *J. Cryst. Growth*, vol. 217, pp. 131–137, 2000.

[123] K.-H. Müller, “Ion-beam-induced epitaxial vapor-phase growth: A molecular-dynamics study,” *Phys. Rev. B*, vol. 35, no. 15, pp. 7906–7913, May 1987, doi: 10.1103/PhysRevB.35.7906.

[124] S. Tripathi *et al.*, “Thickness-dependent optical and structural properties of polytetrafluoroethylene/zinc oxide films by radio frequency magnetron sputtering,” *Adv. Polym. Technol.*, vol. 37, no. 8, pp. 2774–2787, 2018, doi: 10.1002/adv.21950.

[125] Y. Jiang, S. Pillai, and M. A. Green, “Realistic Silver Optical Constants for Plasmonics,” *Sci. Rep.*, vol. 6, p. 30605, Jul. 2016, doi: 10.1038/srep30605.

[126] J. Hwang, H. Lee, and Y. Woo, “Enhancing the optical properties of silver nanowire transparent conducting electrodes by the modification of nanowire cross-section using ultra-violet illumination,” *J. Appl. Phys.*, vol. 120, no. 17, p. 174903, Nov. 2016, doi: 10.1063/1.4967166.

[127] P. M. Natishan and W. E. O’Grady, “Chloride Ion Interactions with Oxide-Covered Aluminum Leading to Pitting Corrosion: A Review,” *J. Electrochem. Soc.*, vol. 161, no. 9, p. C421, Jun. 2014, doi: 10.1149/2.1011409jes.

[128] D. A. Glocker and S. I. Shah, *Handbook of Thin Film Process Technology*. Institute of Physics Pub., 1995.

[129] J.-M. Zhang, Y. Zhang, and K.-W. Xu, “Dependence of stresses and strain energies on grain orientations in FCC metal films,” *J. Cryst. Growth*, vol. 285, no. 3, pp. 427–435, Dec. 2005, doi: 10.1016/j.jcrysgro.2005.08.037.

[130] R. A. Maniyara, V. K. Mkhitaryan, T. L. Chen, D. S. Ghosh, and V. Pruneri, “An antireflection transparent conductor with ultralow optical loss (<2 %) and electrical resistance (<6 Ω sq −1),” *Nat. Commun.*, vol. 7, no. 1, pp. 1–8, Dec. 2016, doi: 10.1038/ncomms13771.

[131] L. Xu, L. Shi, and X. Li, “Effect of TiO2 buffer layer on the structural and optical properties of ZnO thin films deposited by E-beam evaporation and sol–gel method,” *Appl. Surf. Sci.*, vol. 255, no. 5, Part 2, pp. 3230–3234, Dec. 2008, doi: 10.1016/j.apsusc.2008.09.026.

[132] A. C. Marques *et al.*, “Stability under humidity, UV-light and bending of AZO films deposited by ALD on Kapton,” *Sci. Rep.*, vol. 9, no. 1, Art. no. 1, Nov. 2019, doi: 10.1038/s41598-019-54451-0.

[133] M. F. Al-Kuhaili and S. M. A. Durrani, “Optical properties of chromium oxide thin films deposited by electron-beam evaporation,” *Opt. Mater.*, vol. 29, no. 6, pp. 709–713, Feb. 2007, doi: 10.1016/j.optmat.2005.11.020.

[134] M. Novaković, M. Popović, Z. Rakočević, and N. Bibić, “Structural, optical and electrical properties of reactively sputtered CrxNy films: Nitrogen influence on the phase formation,” *Process. Appl. Ceram.*, vol. 11, no. 1, pp. 45–51, 2017.

[135] T. Wierzchoń, I. Ulbin-Pokorska, and K. Sikorski, “Corrosion resistance of chromium nitride and oxynitride layers produced under glow discharge conditions,” *Surf. Coat. Technol.*, vol. 130, no. 2, pp. 274–279, Aug. 2000, doi: 10.1016/S0257-8972(00)00696-4.

[136] H. Monard and F. Sabary, “Optical properties of silver, gold and aluminum ultra-thin granular films evaporated on oxidized aluminum,” *Thin Solid Films*, vol. 310, no. 1, pp. 265–273, Nov. 1997, doi: 10.1016/S0040-6090(97)00331-3.

APPENDIX A: IN SITU ELLIPSOMETRY OF EARLY GROWTH

Although, in this work, *in situ* ellipsometry is used exclusively to evaluate the optical properties of deposited films and ascertain the approximative thickness at which these become continuous, it may be of interest to extend this to the initial stages of growth. However, with the equipment and models used in this work, one does not obtain a valid assessment at this stage, as shown in Figure A.1.

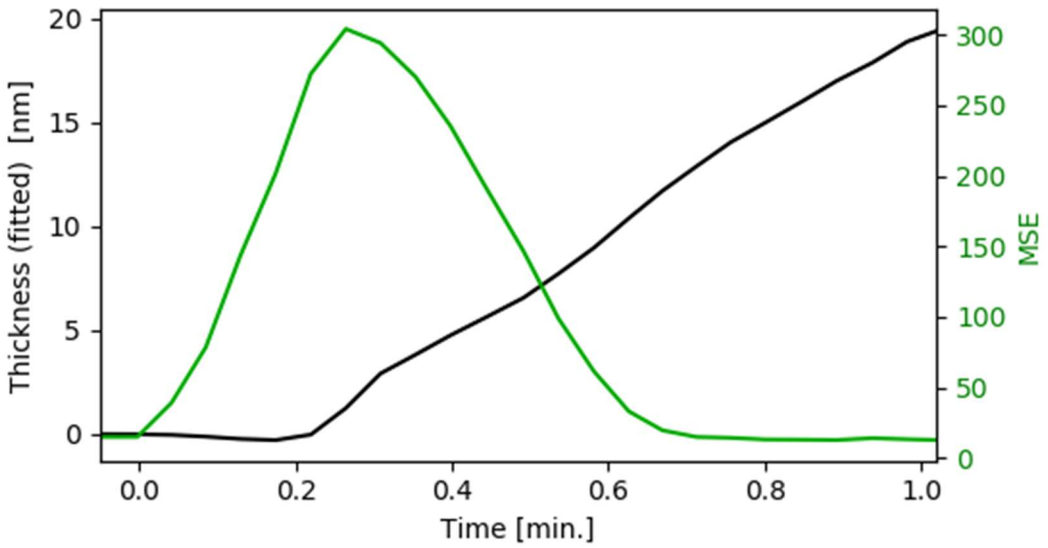

Figure A.1: Fitted Ag thickness and associated MSE as a function of deposition time for Ag layer deposited on B270 glass by magnetron sputtering and monitored by time-reversed fitting, as shown in Figure 4.11 (O_2 IPC).

Although the immediate increase in MSE indicates a change in optical properties, the negative thickness to which the model fits is not a physical solution. While a change in measured growth rate is possible during early stages (e.g. with the formation of stable clusters, an increase in surface coverage and a resulting change of the sticking coefficient of impinging adatoms on the sample), there has not been sufficient investigation oriented towards said early growth stages in this work to make a proper physical interpretation of the apparent shift in growth rate near 0.2 minutes.

Given the extremely high MSE at this point of the deposition, it seems more likely than not that the optical response of the highly discontinuous Ag layer is simply too far from that of a continuous layer for a reasonable fit to be made, and the error minimisation algorithm defaults to a non-

physical solution instead, the transition between these causing the observed shift. More in-depth analysis of the high-MSE thicknesses would be required to clarify this matter; fortunately, as the time-reversed fitting employed in this work takes the final continuous film thicknesses, which have been shown to be valid by *ex situ* measurements, as a starting point, this is not expected to have any significant effect on the results presented in this work.